University of Venda
Creating Future Leaders

University of Venda

Synthesis of Copper- and Iron-Doped Lithium Vanadium Oxides for Use as Negative Electrode Materials in Lithium-Ion Batteries

by

Isaac Mulaudzi

11634901

Submitted in fulfilment of the requirements for the degree

Master of Science in Chemistry

School of Mathematical and Natural Sciences

University of Venda

Thohoyandou, Limpopo

South Africa

Student:	Mr I. Mulaudzi	
Supervisor:	Prof. T. van Ree …	 .
Co-Supervisor:	Dr G.F. Ndlovu	
Co-Supervisor:	Dr M.A. Legodi	

© University of Venda

Declaration

I, Isaac Mulaudzi, hereby declare that this dissertation for the MSc (Chemistry) degree at the University of Venda has not been submitted for any other degree at any other university or tertiary institution. The dissertation does not contain any other persons' writing unless specifically acknowledged and referenced accordingly.

Signed (Student):  Date: April 2021

© University of Venda

Abstract

Li_3VO_4 has been considered a promising negative electrode material because of its high theoretical capacity (394 mAh g^{-1}) and zero strain during the charge and discharge processes. However, the electronic conductivity of Li_3VO_4 is low, which has led to an electrochemical performance unfavorable for practical application. In this study, copper- and iron-doped Li_3VO_4 are prepared by a simple and inexpensive sol-gel method. The doped Li_3VO_4 delivers high initial discharge and charge capacities of up to 70 mAh g^{-1} after 30 cycles for 5% Fe-doped material at a rate of 0.5 C. Conductive Cu and Fe are found to enable better Li^+ ion storage due to the improved electronic conductivity, Li ion diffusion, and structure stability, improving cycling and rate performance. This work provides some hints for preparing Li_3VO_4 based negative electrodes with high electrochemical performance.

Keywords: *Electrochemistry, Electrode, Lithium-ion battery, Lithium vanadium oxide, Doping.*

© University of Venda

ACRONYMS AND ABBREVIATIONS

CV	**Cyclic voltammetry**
DMC	**Dimethyl carbonate**
EC	**Ethylene carbonate**
EDS	**Energy dispersive X-Ray spectrometry**
EIS	**Electrochemical impedance spectroscopy**
FTIR	**Fourier transform infrared spectroscopy**
HOMO	**Highest occupied molecular orbital**
IR	**Infrared spectroscopy**
LIB	**Lithium-ion battery**
LUMO	**Lowest unoccupied molecular orbital**
LVO	**Li_3VO_4**
NMR	**Nuclear magnetic resonance spectroscopy**
PC	**Propylene carbonate**
PES	**Photoelectron spectroscopy**
SEI	**Solid-Electrolyte Interface**
SEM	**Scanning electron microscopy**
TGA	**Thermogravimetric analysis**
TEM	**Transmission electron microscopy**
XRD	**X-ray diffraction**

© University of Venda

List of Figures

© University of Venda

List of Tables

© University of Venda

Acknowledgements

Firstly, I would like to thank God for making it possible for me to write this dissertation and express my sincere appreciation to my supervisor Prof Teuns Van Ree from the Department of Chemistry who introduced me to this beautiful world of research and helping me through all stages of this study.

Secondly, I would like to express my deep sense of gratitude to Mrs Milangoni M.R., Mrs Bongwe A, Mr Mulaudzi T, Mr Mulaudzi K, Mr P.D. Negogogo and Mrs H.J. Negogogo for support, care and encouragement.

Dr Gebhu F. Ndlovu and Mintek are thanked for the opportunity to work at Mintek and for the XRD and SEM analyses.

Prof Neil Coville and Wits University are thanked for doing the TGA analyses.

Dr Yi Zhang and Nanjing Technological University are thanked for doing the electrochemical measurements.

Lastly, I would like to thank SASOL Foundation for funding.

© University of Venda

Table of Contents

© University of Venda

© University of Venda

Chapter 1: Introduction

A battery is a device that is used to store or generate electrical energy. It is made of different parts and materials, comprising metal, ceramics, polymers and inorganic electrode materials (Rui *et al*., 2011; Eriksson, 2001). A battery consists of a multiple number of electrochemical cells joined together. The role of a battery is to convert chemical energy to electrical energy by means of self-sustaining spontaneous electrode reactions. These reactions produce an electrical current only when connected to a closed circuit. Since the 1990s, rechargeable batteries have become widely used in electric devices, electrical vehicles and other electronic appliances (Gómez *et al*., 2010).

A battery consists of three main parts, as follows (Tarascon and Armand, 2011; Wu, 2015):

- **Positive electrode:** this is a negatively charged electrode that attracts positive charges from the electrolyte; it is the source of electrons to the external circuit. During the discharge process it can also be called *cathode* due to the occurrence of a reduction reaction.
- **Negative electrode:** it is the positively charged electrode that attracts negative charges from the electrolyte. During the discharge process this is also called the *anode* due to the occurrence of the oxidation reaction.
- **Electrolyte:** this is the medium that permits the transport of ions inside the battery between the positive and negative electrodes; it can be in the form of liquid, solid, or gel. It also works as physical barrier to prevent short circuiting between the electrodes.

1.1 Battery categories

Primary batteries are batteries that are non-rechargeable; their electrochemical reactions are totally irreversible, consisting only of chemical energy being transformed into electrical energy for transmission in the external circuit (Chen *et al*., 2009). The first appearance of primary battery was around 1800, being invented by Alessandro Volta (Eriksson, 2001). Although some primary batteries can be recharged, their charging performance is very poor (Akinyele *et al*., 2017). The most common primary batteries are zinc-carbon batteries, zinc/alkaline/manganese dioxide batteries, and zinc/mercuric oxide batteries (Barak, 1980).

© University of Venda

Even if such a battery can be charged, it has poor cyclability and during the discharge process there is copious formation of solid-electrolyte interphase which is unstable; during the charge process this kind of battery is associated with volume expansion, which can result in explosion. Figure 1.1 shows a typical primary electrochemical reaction between Li_2S and Cu, resulting in formation of a stable product. The electrochemical system is irreversible (Winter and Brodd, 2004).

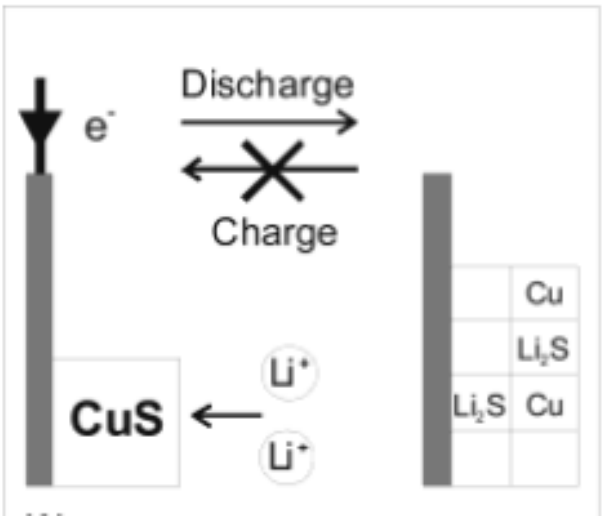

Figure 1.1: Schematic diagram illustrating discharge of a primary battery (Winter and Brodd, 2004).

Secondary batteries are batteries that can be charged and discharged continuously. Their chemical reactions are reversible - during discharge, they behave like primary batteries delivering current to the external circuit using the stored chemical energy; during the charge process the electrical energy from an external supply is converted to chemical energy stored in the battery. They typically cost more than primary (disposable) batteries, but have a lower total cost of ownership and environmental impact, as they can be recharged many times before they need to be replaced (Chan and Sutanto, 2000). There are many common types of rechargeable batteries, such as lead-acid, nickel-cadmium, nickel-metal-hydride and secondary lithium-ion batteries (Migov, 2017).

1.2 Importance of batteries in everyday life

Batteries are used for storage and delivery of energy. The most basic positive impact of batteries is that they make many things easier for humans. There are many activities that have made our life more comfortable for us through the development of batteries. Battery systems are applied in different sectors such as grid energy and industry (portable energy storage,

© University of Venda

renewable energy, grid energy and stationary energy), also in transportation (cars, buses, forklifts and e-bicycles), and lastly in consumer electronics and devices (which include smartphones, laptops, tablets, power tools and personal care equipment (Ding *et al*., 2019). One of the earliest examples is electronic watches; without batteries we would never have portable clocks that can be used to easily access time (Braga *et al*., 2017). Batteries have become more important in all aspects of everyday life, such as electric vehicles, portable devices and other applications (Walker, 2013).

1.3 Impact of batteries on the environment

After reaching their end-of-life, batteries are considered a major problem in the waste stream, contributing nearly indestructible ceramics, hazardous and toxic metals and metal oxides that may have a negative impact not only on the environment but also in humans (Aral and Vecchio-Sadus, 2008).

When batteries are burned they cause pollution by depositing harmful solids on the soil and releasing toxic vapours to the atmosphere (Malavika, 2004). When these harmful chemicals are released into the oceans they pollute our seas and as they are dumped into landfills, their toxic ingredients are left to seep into the soil, potentially causing massive and devastating damage to our natural ecosystems. Some studies have indicated that the reckless disposal of batteries in open landfills can cause many human and plant diseases (Pimentel *et al*., 2004). Some recently reported examples are diseases of the liver and kidneys, headaches, decreased IQ in children, and cancer as a result of exposure to such metals for an extended period (Kang, 2013).

Some of these issues can be addressed by recycling to avoid several of these diseases, or by using secondary batteries rather than primary batteries. Many organizations have been set up to promote the disposal and recycling of batteries to provide a safer environment (Schlesinger, 2010).

© University of Venda

Chapter 2: Literature Review

2.1 Lithium-ion batteries (LIBs)

As the development of portable and latterly, wearable, electronic appliances and electric vehicles continues, the provision of sustainable and clean energy has become a critical factor. The strategic importance of the search for novel energy storage materials has led to rapid development in the field (Dunn *et al*., 2011; Etacheri *et al*., 2011; Jeong *et al*., 2011).

Four main types of rechargeable battery have been developed (Figure 2.1): lead-acid, Ni-Cd, Ni-metal hydride, and lithium-ion batteries (LIBs, PLiON, and Li metal). Other battery types have been found to suffer memory effects, while LIBs have no memory effect, but high rate capability and low self-discharge. Lead-acid, Ni-Cd, and Ni-metal hydride batteries are being improved continuously, but they continue to suffer from shortcomings such as toxicity and energy and power density limitations.

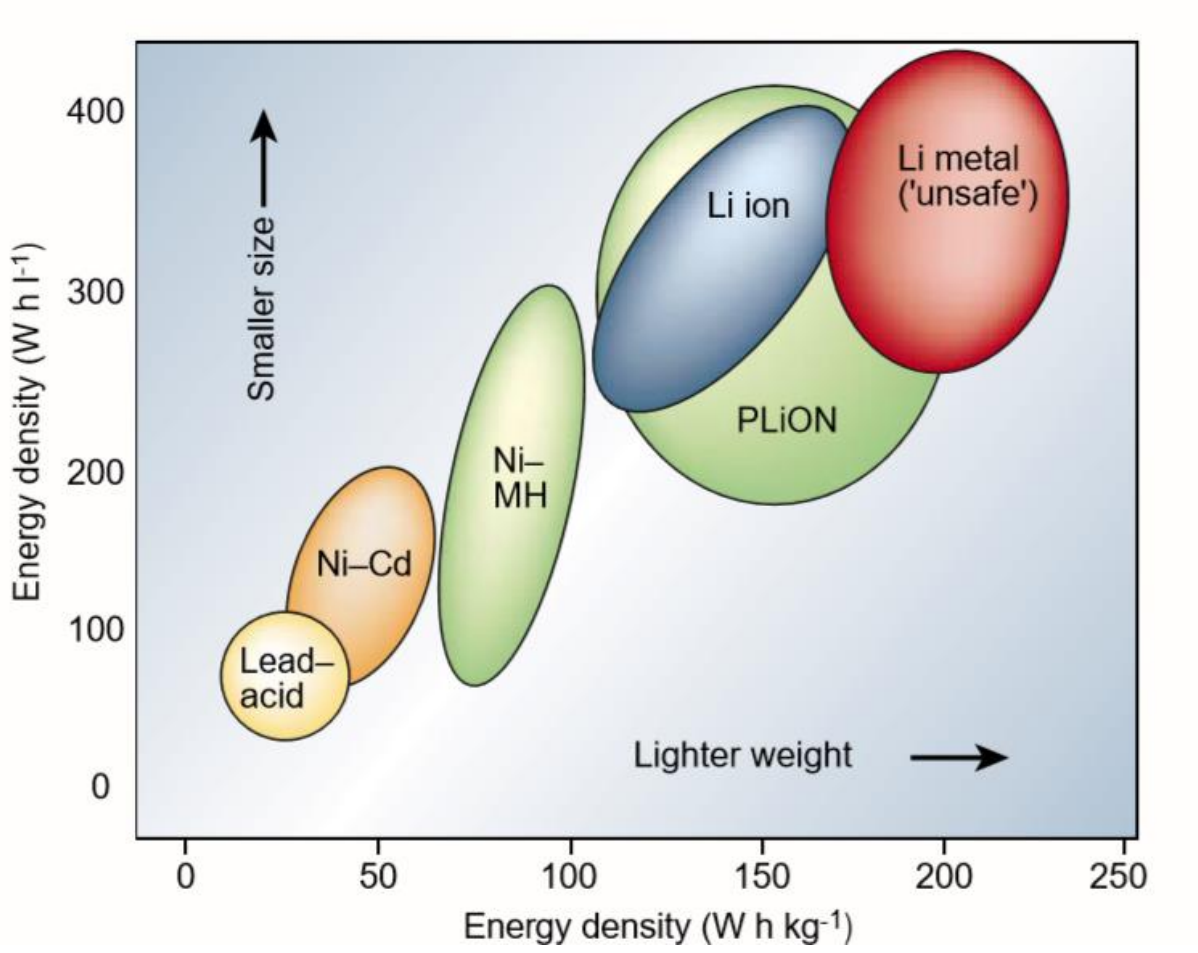

Figure 2.1: Comparison of volumetric and gravimetric energy densities of different rechargeable battery types (Aifantis *et al*., 2010).

© University of Venda

Lithium metal electrodes have been found to have a high energy density, both in gravimetric and volumetric terms; this is due to the fact that lithium has a low specific weight. There are only two barriers that hinder the development of lithium metal as a negative electrode material on LIBs: the formation and growth of Li dendrites, which have various morphologies, formed during cycling and the major cause for lower coulombic efficiency (Xu *et al*., 2014). When Li dendrites grow to a larger size, they may affect the separator, causing short circuiting, heating, and explosion since Li is thermodynamically unstable in organic solvent (Shen *et al*., 2018).

Extensive studies have been carried out for over the past 20 years in order to solve the problems associated with lithium metal as negative electrode material. For example, structural modification, metallic additives and organic additives, and metal or lithium plating have been found to be effective in suppressing dendrite formation. These methods may make it possible for lithium metal negative electrodes to be used in the next generation of LIBs (Brissot *et al*., 1999; Rosso *et al.*, 2006; Zhang *et al*., 2017).

Another type of secondary electrochemical storage device is the sodium-ion battery, which has received much attention due to the wide availability of sodium resources in nature. LIBs and Na-ion batteries share the same properties. To meet the growing demand for energy storage due to the increasing number of consumers, many batteries with high energy and power densities will be needed in the future. (Tang *et al*., 2015; Meng *et al*., 2017).

Though the commercial lithium-ion battery (LIB) was introduced by Sony Corporation in the early 1990's (Tarascon and Armand, 2011), it is still one of the most promising energy storage products of the future. Figure 2.2 shows the growing demand for LIBs for small applications (consumers) to larger applications where they have been introduced into electric-powered vehicles (Fogelman, 2019).

The first secondary lithium-ion battery appeared in the 1970s (Li *et al*., 2014). In 1991 the capacity of LIBs had increased sufficiently for Sony Corporation to introduce them to the consumer market (Rajagopalan, 2017), and they were also introduced gradually in automotive and material handling applications (Nishi, 2001; Li *et al*., 2011). Lithium-ion batteries have become popular due to their high performance, long cycle life, low self-discharge, low environmental pollution and relative safety (Deng *et al*., 2010). Over the next five years the global LIBs market is expected to increase by 17% per year due to the growing market demand (Lebedeva *et al*., 2016).

© University of Venda

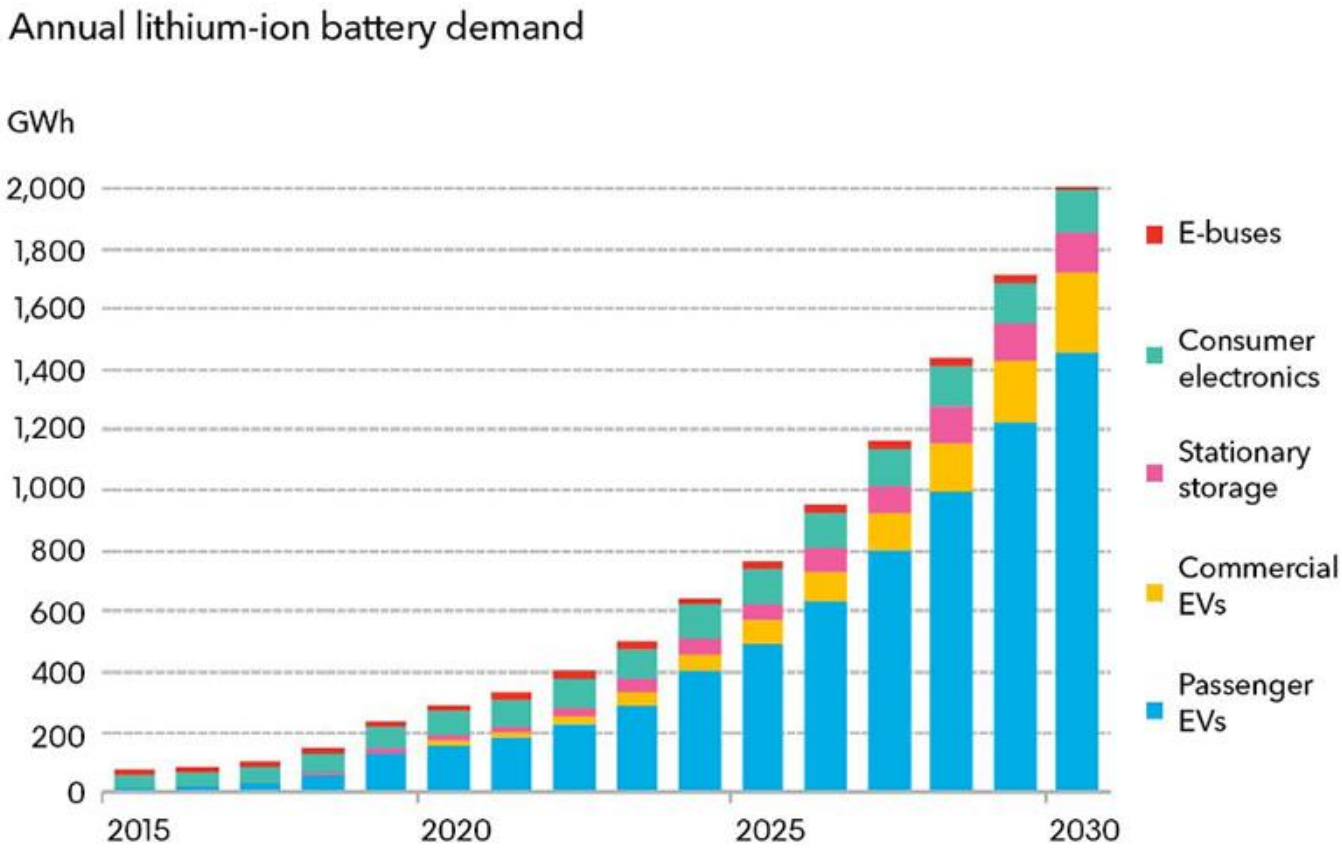

Figure 2.2: Actual and projected demand for lithium-ion batteries up to 2030 (Fogelman, 2019).

Lithium-ion batteries nowadays are the dominant technology for portable electronic applications (Hanna *et al*., 2015), and the demand is rapidly growing for electric vehicle (EV) applications (Tie and Tan, 2013), where increasing production is reducing costs.

Lithium-ion batteries typically consist of a number of lithium-ion cells that are connected using a battery management system to monitor the state of health and charge of each cell, especially in power electronics that supply high currents, to ensure the safety of the device (Cluzel and Douglas, 2012). The cell consists of a negative electrode (usually a graphite layer on a conducting metal), a cathode (a layer of an ionic mixed lithium metal oxide), an electrolyte that separates the electrodes (consisting of a lithium salt dissolved in an organic solvent), and external circuit. Other additives may be added to the electrolyte to improve performance and safety. Usually, the cell will also have a separator (typically a semi-porous membrane) to prevent electrical contact between the electrodes (Hao *et al*., 2013) and cause shut-down when overcharging and overheating. The development of new electrode materials, electrolytes, and separators is still continuing (Jeong *et al*., 2010).

© University of Venda

LIBs have been applied in many portable electronic devices since their original development, but LIBs with higher energy and power densities, as well as longer life expectancy, are needed urgently as alternative power sources. LIBs have become the first choice for portable electrochemical energy storage with improved cost/performance ratios that expand their application and enable new technologies that also depend on energy storage. Electrodes with higher rate capability, higher charge/discharge capacity, and providing high voltages can improve the energy and power density of LIBs (Nitta *et al*., 2015).

Different approaches have been followed regarding increasing charge capacity and Coulombic efficiency and reducing cost. The electrode material of LIBs has been found to be the critical component affecting the life span of LIBs, and various approaches have been studied to improve the electrodes' charge capacity and electrochemical performance (Leng *et al.*, 2015). Many have been used in applications such as portable electronic devices such as electric vehicle but there are still some factors, such as conductivity and cycle life that remain challenging (Mishra *et al*., 2018).

To find electrode materials with high charge capacity and good electrochemical performance, doping methods have been found to be effective and well-organized ways to change the essential electronic properties of battery materials. It is anticipated, for example, that the doping of allow metal ions in Li and V sites could be an efficient way to improve the electrochemical performance of Li_3VO_4 as electrode material (Chung *et al*., 2011).

The application and use of LIBs is nearly unlimited due to uses in the automotive industry and medical industry where miniature hand-held devices and implants are used. The development of LIBs in the portable electronics market is due to the gravimetric and volumetric energy densities that are higher compared to previous commercial rechargeable batteries (Tarascon and Armand, 2011; Winter and Brodd, 2004).

Figure 2.3 illustrates the charging process, with lithium ions deintercalation from the cathode and migrating to the negative electrode, and also the discharge process (producing power) where lithium ions intercalate into the positive electrode, with electrolyte allowing the movement of lithium ions between the electrodes (Tomaszewska *et al.*, 2019; Wu *et al.*, 2019). Each electrode is connected to a current collector (usually copper or aluminium) that allows a current to pass through the external circuit, thereby balancing the movement of lithium ions inside the battery (Bruce *et al.*, 2008; Meng and Arroyo-de Dompablo, 2009). The electrochemical reactions that take place inside a typical cell are given by:

© University of Venda

Positive electrode (Cathode): $LiCoO_2 \rightleftarrows Li_{1-x}CoO_2 + xLi^+ + xe^-$ (1)

Negative electrode (Anode): $C_n + xLi^+ + xe^- \rightleftarrows C_nLi_x$ (2)

Overall reaction: $LiCoO_2 + C_n \rightleftarrows Li_{1-x}CoO_2 + C_nLi_x$ (3)

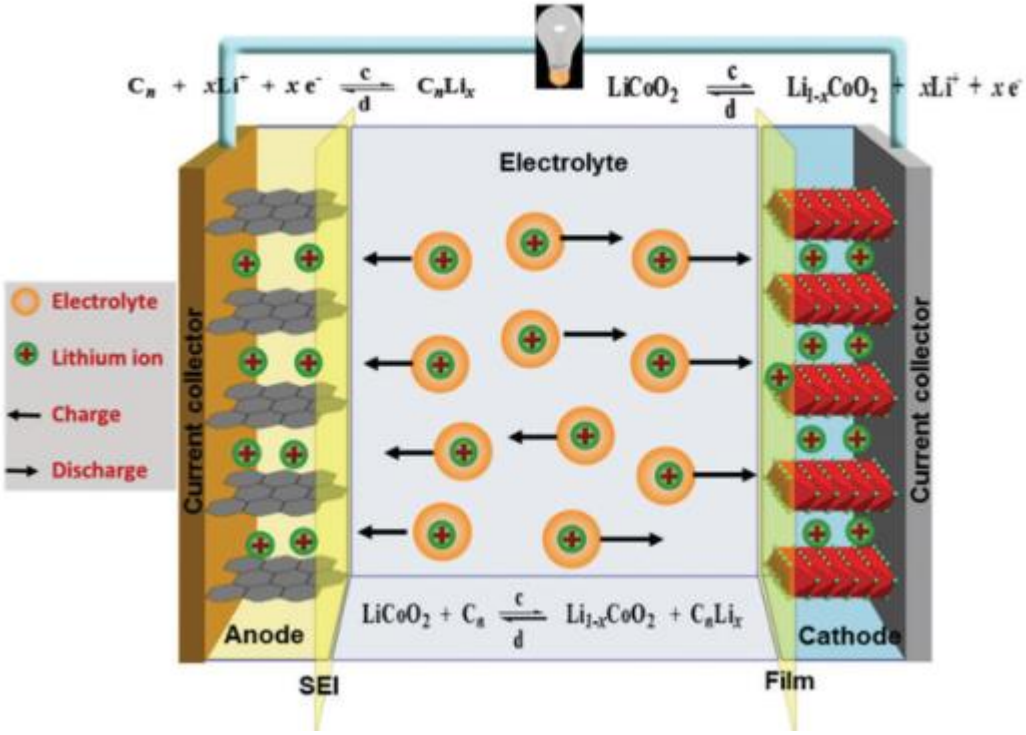

Figure 2.3: Schematic diagram showing the charge and discharge processes of lithium-ion batteries (Haregewoin *et al*., 2016).

The charge process is associated with the oxidation of Co^{3+} to Co^{4+} while the discharge process is associated with reduction of Co^{4+} to Co^{3+}.

Next generation LIBs are required to have five times higher energy density than current LIBs. This can be done by using an electrode material with a high potential by using higher voltage electrodes such as chalcogen or metal fluoride positive electrodes further more Li metal as an negative electrode material, or by choosing to use an electrolyte that allows the battery to work at a higher potential may help to achieve the above goal(Goriparti *et al*., 2014).

Different approaches have been followed to increase the performance of LIBs: (a) dimension decrease, so that faster ion and electron transport can occur; (b) morphology control to improve mechanical and structural stability; (c) coating and encapsulation to protect the electrodes from reacting with impurities or with the electrolyte; (d) doping and

© University of Venda

functionalization of the negative electrode to improve the transport of ions and electrons on the electrode, (e) provide structural support and (f) improve the chemical and thermal stability of the LIBs (Kamali-Heidari *et al*., 2018; Lee *et al*., 2014).

The current collector also plays an important role in the performance of a battery system. The current collector collects the current that is generated by the active material to the external circuit. It has been found that the resistance between the active material and current collector can be minimized and the effectiveness of the current collector can be increased by introducing an oxide or carbon. Different methods are used to introduce C or oxides into the current collector, including chemical vapour deposition (CVD), electrodeposition, electrochemical etching, chemical oxidizing, and also high temperature treatment (Zhu *et al*., 2020).

2.2 Toxicity of LIB Materials

Lithium-ion batteries nowadays are the most important energy storage technology for portable electronic applications (Hanna *et al*., 2015), and their application in electric vehicle (EV) is growing rapidly (Tie and Tan, 2013). However, governments worldwide are formulating regulations for LIBs since they can be harmful due to landfill seepage of lithium, cobalt, and other metals into groundwater and contamination of the environment (Lyster *et al*., 2017). The toxicity of LIB materials has not yet been fully characterized in the literature but they are considered to be safer compared to other materials, such as nickel-metal hydride and nickel-cadmium. In LIBs, the popular lithium cobalt oxide has been found to be toxic to the central nervous system by ingestion and may also damage the kidneys (Aral and Vecchio-Sadus, 2008).

2.3 The electrolyte

The electrolyte of LIBs must be selected carefully to offer strong resistance in the redox environment at anodic and cathodic sites. The electrolyte must be inert and stable over a range of temperatures. In most LIBs, the electrolyte is a lithium salt dissolved in an organic solvent, permitting the movement of ions between the electrodes during the charge and discharge processes (Xu, 2004).

There are some basic requirements for electrolytes. They should have a high lithium-ion conductivity, be able to work over a wide temperature range, should have a wide voltage

© University of Venda

window, should be environmentally friendly, have great chemical stability with stable phase structure while charging and discharging, have a relatively low cost, have good electrical stability, should be non-flammable and non-explosive, and should promote the reversible reactions between the electrodes (Wu, 2015; Yang *et al*., 2010).

Many studies have been carried out in trying to improve the performance of LIBs with regard to the electrolyte; electrolyte modification, including performance enhancing additives, have been introduced to form a stable electrode-electrolyte interphase that controls the solubility of active materials and formation of decomposition products and also improves the mechanical stability of electrodes (Zhao *et al*, 2017; Goriparti *et al*., 2014).

Electrolytes can be classified as liquid, solid state, and gel electrolytes. Liquid electrolytes can be divided further into different solvent types, such as organic carbonate, ester, ether, ionic liquid, and water. Solid-state electrolytes can be classified into two types: solid polymer and glass–ceramic composites.

2.3.1 Non-aqueous electrolytes for lithium-ion batteries

Organic electrolytes generally have an upper stability window between 1.5 V and 4.25 V, resulting in energy densities of organic electrolyte cells between 150 and 300 $Wh.kg^{-1}$, depending on the material systems, since (Li *et al*., 2015):

$$\text{Energy Density } E = (\Delta V \text{x} C)/ (1 + m_c), \quad (4)$$

Where ΔV = the operating voltage of the cell,

C = the capacity of the negative electrode material, and

m_c = the matching mass of the positive electrode material.

The most commonly used electrolyte formulations for lithium-ion batteries are either $LiPF_6$ or $LiClO_4$ in carbonate ester solvents, particularly ethylene carbonate (EC) and propylene carbonate (PC) (Whittingham, 1978). Negative electrodes are corroding continuously in the presence of most organic electrolytes, instead of forming a stable solid electrolyte interphase (SEI). Typical reduction products such as lithium propyl carbonate are generated at negative electrode surfaces in reaction with PC. This species can in turn be oxidized at the positive electrode at top-of-charge, thereby limiting capacity utilization and causing Coulombic inefficiency. To ensure proper functioning, an SEI must be formed to insulate and at the same time allow ion transport.

© University of Venda

A widely-used organic electrolyte solvent, propylene carbonate (PC), is less suitable for lithium-ion batteries, due to the fact that upon first charging of the batteries PC tends to co-intercalate into graphite, accompanied by severe exfoliation of graphite layers leading to the destruction of the electrode structure. Several ways have been explored to overcome the inherent incompatibility of PC with the lithium-ion battery system (Haregewoin *et al*., 2016; Wang *et al*., 2009; Zhang *et al*., 2009).

The strongly reducing lithiated intercalation compounds normally used as negative electrodes therefore need (SEI's) that enable stable cycling in cells. When $LiClO_4$ in EC is used as electrolyte, the SEI formed on carbon consists of Li_2CO_3 and lithium alkyl carbonates (Liao *et al*., 2015). The SEI film formed on hard carbon is mostly inorganic salt and contains precipitated species such as LiF on the surface (when $LiPF_6$ is used as electrolyte salt). Although a variety of organic electrolyte formulas and new electrolyte systems have been reported, much research work still needs to be done (Vignarooban *et al*., 2016). If the electrolyte is flammable it can overheat when overcharging, and explode (Tabuchi *et al*., 2007). The flammability of organic electrolytes can be lowered by adding compounds like fluoroalkyl ethers, fluorinated esters, and fluorocarbonates. It has been found that the use of a functional electrolyte additive is one of the most effective and economic methods for improvement of LIBs (Zhang, 2006).

Developing compatible electrolytes and additives plays a pivotal role, but overall, the electrolyte plays a crucial role in electrochemical storage devices and greatly influences commercial progress of LIBs (Ming *et al.*, 2019). In this regard, extensive efforts are still required to design new formulas or develop new components to make safe, efficient, high-energy LIBs available on a large scale.

2.3.2 Aqueous electrolytes for lithium-ion batteries

A recent alternative approach is to use aqueous electrolytes (Dunn *et al*., 2011; Whitacre, 2012). An aqueous hybrid ion (AHI) battery has been designed using activated carbon as a negative electrode material and manganese dioxide (MnO_2) as positive electrode material (Whitacre, 2012). These materials are already used in common alkaline batteries and some LIBs. Beside their low cost, aqueous batteries are also attractive because of their high safety and environmental friendliness in large-scale applications.

© University of Venda

The corresponding lithium storage mechanism is similar to that of non-aqueous systems, although the operating voltage window is narrower than that of an organic electrolyte system (about 1.23 V, the reduction potential of water). To avoid side-reactions, the choice of electrode materials is dictated by the reduction energy (negative electrode), which should be higher than the LUMO (lowest unoccupied molecular orbital) energy of the solvent, and the oxidation energy (positive electrode), which should be lower than that of the HOMO (highest occupied molecular orbital) of the solvent (Figure 2.4).

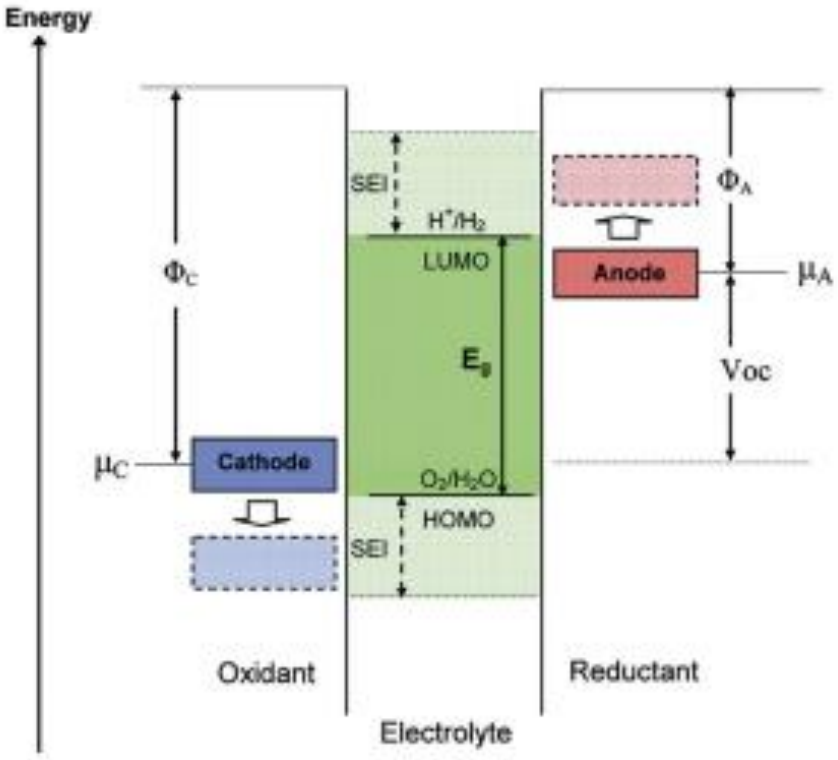

Figure 2.4: Stability window of the electrolyte (Goodenough and Kim, 2010). μ_A and μ_C are the working potentials, Φ_A and Φ_C are the work functions of the negative electrode and positive electrode, respectively, V_{OC} is the open circuit potential, and E_g is the difference in energy between HOMO and LUMO.

There is still much research to be done on solvents, electrolyte salts, and additives to understand the reaction mechanisms and obtain good cycling properties. Electrolytes determine to a large extent the safety and lifetime of LIBs. With the steadily increasing size and energy density of batteries, safety is more important than ever (Yamaguchi *et al.*, 2019). Electrolytes used in LIBs should preferably be non-flammable. Ionic liquids have been found to be promising candidates in this respect (Zhao *et al.*, 2017). Furthermore, ionic liquids could be medium- to short-term achievable replacements for organic solvents in secondary batteries due to their good combination properties with electrolytes, including wide

© University of Venda

temperature range, high conductivity, low flammability and volatility, and electrochemical stability.

2.4 Solid-electrolyte interphase (SEI) formation

The SEI, also called the negative electrode- or positive electrode-electrolyte interphase, plays an important role in a lithium-ion battery system, since it strongly influences the cycle life, self-discharge, low and high temperature behaviour, safety, power capability, morphology of lithium deposition, and irreversible capacity loss during the first charge cycle in LIBs (Peled *et al*., 1998). It has been found that in every functioning LIB (containing organic liquid electrolyte such as PE), the negative electrode material is covered by a SEI, produced by reduction processes between the electrode material and electrolyte.

The SEI is a thin layer about 30 to 50 nm thick (Lu *et al*., 2011), formed between the electrode material and the electrolyte during the LIBs first charge/discharge cycle. It is believed that the layer is of heterogeneous multi-layered structure having an inorganic inner layer usually containing LiF, Li_2O, and Li_2CO_3 near the electrode surface. Those layers allow the movement of Li^+ ions, and outer layer organic products that allow the movement of both Li^+ ions and electrolyte solvent, formed on the electrode surface during cycling. It has been found that the SEI has both advantageous and disadvantageous effects (Agubra and Fergus, 2014).

During its formation, it acts as a barrier that reduces the total mass of lithium ions. It reduces the surface area of the electrode and consumes lithium ions, which can cause poor performance of LIBs and thermal instability (Hamidah *et al*., 2019). During the formation of the SEI film, the mass of the electrode increases while the current and battery performance decrease. Some electrolyte is also consumed during each cycle in the formation of the SEI (Huang *et al*., 2014). The formed SEI layer is thicker at low potentials and thinner at higher potentials; it is also observed that the SEI undergoes some transformation at higher temperatures, allowing Li^+ ions to be in contact with electrolyte and electrons to pass through the SEI.

Since lithiated carbon and lithiated positive materials are unstable in air, LIBs are always assembled in discharged state; the electrolyte solution is also thermodynamically unstable at low and high potentials (Verma *et al*., 2010). During the first discharge of a LIB the electrolyte solution starts to reduce on the graphite negative electrode and forms a SEI in a

© University of Venda

two-step reaction that competes with the half-cell reaction at the electrode surface (Wang *et al*., 2018).

It is generally understood that SEI formation starts at about 0.8 V (Bryngelsson *et al*., 2007; Verma *et al*., 2010) and continues for a few cycles. With cyclic carbonate solvents such as ethylene carbonate or propylene carbonate, SEI film formation typically starts with a ring-opening reaction in the presence of the electrolyte. Thus, the SEI consists mainly of the decomposition products of electrolyte solvents and salts. The product of this decomposition develops a solid layer on the surface of the electrode material. While the SEI prevents solvent co-intercalation and exfoliation of the graphite (Besenhard *et al*., 1995), ion conduction in the SEI presumably is the result of the migration of solvated lithium ions through microchannels in the SEI.

Formation of SEI on the negative electrode is the result of the reduction process of the electrolyte and reaction with lithium salts (Goodenough and Kim, 2010). During the formation of the SEI layer there is irreversible consumption of lithium ions (Zhang *et al*., 2013). In the first step the graphite electrode is polarized to such an extent that the components can undergo reduction, and in the second step decomposition and precipitation occur to form the SEI layer until all sites on the graphite surface are covered by the SEI (An *et al*., 2016).

Figure 2.5 illustrates the formation of SEI on different types of recently used negative electrode materials. In graphite, there is expansion and contraction of volume during the intercalation process. In the Li storage material, the volume also increases and decreases with SEI formation during the cycling processes; and when metallic Li is used as a negative electrode material, during each cycle there is formation of new SEI.

SEI's are divided in two types, a stable SEI that is formed during the first few cycles and facilitates the performance of LIBs (Figure 2.6), where it depend on the potential window of the electrolyte; there is also unstable SEI formation during each cycle, which can result in poor performance of LIBs. This results in consumption of Li^+ ions, increasing the mass of the electrode and decreasing the specific surface area of the electrode (Hamidah *et al*., 2019).

The SEI should not allow transfer of electrons from the negative electrode, should be thick enough to suppress electron tunnelling, it should accommodate the change of volume during the cycling process, it should not crack during the cycling process, should allow transfer of lithium ions, and should be insoluble in and impermeable to the electrolyte (Xu, 2004).

© University of Venda

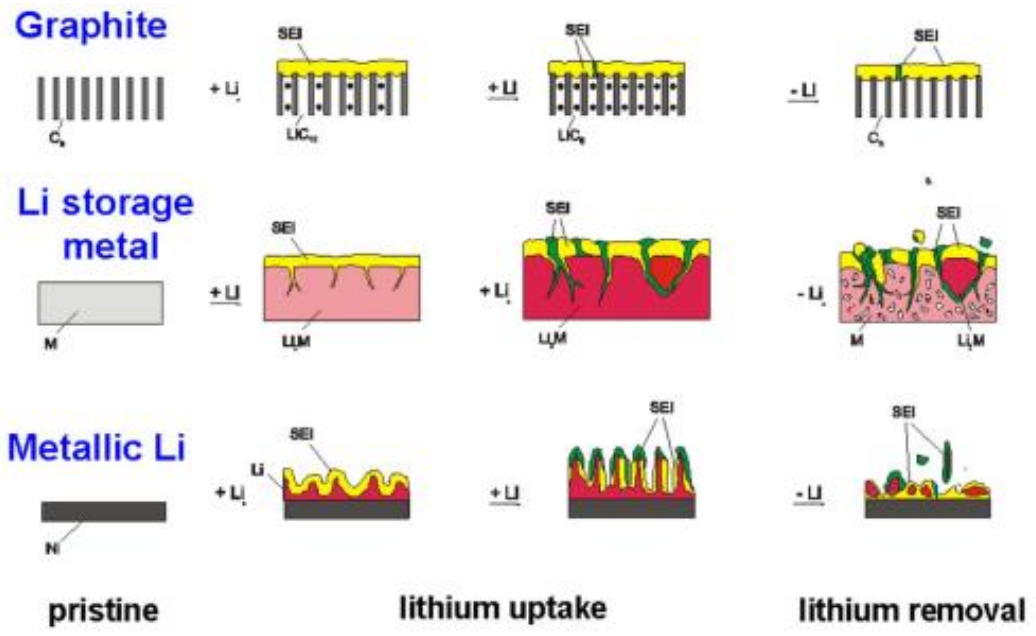

Figure 2.5: Stability of different negative electrode materials in the formation of SEI (Heine *et al*., 2015).

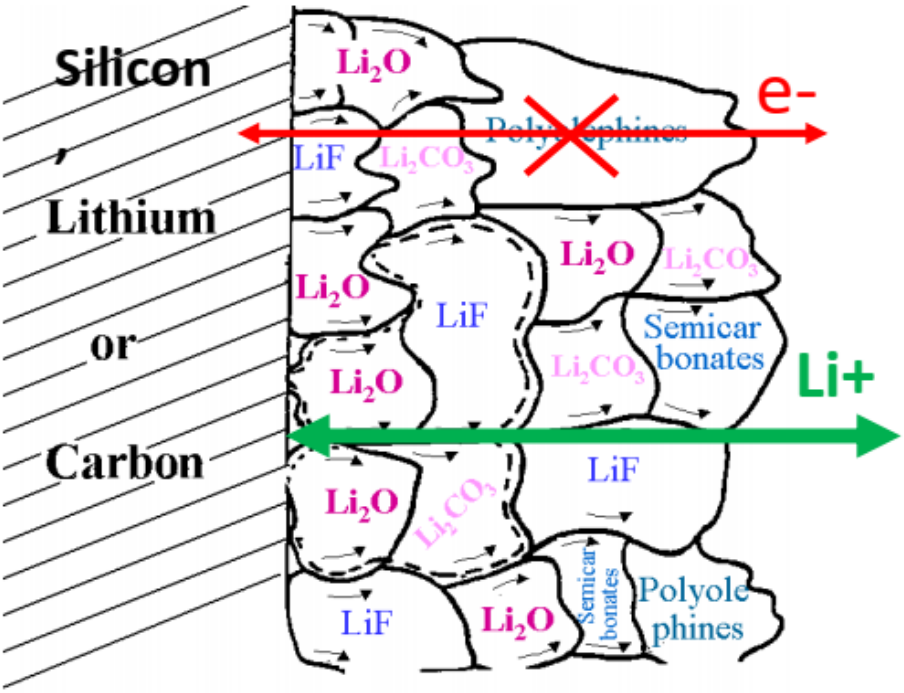

Figure 2.6: Schematic diagram of a stable SEI (Peled, 1979).

Different studies have investigated alternative ways to modify the formation of the SEI layer at a negative electrode; most of the electrolyte additives investigated have been used to

© University of Venda

reduce the continuous formation of SEI in each cycle, like vinylene carbonate which has been found to facilitate the formation of stable SEI. Propylene carbonate forms an unstable SEI (Goodenough and Kim, 2010; Zhang *et al*., 2001), which is uncontrollable at elevated temperatures.

An alternative approach is to introduce an artificial SEI on Li metal electrodes, which uses gases like N_2, O_2, F_2, CO_2 or SO_2 to form a thin passivation layer that is controllable. Among them N_2 has been found to form an elastic layer, while others like O_2, F_2, and CO_2 form a layer, and SO_2 forms an insulating and ultra-thin passivation layer (Koch *et al.*, 2015).

2.5 Electrode materials

The electrode materials are crucial elements determining the life and performance of LIBs. As various technologies developed, much effort has gone into improving electrode materials for LIBs (Goriparti *et al*., 2014; Meng *et al*., 2018). Apart from the movement of Li^+ ions through electrolyte, electrode materials play an important role in reversibility, cyclability, and rate performance (Ram *et al*., 2017). Many studies have also been done with regard to the regeneration of electrode materials of LIBs (He *et al*., 2015).

Li^+ ions are stored by different mechanisms in electrode materials (Figure 2.7), categorized according to the charging and discharging mechanisms and their reaction with Li^+ ions (Liu *et al*., 2012).

Intercalation/deintercalation materials follow the process of inserting and extracting Li ions into/from electrode material (Kamali-Heidari *et al.*, 2018). They include $Li_4Ti_5O_{12}$, Li_3VO_4 and graphite, with the storage mechanism being represented by the half-reaction (Malini *et al.*, 2009):

$$MO_x + yLi^+ + ye^- \rightleftarrows Li_yMO_x \quad (5)$$

Most of these reactions follow first order kinetics and are associated with small volume changes during the cycling processes. These compounds can store one lithium ion per M atom, which results in a low theoretical capacity (Palacin, 2009).

© University of Venda

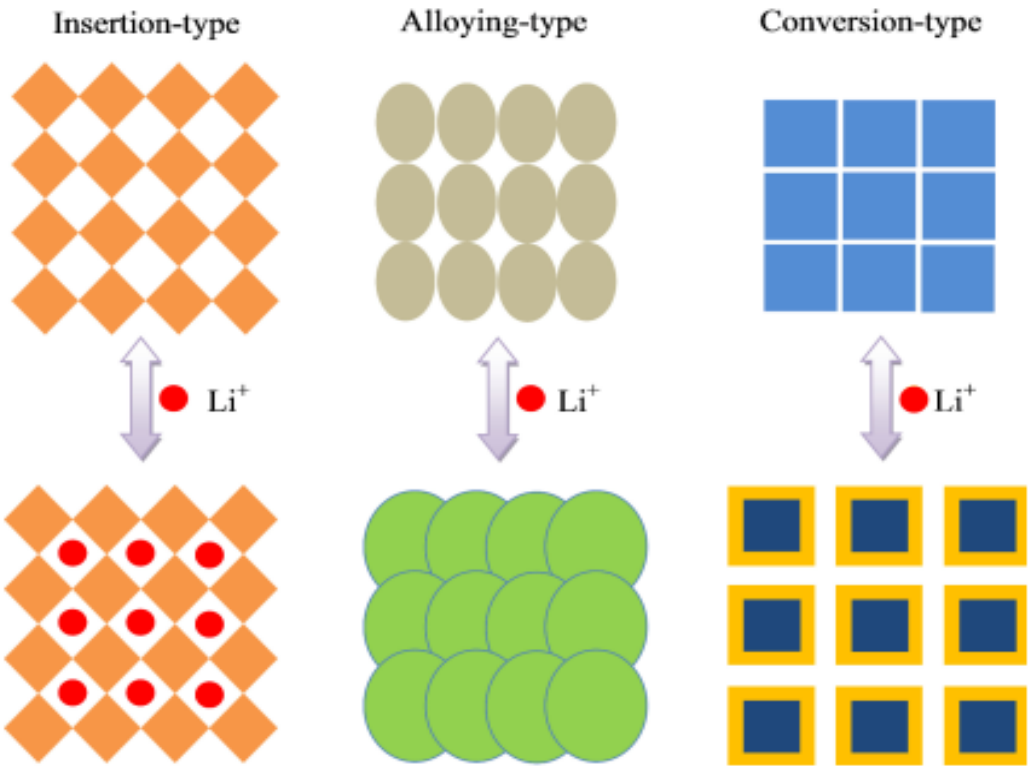

Figure 2.7: Different lithium ion storage mechanisms (Liu *et al.*, 2012).

Conversion reaction (i.e. reduction/oxidation) materials undergo solid-state redox reactions during the cycling process, and include mostly transition metal oxides, as represented by the half-reaction (Nitta *et al.*, 2015):

$$M_xO_y + 2yLi^+ + ye^- \rightleftarrows yLi_2O + xM \quad (6)$$

Figure 2.8 shows that, for instance, sulfur has a great specific gravimetric capacity but a low potential, while CuF_2 has a higher potential than all other conversion materials but not a great capacity.

Alloying/dealloying materials include metals like tin, lead, and aluminium, as represented by the half-reaction (Goriparti *et al.*, 2014; Liu and Xue, 2010):

$$M + yLi^+ + ye^- \rightleftarrows Li_yM \quad (7)$$

These materials are capable of storing multiple Li^+ ions per M, resulting in higher volumetric and gravimetric energy densities, although they may suffer from large volume expansion, which results in fast capacity fading (Liao *et al.*, 2017; Deng, 2015).

© University of Venda

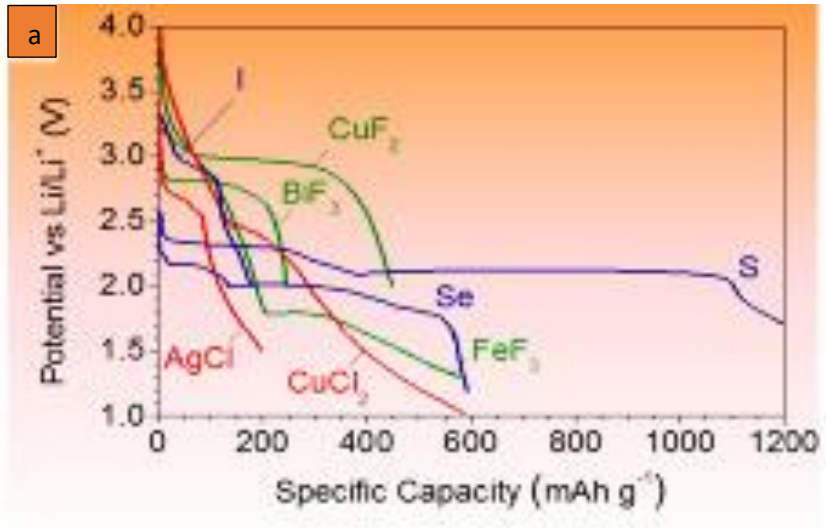

Figure 2.8: Potential/Specific Capacity curves of conversion positive electrode materials (Nitta *et al.*, 2015).

2.5.1 Requirements for positive electrodes (cathodes) of LIBs (Zhang *et al.*, 2010)

- In an intercalation compound such as $Li_3M_xV_{1-x}O_4$, the metal ions should have a high redox potential to achieve a high output voltage;
- To achieve a high charge/discharge capacity, a large number of lithium ions in an intercalation compound like $Li_3M_xV_{1-x}O_4$ should be reversibly intercalated and deintercalated;
- To ensure good cycling performance, intercalation/deintercalation of lithium ions should be reversible during the whole intercalation/deintercalation process, and there should be little or no change in the main host structure;
- Also the intercalation compound should be inexpensive, nontoxic, and environmentally benign.

Most positive electrode materials function by insertion and extraction of Li^+ ions into and from the host during the cycling processes. Chalcogenides have been used as positive electrode material for about three decades in LIBs due their properties of long cycle life, great gravimetric energy capacity, and high operating voltages. They were initially commercialized by Exxon. Chalcogenides include $LiTiS_2$, TiS_3, and $NbSe_3$, but they undergo structural changes during the cycling processes.

© University of Venda

The crystal structures of positive electrode materials used to host lithium ions are layered oxides ($LiCoO_2$, $LiMnO_2$), spinel oxides (LiM_2O_4, where M is Ni or Mn), and olivine polyanionic salts ($LiMPO_4$, where M = Fe, Co, Ni, or Mn), represented in Figure 2.9. The rate capability of positive electrode materials depends on their electronic and ionic conductivities and their capacity is determined by the position of the lithium ion in the structure (Tang *et al*., 2015).

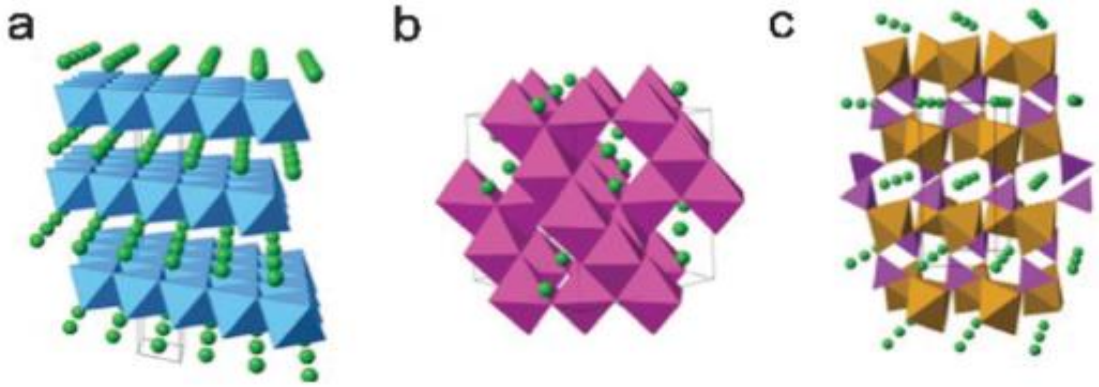

Figure 2.9: Crystal structures of different LIB positive electrode materials: (a) layered structure; (b) spinel structure; (c) olivine structure. (Julien *et al.*, 2014).

Spinel $LiMn_2O_4$ is a typical lithium intercalation compound that has received particular attention due to its improved performance in lithium-ion batteries (Wu *et al*., 2011). It has been studied as positive electrode material for many years since it exhibits a potential of 4.0/4.2 V versus Li^+/Li when cycled over the composition range of $Li_xMn_2O_4$ ($0 < x < 1$) and has higher thermal stability than the widely used $LiCoO_2$. It is also safer and more suitable for large capacity devices. But although spinel $LiMn_2O_4$ has many advantages, its low electrical conductivity is a limiting factor for applications requiring high power. Taking these two aspects into account, nano-structured $LiMn_2O_4$ materials have been synthesized with improved electrochemical performance such as high rate capability and long cycling life over their bulk counterparts, due to the large electrode/electrolyte interface and shorter Li^+ diffusion path length. In work by Tang *et al*. (2012), nanochain $LiMn_2O_4$ with 100 nm-sized beads was prepared using a starch-assisted sol–gel method. A special chain-like microstructure was obtained (Figure 2.10), while the particle size was reduced to the nano range.

© University of Venda

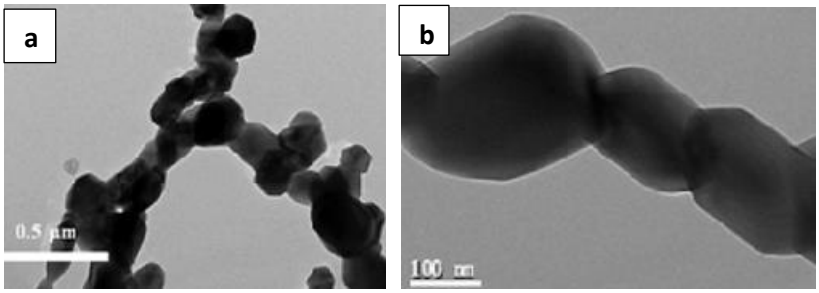

Figure 2.10: (a) and (b) TEM micrographs of nanochain LiMn2O4 (Tang et al., 2012).

Conversion electrode materials can be divided into two main types, comprising metal oxide (e.g. Fe_xO_y, Co_xO_y) and also metal phosphides (MY where M = Fe, Mn, Ni and Y = P, but also S and N). They have the common advantages of higher capacity, higher energy, low cost, and low operating potential; they are also environmentally compatible. They also have the similar disadvantages of unstable SEI formation, poor cycle life, high cost, and also low Coulombic efficiency (Goriparti *et al*., 2014).

Alloying/de-alloying materials (such as S, Se, Te, I, Li_2S) include MF and MCl (M = Fe, Cu, Ag, Bi, Ni, Co, Li) has been used as positive electrode material for LIBs for more than 2 decades. They generally show higher specific capacities, good safety, and high energy density, and shortcomings such as poor cycling, large volume expansion, and high irreversible capacity since they are usually associated with SEI formation (Park *et al*., 2010). The volume expansion also leads to higher mechanical stress on the material used, which results in degradation and cracking of material (Wu *et al*., 2020). Various approaches have been made with the aim of minimizing the volume expansion, including minimization of the active particle size and using nano-sized materials (Si for example) (Berg, 2015).

Vanadium pentoxide has some potential as positive electrode material because of the high energy density and good theoretical capacity of V_2O_5, which is 294 mAh g^{-1} at 2.0 - 4.0 V. However, its electron conductivity is quite low and lithium-ion conductivity is sluggish (Cheah *et al*., 2012). These properties, combined with poor structural stability, result in poor long-term cycling stability and rate performance (Chan *et al*., 2007). Vanadium pentoxide nanoparticles can be synthesized by a fast sol-gel method with citric acid at 600°C; they show good electrochemical performance, with a high initial discharge capacity of 276 mAh g^{-1} between 2.1 and 4.0 V, and have good cycling stability (Kim *et al*., 2015).

Vanadium pentoxide has been studied and used in different applications as a positive material (Coustier *et al*., 1999). It has been prepared using different methods and has been applied as

© University of Venda

positive electrode material in LIBs due to its high capacity and high intercalation rate. It has also been used as a lithium intercalation host due to its pore size and porosity, which lead to a high surface area (Mjejri *et al.*, 2013), which allows the electrolyte to penetrate (Coustier *et al*., 1999).

Other vanadium oxides have also been investigated for some time as electrode materials for LIBs since they have interesting characteristics such as high energy density, good rechargeability, rate capability, and low cost (West *et al*., 1992.). Vanadium has several oxidation states ranging from +2 to +5, forming a number of oxides such as VO_2, V_2O_5, V_3O_7, V_4O_9, and V_6O_{13}. The electrochemical capacity of a vanadium compound can increase due to the higher quantities of intercalated lithium ions possible per formula unit (Parasuraman *et al.*, 2013). This can be expected to result in a wide variety of redox reactions and wide potential window when used as electrode materials. Mixed oxides with lithium, such as $LiVO_2$, $LiVO_3$, and LiV_2O_4 are also known (Fu *et al*., 2015). However, mostly VO_2, V_2O_5, and Li_3VO_4 have been investigated as negative electrode materials.

Due to the structural differences of the vanadium oxides, V_2O_5 and LiV_3O_8 have been found to show some interesting positive electrode properties. Their electrochemical capacity strongly depends on the preparation method used and can reach 440 and 260 mAh g^{-1}, respectively, but they cannot be combined with known negative electrodes of lithium-ion cells as they do not contain extractable lithium (Qiao *et al*., 2012).

$LiFePO_4$ (LFP), with a phospho-olivine structure, has been studied widely as promising candidate positive electrode material for use in LIBs (Guan *et al*., 2017). LFP has become a competitive candidate due to its high operating voltage, high specific capacity, low cost, environmental friendliness and great thermal stability (Guan *et al*., 2017). LFP has a high electronic conductivity and high specific surface area, and it is also believed that various methods used to prepare and dope LFP can improve its electronic conductivity (Gong *et al*., 2016; Kulka *et al*., 2019). Some obstacles have been solved by reducing the crystallite size, but the limiting factor of LFP is that it has low electrical conductivity and lithium ion diffusion rate, which is believed to affect the cycling stability of LIBs (Vedala and Sushama, 2018).

The mixed oxides $LiMO_2$ (M = Co, Mn or Ni) have been studied extensively as positive electrode materials in LIBs (Muto *et al*., 2012). They have been applied in small and large applications for more than 20 years now because of their high volumetric energy density,

© University of Venda

high working potential, and low production cost (Du Pasquier *et al*., 2003). $LiCoO_2$ (LCO) has been found to share several characteristics with $LiNiO_2$ (LNO); the only difference being that LNO has a higher energy density and lower cost than LCO (Nitta *et al*., 2015). At higher temperatures, however, the $LiMO_2$ suffers from poor cycle performance, poor electric conductivity and low lithium ion conductivity (Mizushima *et al*., 1980). $LiMn_2O_2$ (LMO) has been studied and applied as a positive electrode material and also in supercapacitors due to its high charge and discharge rates. It shares some of the characteristics of LCO and LNO, but manganese is more widely available than Co and Ni (Tron *et al*., 2016).

The poor cycling performance of LMO is due to dissolution of the M ion ($Co^{3+/4+}$, Ni^{2+} and Mn^{2+}) in the electrolyte, and phase changes, which also lead to poor rate capability (Zhao *et al*., 2019; Yan *et al*., 2017; Deng *et al*., 2019). One way to improve the performance and electrochemistry is to reduce the distance between the electrodes (Nitta *et al*., 2015).

The mixed oxides $LiMO_2$ have higher potentials and specific capacity than $LiFePO_4$ (Figure 2.11); double and triple doping of LMO_2 results in increasing potential with specific capacity of the material (Nitta *et al*., 2015).

There are still many possibilities for development of novel, improved, electrode materials with high specific energy and capacity, which may be achieved by doping or/and coating.

2.5.2 Requirements for negative electrodes (Wu, 2015)

The negative electrodes investigated include graphitic carbon materials, amorphous carbon materials, nitrides, silicon-based materials, tin-based materials, new alloys, nano-oxides, and other materials.

- The redox potential should be low, to allow lithium-ion insertion into the negative electrode matrix;
- To have high reversible capacity, a high number of lithium ions should be able to intercalate and de-intercalate reversibly in the matrix;
- The matrix material should have a good surface structure so that a good solid-electrolyte interphase (SEI) film is formed with liquid electrolyte;
- The intercalation compound should have good chemical stability over its total volume and not react with electrolytes after the formation of the SEI.

© University of Venda

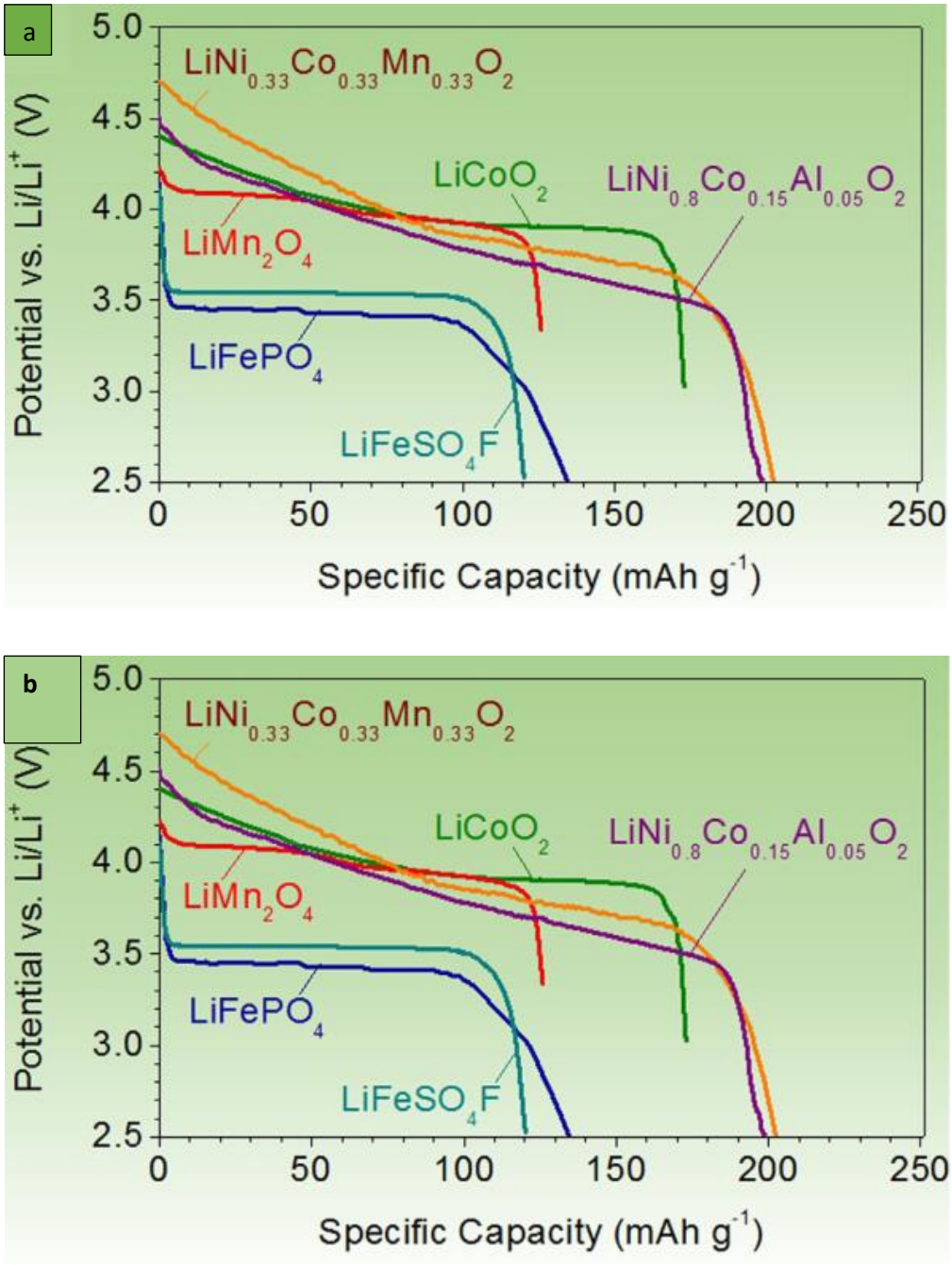

Figure 2.11: The Potential/Specific Capacity curves of several conversion positive electrodes (Nitta *et al*., 2015).

Much research has been conducted on alternative negative electrode materials (Li *et al*., 2011). Transition metal oxides achieve high gravimetric and volumetric capacities by conversion reactions (Poizot *et al*., 2000; Wu *et al*., 2012), with MoO_2 becoming a promising negative electrode material because of its metallic conductivity and high theoretical capacity (838 mAh g^{-1}) (Scanlon *et al*., 2010; Hu *et al*., 2015). However, because of its rapid capacity decay (Dahn and McKinnon, 1987; Ku *et al*., 2012) the performance of MoO_2 has to be improved by utilizing a range of nanostructured MoO_2 materials and/or dopants.

© University of Venda

The negative electrode is often found to suffer from poor cycle life (Xu *et al*., 2014). To develop a cell with a higher energy density and good electrochemical behaviour, it is necessary to find an negative electrode material with high specific capacity and good electronic conductivity. The specific capacity of an negative electrode material depends on the amount of lithium inserted, but increasing the amount of Li can have a negative effect on the stability of the crystal structure and also causes greater volume expansion and shrinking (Garche *et al.,* 2018).

For more than 20 years, carbon has been used as an negative electrode material and even now, it is still used because of its high electrochemical activity. Lithium intercalation between graphene planes offers good stability, electrical conductivity, and Li transport (Zheng *et al.,* 1995). Carbon is attractive because of its low cost, abundance, moderate energy density, power density and cycle life compared to other types of negative electrode material. However, its limitation is that the volumetric capacity of a graphene electrode is small. There are several types of carbon negative electrode; graphitic carbon consists of large graphite grains and provides fast Li ion transport, resulting in higher reversibility but lower volumetric capacity (Dahn *et al.,* 1995; Garche *et al.,* 2018).

$Li_4Ti_5O_{12}$ (LTO) is promising as a new negative electrode material for LIBs due to its high charge rate, high volumetric capacity and long cycle life; it is also inexpensive and safe (Bruce *et al.,* 2008) and develops zero strain during the charging and discharging processes. LTO also has excellent reversibility, fast Li^+ insertion/extraction ability and is highly lithiated. Unfortunately, its theoretical capacity is low and its operating voltage is higher than that of graphite/carbon (Guo *et al.,* 2012). Optimization of negative electrode material by controlling its particle size, nano-structuring and carbon coating has generally been found to improve electrochemical performance (He *et al.,* 2012), but LTO suffers from poor electronic conductivity and slow Li ion diffusion (Chen *et al.,* 2001; Dahn *et al.,* 1995).

Silicon is an alloying material with higher specific capacity and potential than those of graphite (Figure 2.12), but is problematic because electrical contact between the particles is lost due to volume expansion (Nitta *et al*., 2015). MnO also exhibits higher potentials than other negative electrode materials, but has lower specific capacity than silicon and also suffers from rapid capacity decay.

Turning to Li_3VO_4, this material shows promise as negative electrode material for LIBs. Although its theoretical capacity for 2-electron insertion/extraction is ~394 mAh g^{-1}, which is

© University of Venda

higher than that of graphite (~372 mAh g^{-1}) (Li *et al.*, 2014; Liang *et al.*, 2015), with only 4% volume expansion, its actual specific capacity is too low for practical application in LIBs. A composite of Li_3VO_4 with N-doped carbon was found to produce initial discharge and charge capacities of 686 and 540 mAh g^{-1}, respectively, with excellent cycle stability (Zhang *et al*., 2016).

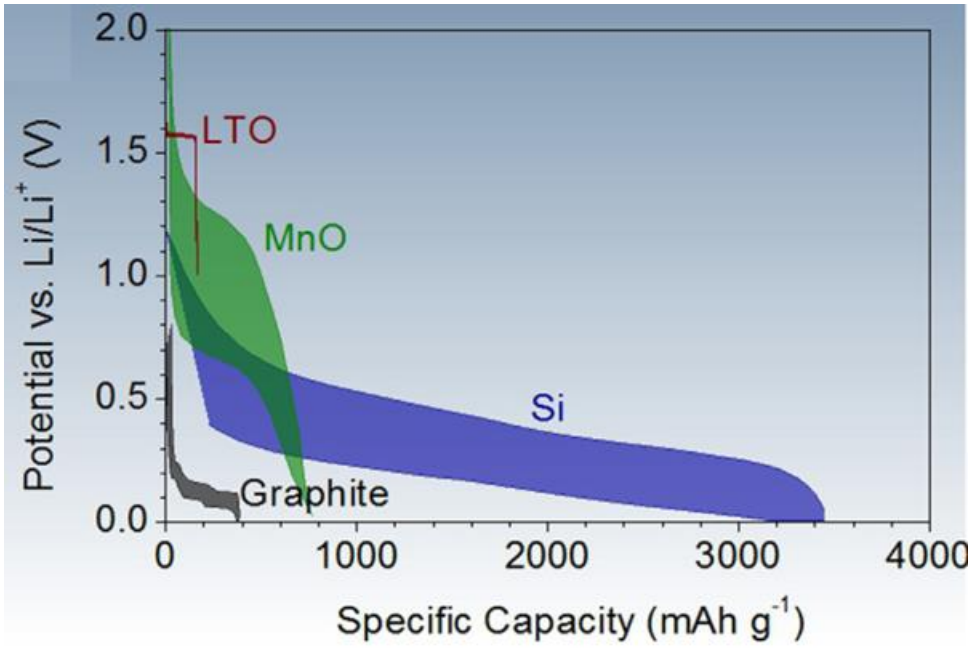

Figure 2.12: Potential/Capacity behaviour of several negative electrode materials (Nitta *et al*., 2015).

2.6 Safety concerns

Due to the increasing demand for energy storage devices, the safety of LIBs has become a major issue due to the increasing energy density (Yuan and Liu, 2019). The separator and electrolyte are the main factors determining battery safety. External battery management systems can also be introduced to maintain safety in LIBs (Garche and Jossen, 2000).

The separator (also called electrical insulator) is an insulator which is found between the negative electrode and positive electrode materials of the LIB in a three-dimensional structure It allows the movement of ions through the electrolyte between the electrodes (Deng, 2015), while blocking short-circuiting and conversion of stored chemical energy to heat (Goodenough and Park, 2013).

© University of Venda

The separator plays an important role in battery safety even though it is not an active material in the battery. Different strategies have been tried to improve separator properties. Commonly used separators in LIBs are polymeric, which promotes thermal stability; however, incomplete and non-uniform wetting of the separator can cause short-circuits, mainly due to the formation of lithium dendrites on the positive electrode (Wang *et al*., 2012).

Different types of separator are currently used, but the most commonly used separators are polyolefins such as polyethylene (PE) and polypropylene (PP), with a three-layered (PP/PE/PP) structure having the best thermal stability; if the temperature of the battery increases, the middle (PE) layer of the battery melts, which then shuts down the battery by sealing the pores in the separator and so stopping the movement of ions between the electrodes (Zhang *et al*., 2015).

As described above, the electrolyte plays a crucial role in the transport of lithium ions between the electrodes (Jow *et al*., 2010). The most widely used electrolytes are still based on flammable organic carbonates that can ignite at elevated temperatures (Verma *et al*., 2010). Different studies have resulted in improved safety of liquid electrolytes. Addition of flame retardants, especially phosphorus containing organic compounds, was found to reduce flammability of electrolytes. Ionic liquids have also been implemented as electrolyte solvents or additives, because they are non-volatile and nonflammable (Hung *et al*., 2003; Xiang *et al.*, 2013).

Redox shuttles have also been used to reversibly protect secondary batteries from overcharging. An ideal redox shuttle is oxidized and reduced reversibly at a potential above the end-of-charge potential of the positive electrode. This mechanism protects the battery against overcharging because the potential of the positive electrode cannot rise above the oxidation potential of the shuttle molecule (Li *et al*., 2011; Wang *et al.*, 2008).

© University of Venda

Chapter 3: Problem Statement, Aim and Objectives

Due to increasing CO_2 emissions and increasing use of energy over several decades, our environment has been affected by global warming, greenhouse gas emissions and climate change. Therefore, much research has been carried out to alleviate or reduce climate change by development of lithium-ion batteries. The search for better energy storage methods has produced secondary batteries with desirable properties such as high energy density, high coulombic efficiency, and relative safety. However, in large-scale applications there are still capacity and stability issues such as performance degradation and low-temperature performance. These issues are addressed in various ways, such as using safer electrolytes with better lithium-ion conductivities, adding SEI-enhancing and flame-retardant substances to the electrolyte, increasing electrode surface area and also decreasing the distance between the electrodes. Circuitry is now also used in each battery to monitor the state of charge in real time so as to optimize the use of the battery, but it remains necessary to continue looking for improved electrode materials.

Vanadium has oxidation states ranging from +2 to +5, forming a number of oxides with wide potential windows when used as electrode materials. Composite oxides with lithium, such as $LiVO_2$, $LiVO_3$, and LiV_2O_4 are also known (Fu *et al*., 2015). However, mostly VO_2, V_2O_5, and Li_3VO_4 have been investigated as negative electrode materials. Vanadium oxides have been found to have higher capacities and are easy to synthesize with different crystal structures. Nanostructured vanadium oxides can intercalate several equivalents of lithium ions.

In previous work (Mulaudzi, 2019), doped lithium vanadium oxides with varying compositions(Fe, Cu and Ag) and varying morphologies were synthesized. It is necessary to better control the elemental composition, size, and morphology of the mixed oxide particles obtained.

3.1 Aim

The main aim of this study is to develop better and safer lithium-ion power sources by the introduction of new electrode materials to overcome capacity and stability problems, providing a better way for commercial production of electronic appliances and electric vehicles.

© University of Venda

3.2 Objectives

The main objectives of this study are to find new electrode materials to improve the functional and safety behaviour of lithium ion power sources, so as to provide a way for commercial production of electric vehicles. More specifically, this study is pursued to achieve the following objectives:

- Synthesis of novel copper- and iron-doped lithium vanadate electrode materials;
- Physical and electrochemical characterization of the materials.

© University of Venda

Chapter 4: Experimental

4.1 General experimental conditions

All reagents and solvents were Reagent Grade, purchased from Sigma-Aldrich. A Büchi rotatory evaporator was used to evaporate the solutions, and a Scientific muffle oven was used for the temperature-programmed calcination of samples.

Fourier transform IR (FTIR) spectroscopy was performed on a Bruker Alpha at the University of Venda. Thermogravimetric analysis (TGA) was performed by Witwatersrand University's Chemistry Department on a Perkin-Elmer TGA4000.

Thermogravimetric analysis (TGA), Eight to 10 mg sample was heated in a nitrogen/air mixture with flow rates 20 ml/min each at pressures of 2.8 – 3.0 bar. The samples were heated from 35 to 900°C at a rate of 10°C/min.

Scanning electron microscopy was executed at Mintek on a Jeol JCM 6000Plus at an acceleration voltage of 15.0 kV, and powder XRD spectra were recorded at Mintek on a PANalytical X'Pert Pro diffractometer with CuKα radiation (λ = 1.5046 Å, 45 kV, 40 mA, step size = 0.02°).

XRD diffractograms were obtained in a scan range between 0 and 90°. The lattice parameters and crystal information were obtained by Rietveld refinement using Topaz software. An SEM/EDX combined instrument was used for energy dispersive X-ray spectroscopy (EDX) for the elemental analysis of the samples. XRD analysis of samples was also conducted on a Bruker AXS D8 X-ray advanced powder diffractometer. The XRD was fitted with a LinxEye detector, nickel filter and Cu Kα-radiation operated at 40 kV and 35 mA with wavelength alpha of 1.78897 Å. XRD patterns were recorded with a step size of 0.02˚/s in the 2θ range of 0 to 100° diffraction angle.

Transmission electron microscopy (TEM) and energy dispersion X-ray spectroscopy (EDX) were conducted on a JEOL JEM-2100F field emission electron microscope. The samples were suspended in ethanol by ultrasonication and subsequently drop-casted on a 300 mesh formvar coated nickel grid from SPI supplies.

Cyclic voltammetry (CV) and electrochemical impedance spectroscopy (EIS) measurements were carried out at Nanjing Tech University on a Bio-Logic VSP potentiostat. The frequency

© University of Venda

of the EIS measurements ranged from 100 kHz to 0.1 Hz. CV was executed at a scan rate of 0.2 mV/s with the voltage window between 0.01 V and 3 V (vs. Li^+/Li).

The cycling performance was determined at Nanjing Tech University on a battery tester (Wuhan LANHE Electronics Corporation). The cycling performance was tested at 200 mA/g (0.5C) with the voltage window between 0.01 V and 3 V (vs. Li^+/Li). The working electrodes were made using a slurry method with lithium vanadium oxide (LVO)-based powders, Carbon Super P and polyvinylidene fluoride with a mass ratio of 8:1:1; the mixture was added into *N*-methyl-2-pyrrolidone and stirred overnight. The slurry was cast onto copper foil and dried at 80°C for 12 h. The standard CR2032 type coin cell was assembled in an argon-filled glovebox using the LVO as working electrode and lithium metal foil as counter electrode. The electrolyte was 1 M $LiPF_6$ dissolved in ethylene carbonate (EC)/diethyl carbonate (DEC) (EC/DEC = 1:1 v/v) (Sigma Aldrich) and Celgard 2420 was used as the separator.

4.2 Synthesis of undoped and doped Li_3VO_4 samples by sol-gel method

4.2.1 Using cellulose as template

Synthesis of Li_3VO_4

Microcrystalline cellulose (2.31 g) was suspended in 51 ml *N*,*N*-dimethylacetamide in a dry two-necked, round-bottomed flask fitted with a magnetic stirrer, reflux condenser and $CaCl_2$ drying tube. The suspension was heated to 165ºC and stirred for 1 hour at that temperature. After cooling the suspension to 100ºC, 6.21 g (90 mmol) lithium nitrate was added while stirring, followed by 2.683 g (14.75 mmol) vanadium pentoxide, continuing stirring at 100ºC for 1.5 hours or until clear. The stirring bar was removed and the mixture was transferred to a single-necked flask. The solution was then evaporated, initially at 110ºC for 12 h to get a precursor in the form of foam, and then the dried foam was finely ground and transferred to a muffle oven for calcination.

Synthesis of $Li_3V_{1-x}M_xO_4$

Microcrystalline cellulose (2.31 g) was suspended in 51 ml *N*,*N*-dimethylacetamide in a dry two-necked, round-bottomed flask fitted with a magnetic stirrer, reflux condenser and $CaCl_2$ drying tube. The suspension was heated to 165ºC and stirred for 1 hour at that temperature.

© University of Venda

After cooling the suspension to 100ºC, 6.21 g (90 mmol) lithium nitrate was added while stirring until the solution was clear, followed by an appropriate amount of vanadium pentoxide (indicated in Table 4.1). Stirring continued at 100ºC for 1.5 hours or until clear, then the solution was cooled and the appropriate amount of M (Cu or Fe) salt added. After heating another 1.5 hours at 100ºC, the stirring bar was removed and the mixture was transferred to a single-necked flask. The solution was then evaporated, initially at 110ºC for 12 h to get a precursor in the form of foam, and then the dried foam was finely ground and transferred to a muffle oven for calcination.

The doped materials were made by adding appropriate amounts (x = 0.01, 0.05, 0.1, 0.3, 0.5 equivalents.) of salts (cupric carbonate or ferric nitrate) to the final reaction mixture, as indicated in Table 4.1.

Table 4.1: Vanadium and dopant M amounts (g) used for different values of x. M = Fe or Cu.

x	**0.01**	**0.02**	**0.05**	**0.1**	**0.2**	**0.3**	**0.4**	**0.5**
V	29.205	28.910	28.025	26.550	23.600	20.650	17.700	14.75
M	0.295	0.590	1.475	2.950	5.900	8.850	11.800	14.750

4.2.2 Using starch as template

The same procedure was repeated by replacing cellulose with starch, using deionized water as solvent.

© University of Venda

Chapter 5: Results and Discussion

Samples were prepared as described under Experimental, and coded as shown in Table 5.1.

Table 5.1: Samples and sample codes.

Samples	Sample code (Starch)	Sample code (Cellulose)
Li_3VO_4	A	B
$Li_3Cu_{0.01}V_{0.99}O_4$	Cu0.01A	Cu0.01B
$Li_3Cu_{0.05}V_{0.95}O_4$	Cu0.05A	Cu0.05B
$Li_3Cu_{0.1}V_{0.9}O_4$	Cu0.1A	Cu0.1B
$Li_3Fe_{0.01}V_{0.99}O_4$	Fe0.01A	Fe0.01B
$Li_3Fe_{0.05}V_{0.95}O_4$	Fe0.05A	Fe0.05B
$Li_3Fe_{0.1}V_{0.9}O_4$	Fe0.5A	Fe0.1B
$Li_3Fe_xV_{1-x}O_4$	CuA	CuB
$Li_3Cu_xV_{1-x}O_4$	FeA	FeB

5.1 LVO and doped LVO prepared Using Starch as Template

5.1.1 TGA and DTG results

Figure 5.1 shows the thermogravimetric analysis (TGA) of LVO Sample A in an air/N_2 flow. The initial weight loss of 26.74% which occurred from about 48°C to 107°C for most samples is associated with the loss of adsorbed water (Chen *et al*., 1996). The loss of intercalated water starts at about 107°C, followed by oxidation, combustion, and decomposition of starch and nitrate, leading to a constant mass above 600°C. This amounts to a total mass loss for the whole process of 65% (Dai *et al*., 1999). The differential thermogravimetry (DTG) curve shows three peaks, attributed to the loss of water, decomposition of starch, and loss of NO_2. Above about 700°C there is no more change, meaning there is no further phase transformation (Du *et al*., 2015; Kriston *et al*., 2019). Each

© University of Venda

step on the TGA curve has a corresponding endothermic peak on the DTG curve (Shchelkanova *et al.*, 2019).

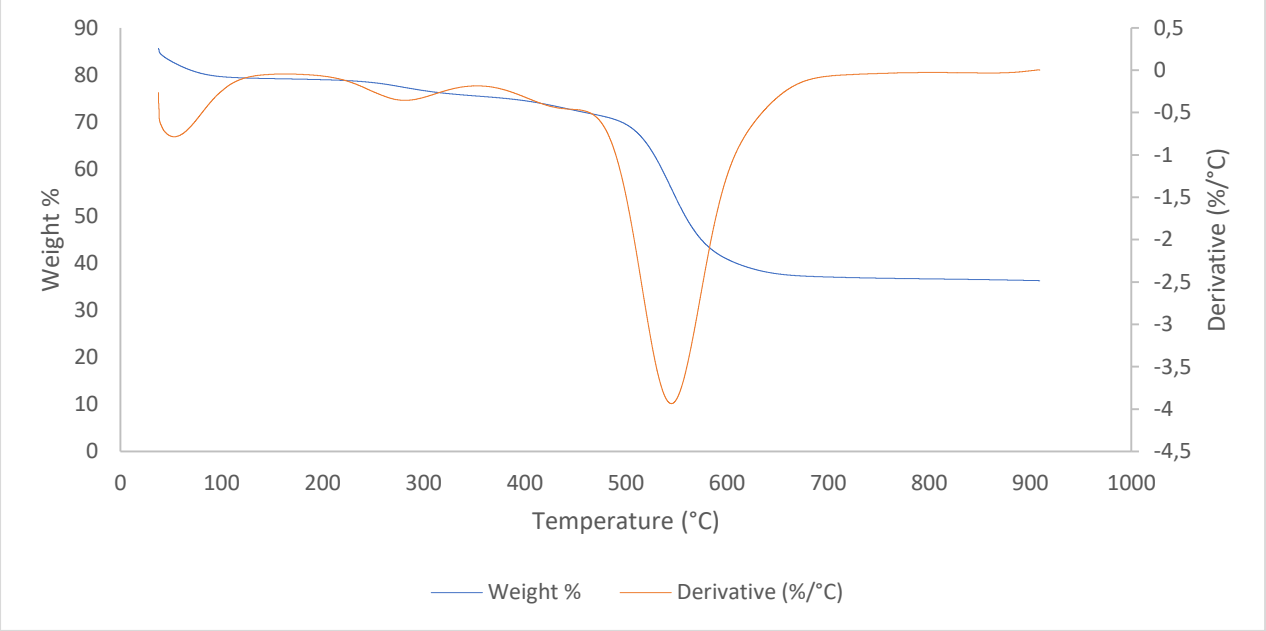

Figure 5.1: Sample A TGA and DTG analyses.

The DTG of Cu0.05A (Figure 5.2) shows four main peaks. The first two peaks at 85.5°C and 449.54°C are attributed to the loss of physically and chemically bound water, while the large endothermic peak at 600°C is assigned to the decomposition of starch and nitrate with release of water, CO_2, and NO_2. The exothermic peak at around 800°C is assigned to the combustion of graphene.

© University of Venda

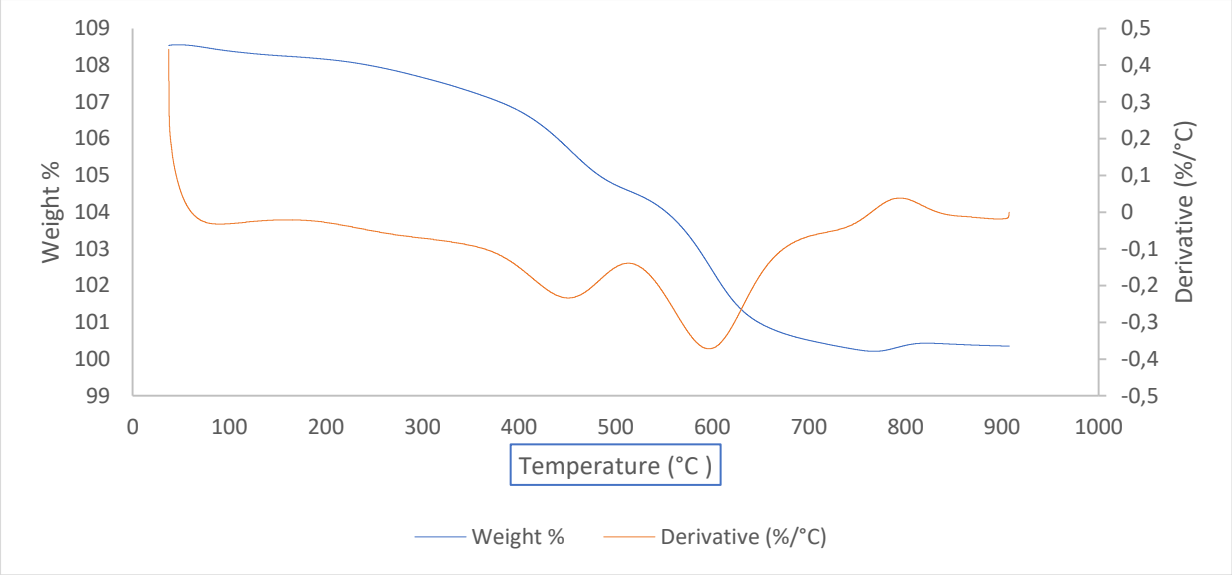

Figure 5.2: TGA and DTG analysis of 5% Cu-doped LVO.

TGA and DTG of Sample Fe0.05A (Figure 5.3) again shows gradual weight loss due to the release of adsorbed and chemically bound water molecules. The first 3 endothermic peaks (65.95°C, 156.62°C and 363.26°C) are assigned to the physically and chemically bound water. The peaks at 534.56°C and 604.36°C are attributed to pyrolysis of starch and $LiNO_3$.

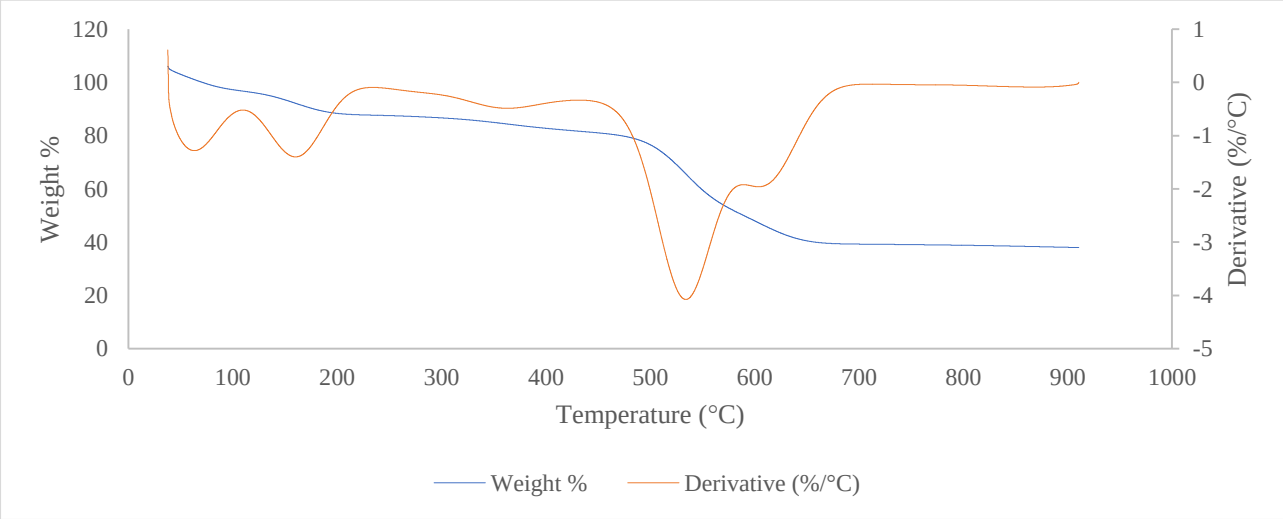

Figure 5.3: TGA and DTG analysis for 5% Fe-doped LVO.

5.1.2 Infrared Spectroscopy

The FTIR absorption bands of the various stretching and bending vibrations were recorded. In undoped LVO (Figure 5.4), the absorption band for Li-O is around 450 cm^{-1}. The band between 500 and 800 cm^{-1} is associated with the stretching vibrations of V=O bonds of the

© University of Venda

VO_4 tetrahedra. The weak absorption at around 3500 cm^{-1} is assigned to -OH due to water adsorption by the sample. As the concentration of the dopant increases the V=O absorption band shifts to higher frequencies. All spectra clearly show the V-O bond absorptions between 770 and 820 cm^{-1} (Ding *et al.*, 2016; Qin *et al.*, 2016).

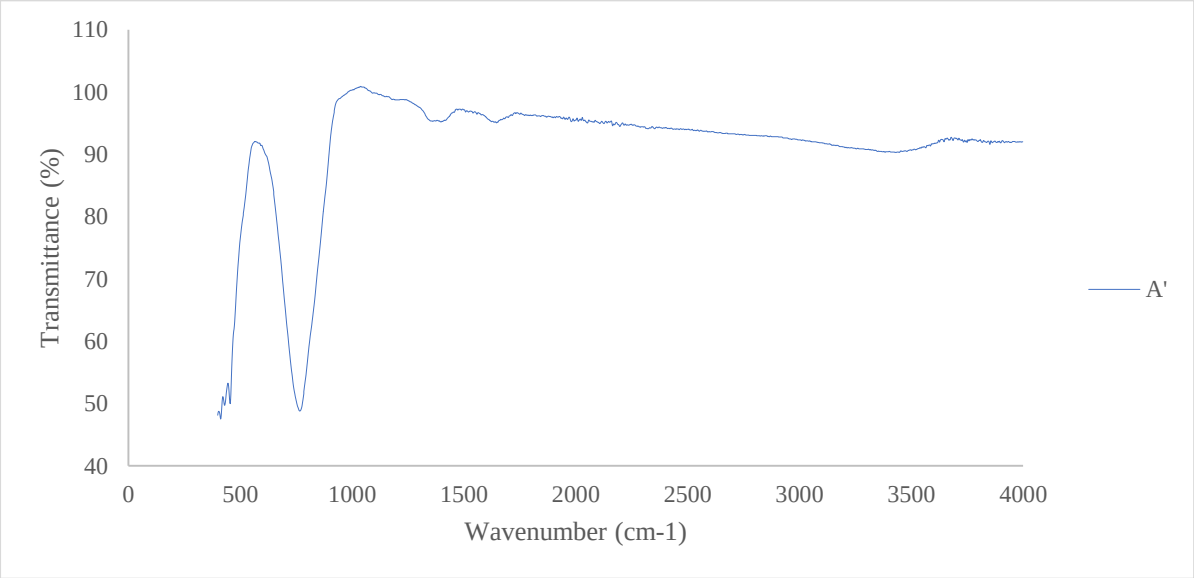

Figure 5.4: IR spectrum of Sample A.

On the FTIR spectra of Cu-doped materials using starch as a template (Figure 5.5, Table 5.2), the Li-O stretching bands were found to be around 443.28 - 454.3 cm^{-1}. The bands observed between 500 and 800 cm^{-1} are associated with the stretching vibrations of V=O bonds of the VO_4 tetrahedra. The IR modes at 500–600 cm^{-1} are assigned to the asymmetric V-O-V stretching vibrations. Some samples are hygroscopic, as shown by the weak O-H band at about 3500 cm^{-1} (Nithya *et al.*, 2012). The absorption peak at around 1300 and 1800 cm^{-1} is assigned to C-C (Priyono *et al.*, 2018; Barboux *et al.*, 1991).

© University of Venda

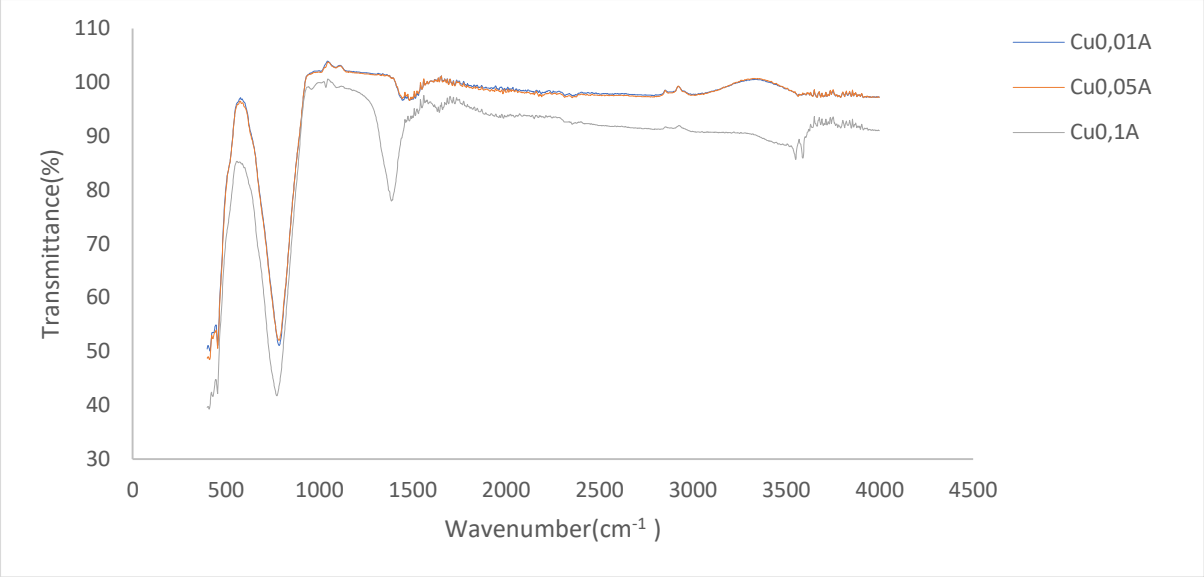

Figure 5.5: IR spectra of Samples CuA.

Table 5.2: IR spectral data (cm^{-1}) of $Li_3Cu_xV_{1-x}O_4$ using starch.

	Li-O	**V=O**	**Cu-O-Li**	**V-O-V**
$Li_3Cu_{0.01}V_{0.99}O_4$	455.13	1018.28	1392.17	777.52
$Li_3Cu_{0.05}V_{0.95}O_4$	443.28	1016.87	1472.90	801.603
$Li_3Cu_{0.1}V_{0.9}O_4$	463.14	1018.97	1419.08	811.10

The IR data of the FeA samples reported in Figure 5.6 and Table 5.3 show the absorption bands for Li-O bond stretching at 4029.74 to 414.34 cm^{-1}. The bands at 1083 to 1094 cm^{-1} are associated with the stretching vibrations of V=O bonds of the VO_4 tetrahedra. The IR modes at 778.94-779 cm^{-1} and 1632.72-1648.36 cm^{-1} are assigned to the asymmetric stretching vibration of the transition metal oxides, V-O-V and V-O-Fe, respectively. With increasing dopant Fe concentration, the Li-O bond stretching intensity decreases, with an increase of the Li-O-Fe and V-O-V intensities (Lu *et al*., 1999; Qin *et al*., 2016).

© University of Venda

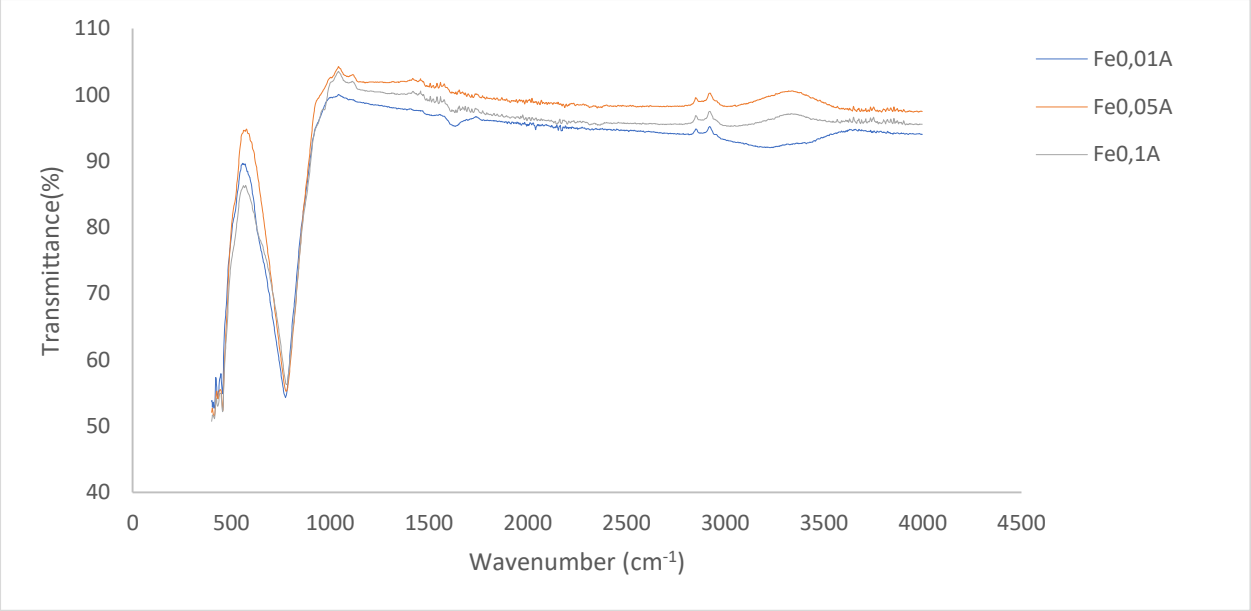

Figure 5.6: IR spectra of Samples FeA.

Table 5.3: IR spectral data (cm^{-1}) of $Li_3Fe_xV_{1-x}O_4$ using starch.

Sample	Li-O	V=O	Fe-O-Li	V-O-V
$\mathbf{Li_3Fe_{0.01}V_{0.99}O_4}$	414.34	1083.43	1645.24	778.94
$\mathbf{Li_3Fe_{0.05}V_{0.95}O_4}$	409.24	1094.63	1632.72	786.49
$\mathbf{Li_3Fe_{0.1}V_{0.9}O_4}$	411.74	1089.15	1648.36	779.02

5.1.3 Structure characterization

The XRD patterns of undoped and doped LVO materials (Figure 5.7a) show sharp diffraction peaks for Li_3VO_4 at 19.42, 25.40, 26.92, 28.66, 33.19, 38,61, 42.80, and 44.33° with the Miller indices of 100, 110, 011, 101, 111, 200, 002, and 201, respectively. These peaks correspond to the crystal faces of orthorhombic Li_3VO_4 (JCPDS, no. 38–1247, Figure 5.7b) (Zhou *et al.*, 2016; Zhang *et al.*, 2015). Diffraction peaks for copper and iron were not detected due to the low Cu and Fe content, but a small shift in the values of the peaks was observed as the dopant metal was added. The crystallinity of the particles was determined using the Debye-Scherrer equation, shown in Table 5.4. The results suggest orthorhombic Li_3VO_4 was successfully prepared (Liu *et al.*, 2015).

© University of Venda

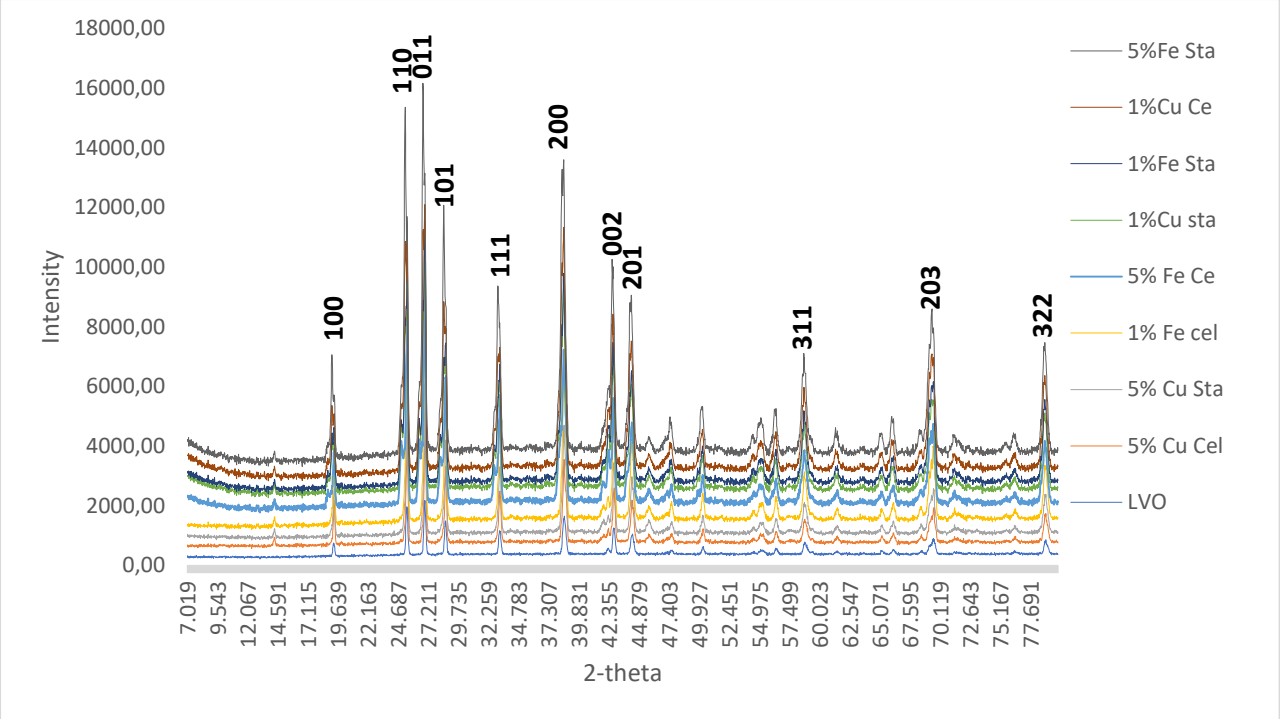

(a)

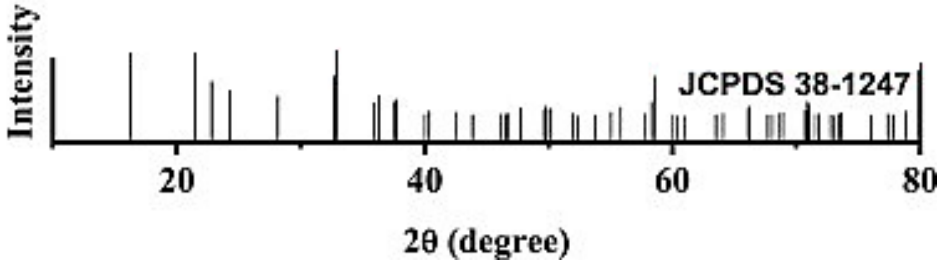

(b)

Figure 5.7: XRD patterns of (a) the as-prepared products (sta = starch-assisted, ce = cellulose-assisted); (b) JCPDS 38-1247.

Table 5.4: Crystallite sizes of undoped and doped LVO samples.

Sample Code	Crystallite size (nm)
A	60.3
Cu0.05A	39.5
Cu0.05B	92.8
Fe0.05A	29.0
Fe0.05B	21.6
Cu0.01A	77.5
Cu0.01B	64.6
Fe0.01A	21.6
Fe0.01B	78.1

© University of Venda

The XRD of undoped LVO (Sample A, Figure 5.8a) has intense and sharp diffraction peaks, indicating a high crystallinity, as reported before (Liu *et al.*, 2015). The sample crystalized in the orthorhombic Li_3VO_4 structure without any impurity. The SEM image (Figure 5.8b) of undoped LVO (Sample A) shows numerous micro-flakes ranging in size from 0.8 µm – 22 µm. The surfaces of these particles are rough (Song *et al.*, 2016; Zhang *et al.*, 2020; Qin *et al.*, 2016), as illustrated by the TEM (Figure 5.8c). The undoped LVO EDS spectrum (Figure 5.8d) reveals that the product is mainly composed of C, V, O and Cu. However, Cu appears in all samples due to the use of a copper grid during TEM analysis. Ultra-soft Li K X-rays represent a detection challenge for standard EDS systems. The X-ray signal generated is low and the probability of absorption high, therefore emitted intensity is small and thus, lithium is not visible on EDS spectra (Babu *et al.*, 2018; Johnson *et al.*, 2016).

The XRD of 1% Cu-doped LVO (Figure 5.9a) also has intense and sharp diffraction peaks, indicating a high crystallinity. The sample crystalized in the orthorhombic Li_3VO_4 structure without any impurity. The SEM image (Figure 5.9b) shows up to 10 µm-sized particles. It can be clearly seen that the particle size has decreased. This confirms that introducing dopant metal has an effect on the structure of LVO. The surfaces of these particles are relatively smooth and seem to be coated by a 3 nm layer of amorphous carbon (Zakharova *et al.*, 2019), as illustrated by the TEM (Figure 5.9c).

© University of Venda

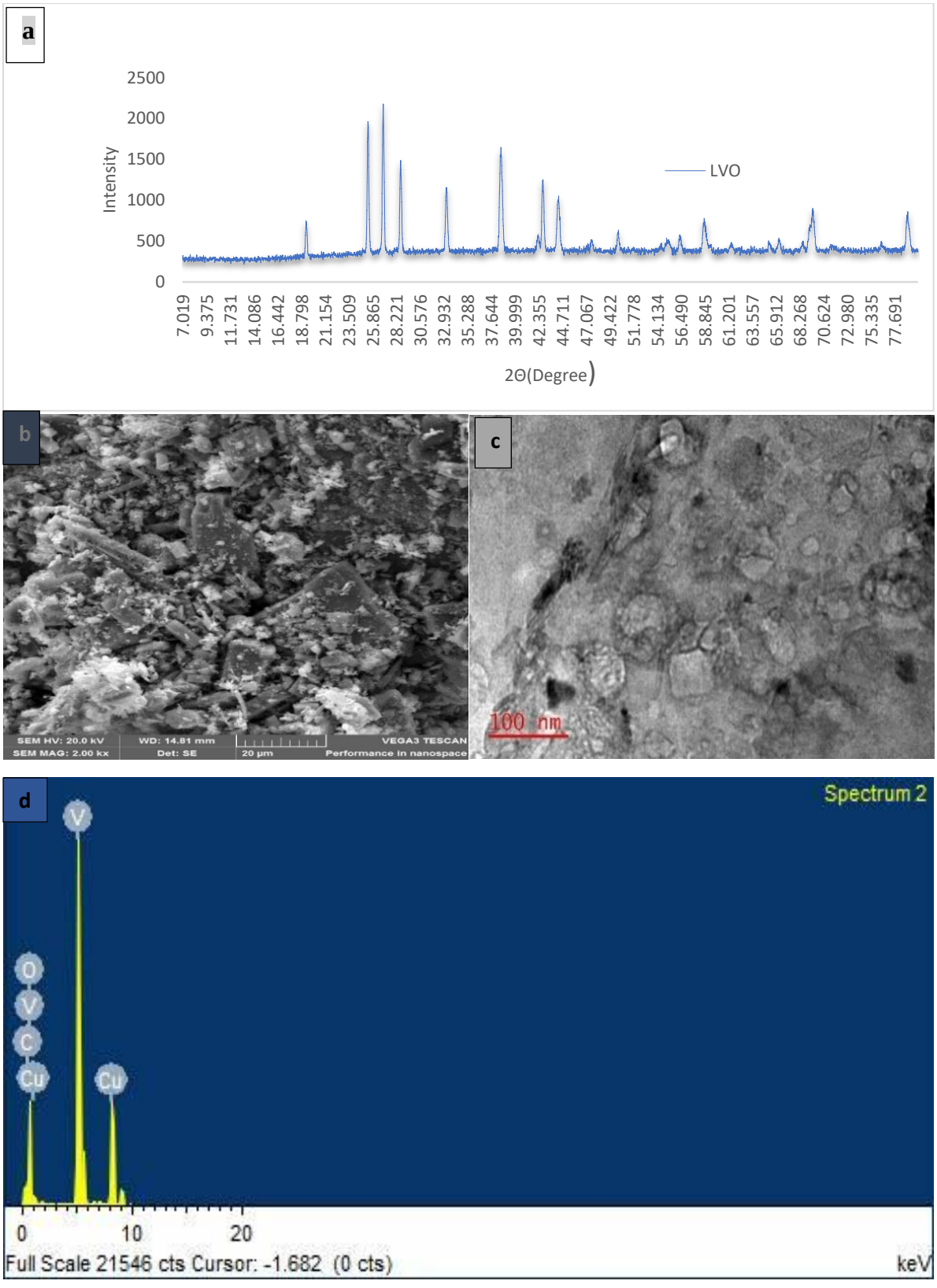

Figure 5.8: Structural characterization of undoped LVO (A). (a) XRD pattern, (b) SEM image, (c) TEM image, and (d) EDS spectrum.

© University of Venda

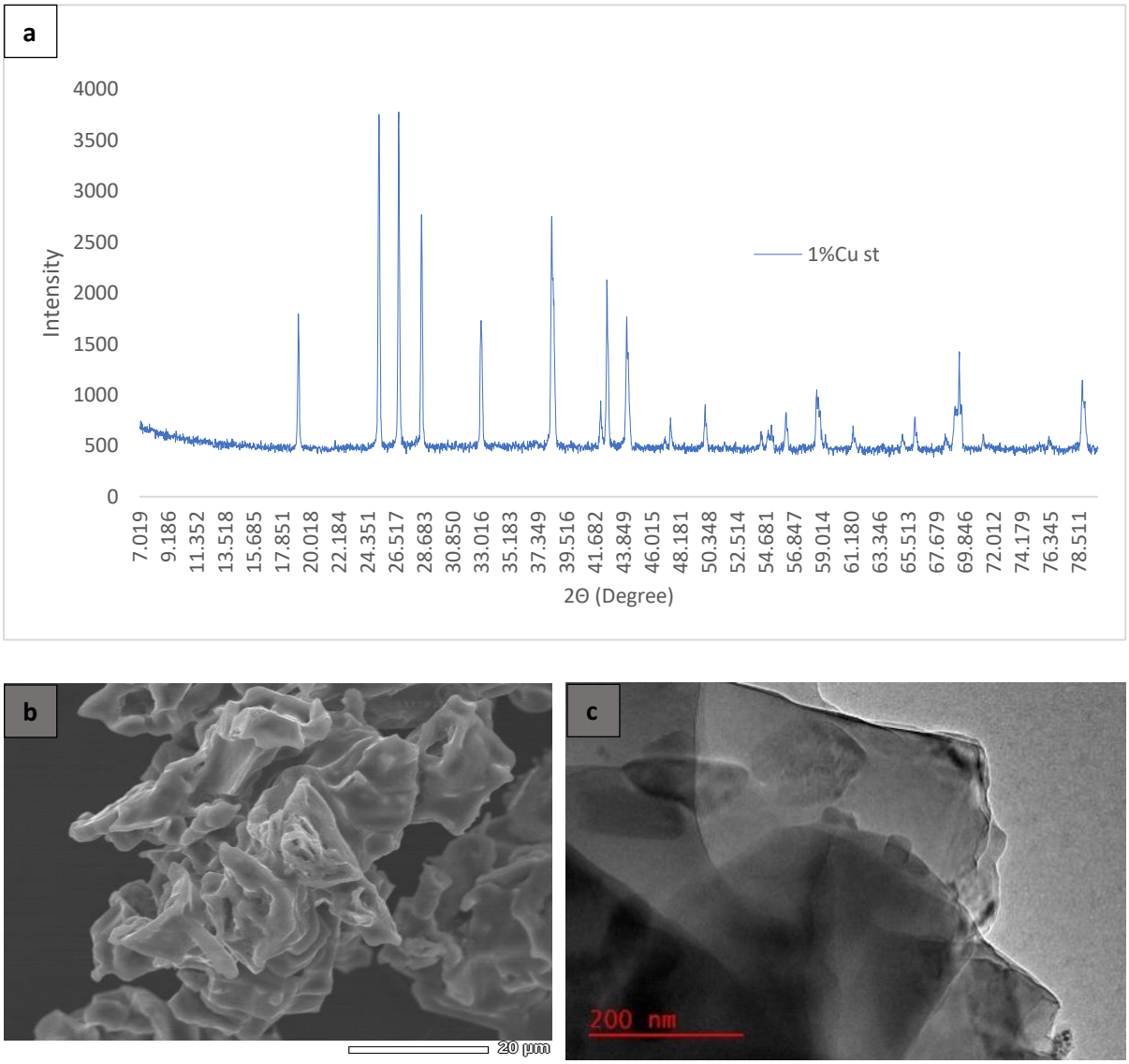

Figure 5.9: Physical characterization of 1% Cu-LVO. (a) XRD pattern, (b) SEM image, and (c) TEM image.

The XRD of 1% Fe-doped LVO (Figure 5.10a) has intense and sharp diffraction peaks, indicating a high crystallinity. The sample crystalized in the orthorhombic Li_3VO_4 structure without any impurity. The SEM image (Figure 5.10b) shows numerous micro-flakes ranging in size from 0.8 µm – 22 µm. The surfaces of these particles are relatively smooth, as illustrated by the TEM (Figure 5.10c).

© University of Venda

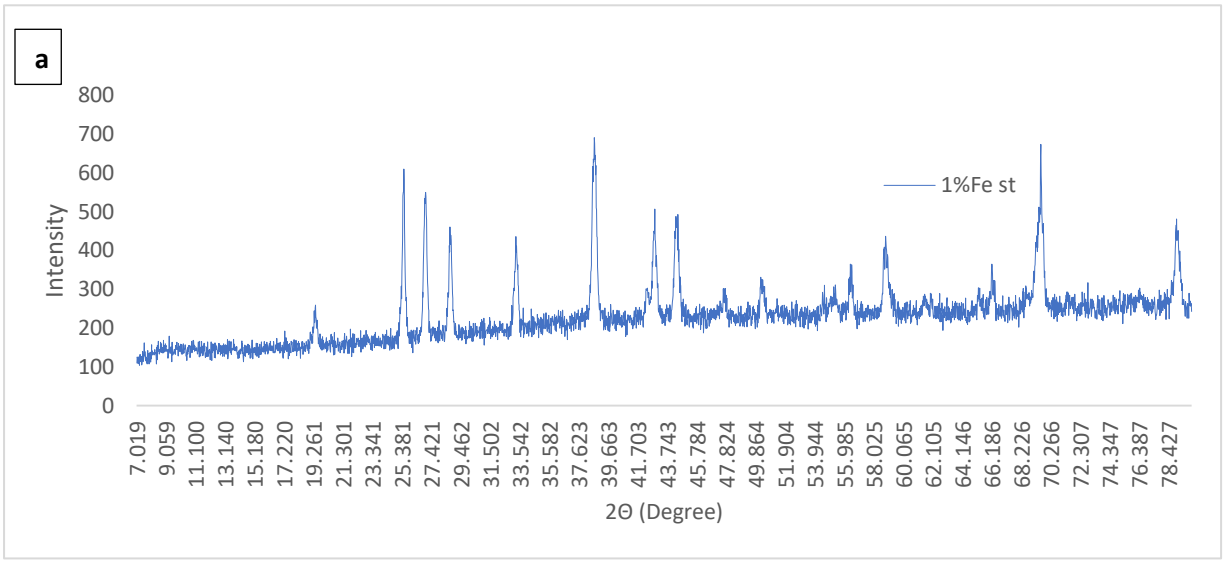

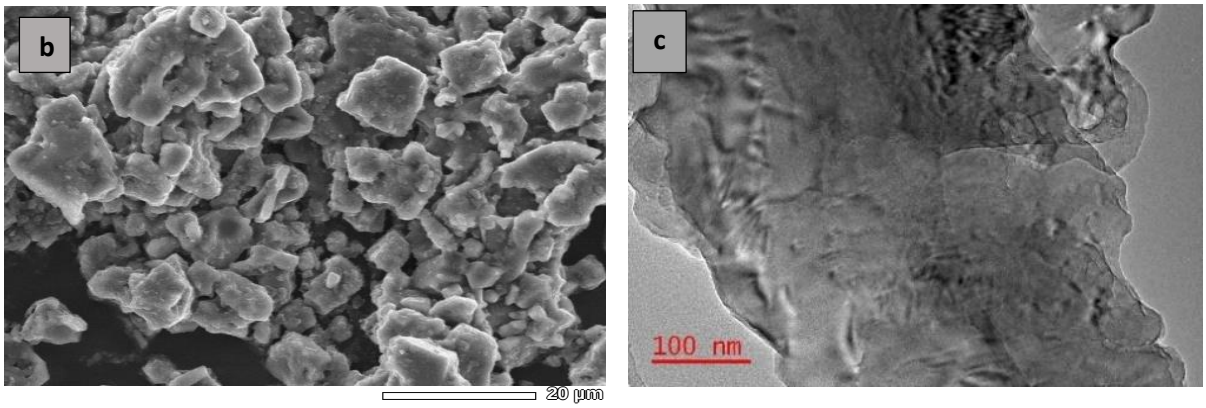

Figure 5.10: Physical characterization of 1% Fe-LVO. (a) XRD pattern, (b) SEM image, and (c) TEM image.

The XRD of 5% Cu-doped LVO (Figure 5.11a) has intense and sharp diffraction peaks, indicating a high crystallinity. The sample crystalized in the orthorhombic Li_3VO_4 structure without any impurity. In the SEM image (Figure 5.11b) agglomerated micron- and submicron-sized particles can be seen, forming a material with a relatively large specific surface area. The EDS spectrum (Figure 5.11c) reveals that the product is mainly composed of C, V, O and Cu.

© University of Venda

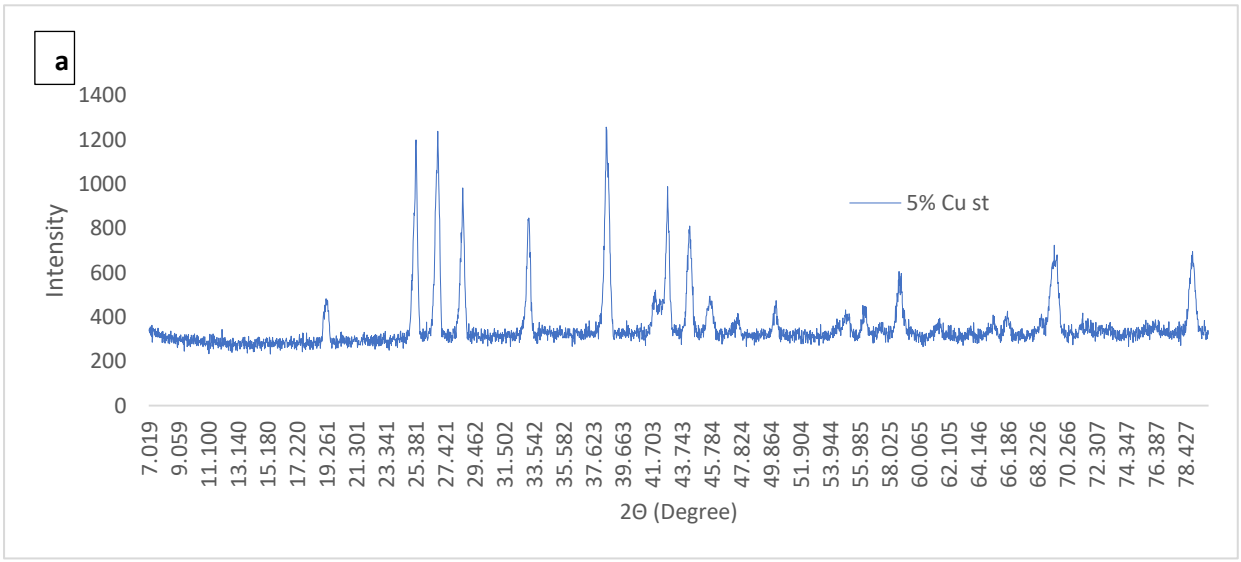

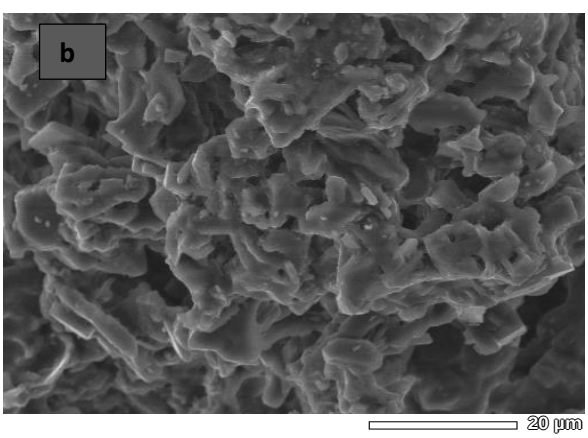

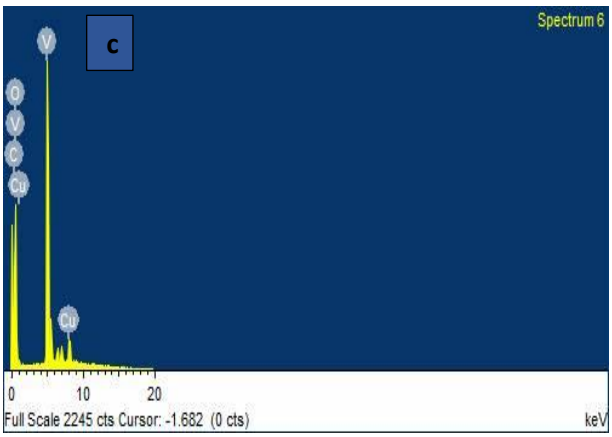

Figure 5.11: Physical characterization of 5% Cu-LVO. (a) XRD pattern, (b) SEM image, and (c) EDS spectrum.

The XRD of 5% Fe-doped LVO (Figure 5.12a) has intense and sharp diffraction peaks, indicating a high crystallinity. The sample crystalized in the orthorhombic Li_3VO_4 structure without any impurity. The SEM image (Figure 5.12b) shows clusters with irregular shape in sizes up to 10 µm. The surfaces of these particles are rough. The EDS spectrum (Figure 5.12c) reveals that the product is mainly composed of C, V, O and Fe.

© University of Venda

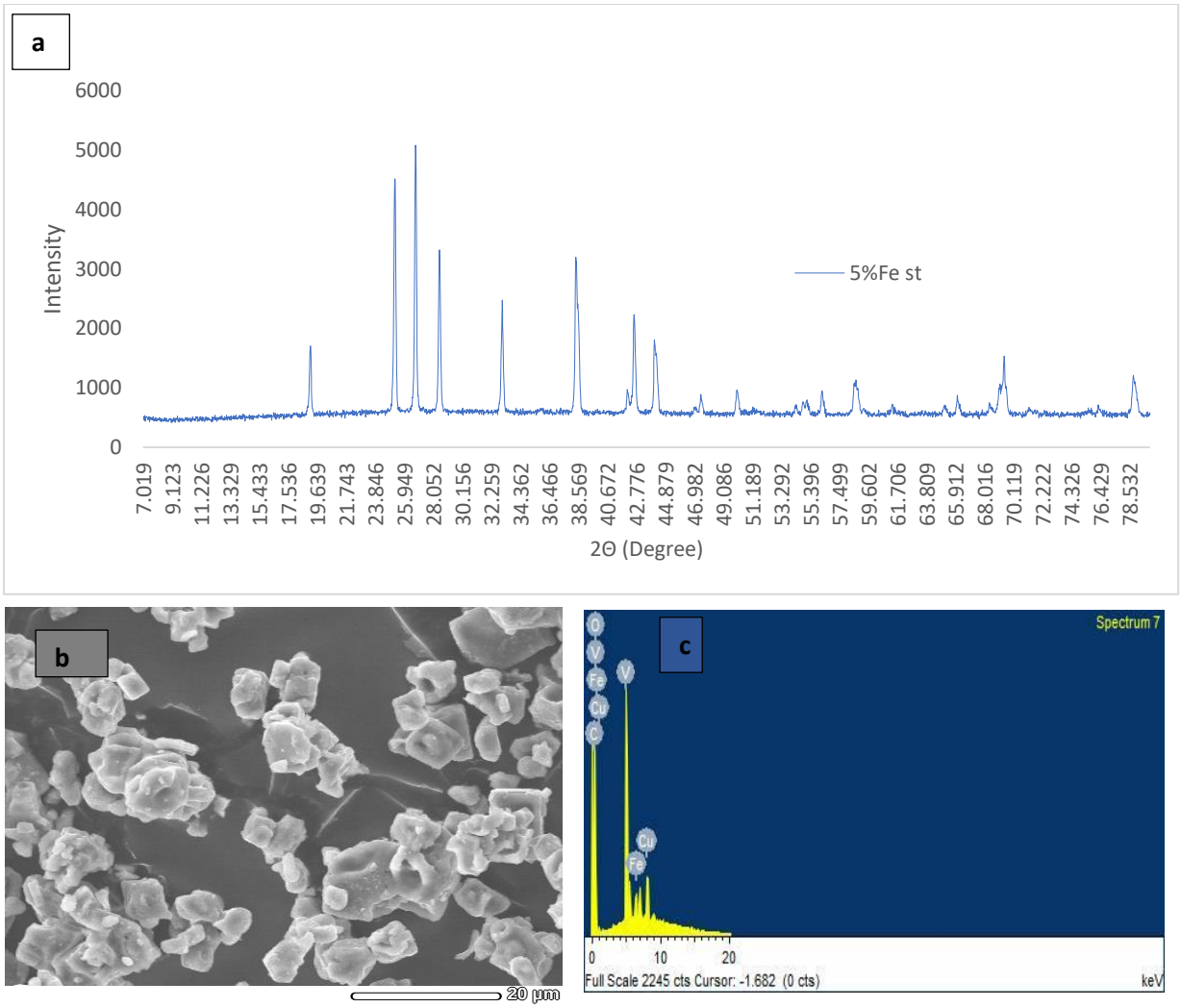

Figure 5.12: Physical characterization of 5% Fe-LVO. (a) XRD pattern, (b) SEM image, and (c) EDS spectrum.

5.2 LVO and doped LVO prepared using cellulose as template

5.2.1 TGA and DTG results

The TGA and DTG plots for Sample CuB on Figure 5.13 show three main endothermic peaks; the first two peaks at 76.26°C and 357.59°C are assigned to loss of physically and chemically bound water, and there is a peak at 578.49°C assigned to the decomposition of $LiNO_3$ with release of NO_2.

The DTG plot of Sample FeB in Fig 5.14 shows three main endothermic peaks at around 65.95°C, 363.26°C, and 534.04°C. The first two peaks are assigned to the physically and chemically bound water and the last peak is assigned to the pyrolysis of cellulose and $LiNO_3$.

© University of Venda

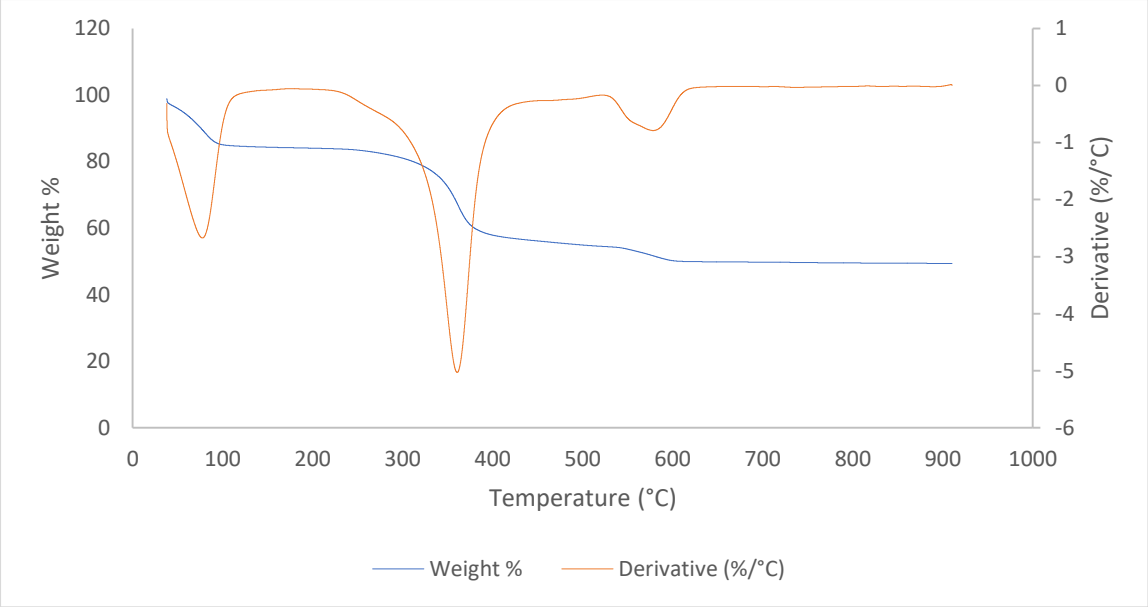

Figure 5.13: TGA and DTG of 5% Cu-LVO.

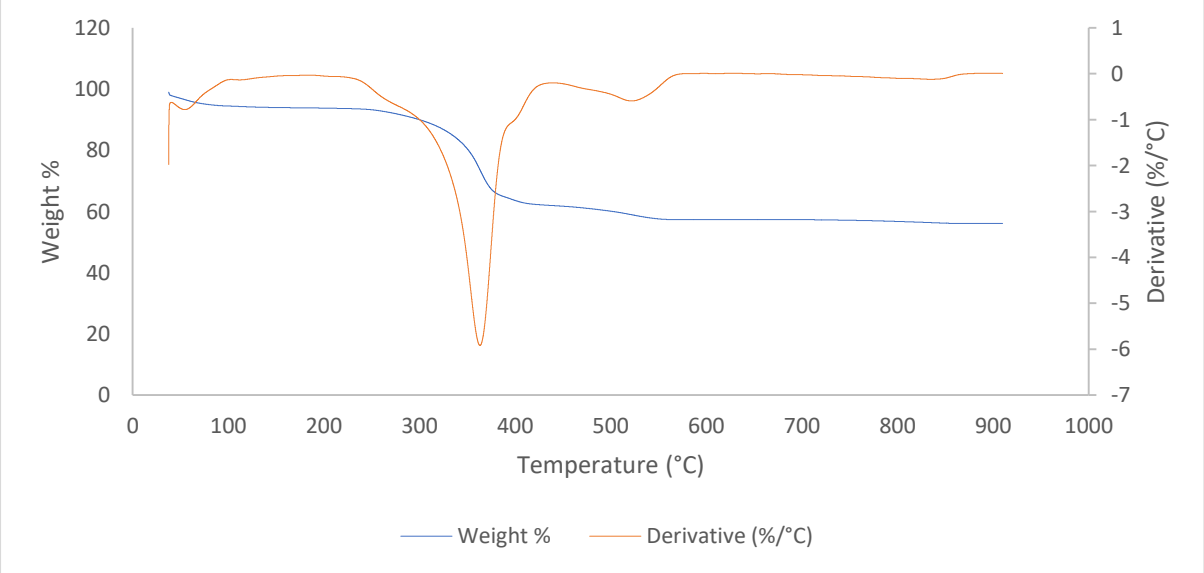

Figure 5.14: TGA and DTG analysis of 5% Fe-LVO.

5.2.2 IR results

Figure 5.15 shows the IR results of Sample B using cellulose as template. The absorption bands for Li-O are at 399.45 and 454.37 cm^{-1}, respectively with an asymmetric stretching vibration of the transitional metals. The bands between 500 and 777.68 cm^{-1} are associated with the stretching vibrations of V=O bonds of the VO_4 tetrahedra. The weak absorption at around 3434.86 cm^{-1} is assigned to -OH due to hydroscopic activity of the Fe containing oxide. As the concentration of the dopant increases the V=O absorption band shifts to higher frequencies (Ding *et al*., 2016; Dimitrov *et al*., 1994; Di Noto *et al*., 2012).

© University of Venda

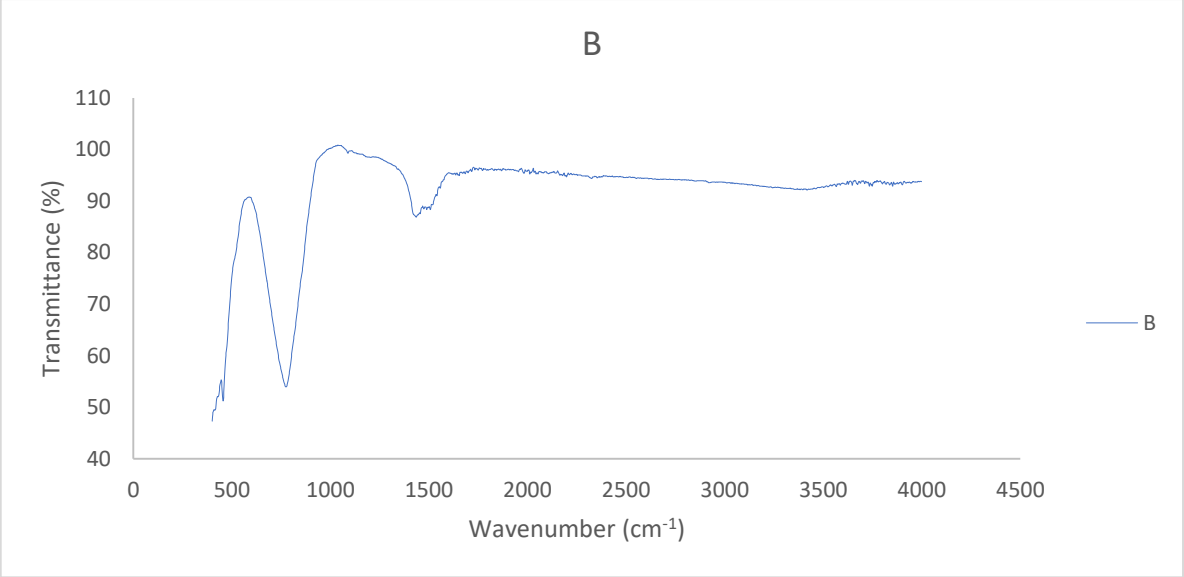

Figure 5.15: IR spectrum of Sample B prepared using cellulose as template.

Figure 5.16 and Table 5.5 display the IR data of Cu-doped LVO using cellulose as a template The Li-O stretching bands were found to be around 405.36-454.61 cm^{-1}. The bands observed between 500 and 800 cm^{-1} are associated with the stretching vibrations of V=O bonds of the VO_4 tetrahedra. The IR modes at 771.24–792.14 cm^{-1} are assigned to the asymmetric V-O-V stretching vibrations. The Cu-O-Li vibration is found at 1434.17-1444.58 cm^{-1} (Di *et al.*, 2014).

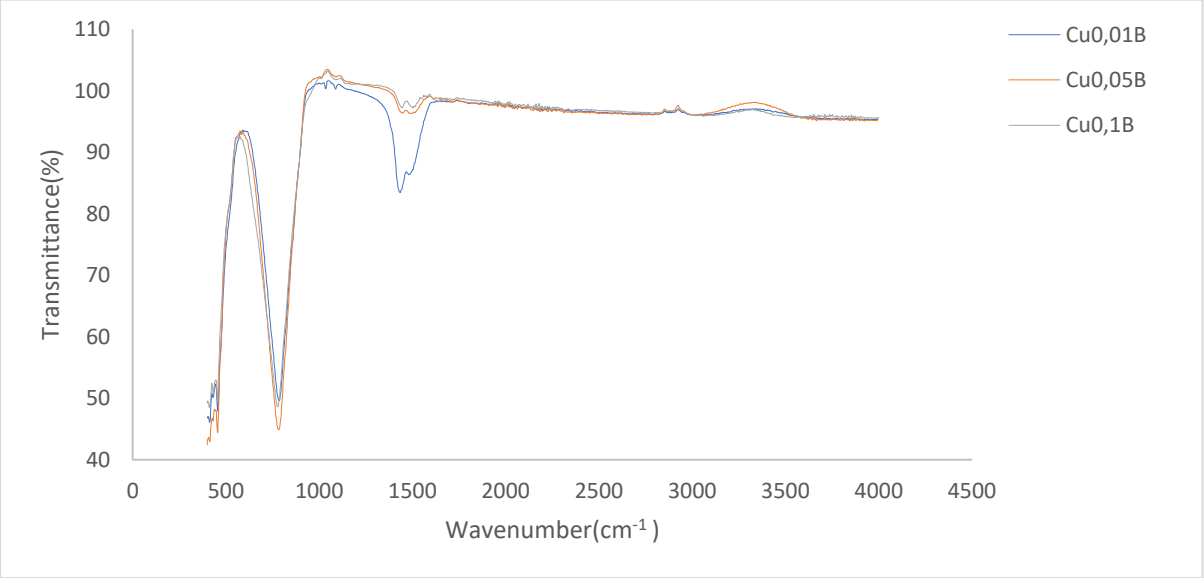

Figure 5.16: IR spectra of Samples CuB.

© University of Venda

Table 5.5: IR spectral data (cm^{-1}) of $Li_3Cu_xV_{1-x}O_4$ prepared using cellulose.

	Li-O	**V=O**	**Cu-O-Li**	**V-O-V**
$Li_3Cu_{0.01}V_{0.99}O_4$	405.36	1022.46	1434.17	792.14
$Li_3Cu_{0.05}V_{0.95}O_4$	454.61	1004.43	1437.72	781.77
$Li_3Cu_{0.1}V_{0.9}O_4$	424.61	1074.43	1444.58	771.24

The IR data of Fe-doped LVO (FeB) are reported in Figure 5.17 and Table 5.6; the absorption bands for Li-O bond stretching are found at 454 to 457 cm^{-1}. The bands at 1033 to 1036 cm^{-1} are associated with the stretching vibrations of V=O bonds of the VO_4 tetrahedra. The IR modes at 769-782 cm^{-1} and 1334-1363 cm^{-1} are assigned to the asymmetric stretching vibration of the transition metal oxides, V-O-V and V-O-Fe, respectively. With increasing dopant Fe concentration, the Li-O bond stretching intensity decreases, with an increase in the Li-O-Fe and V-O-V intensities (Li *et al*., 2015).

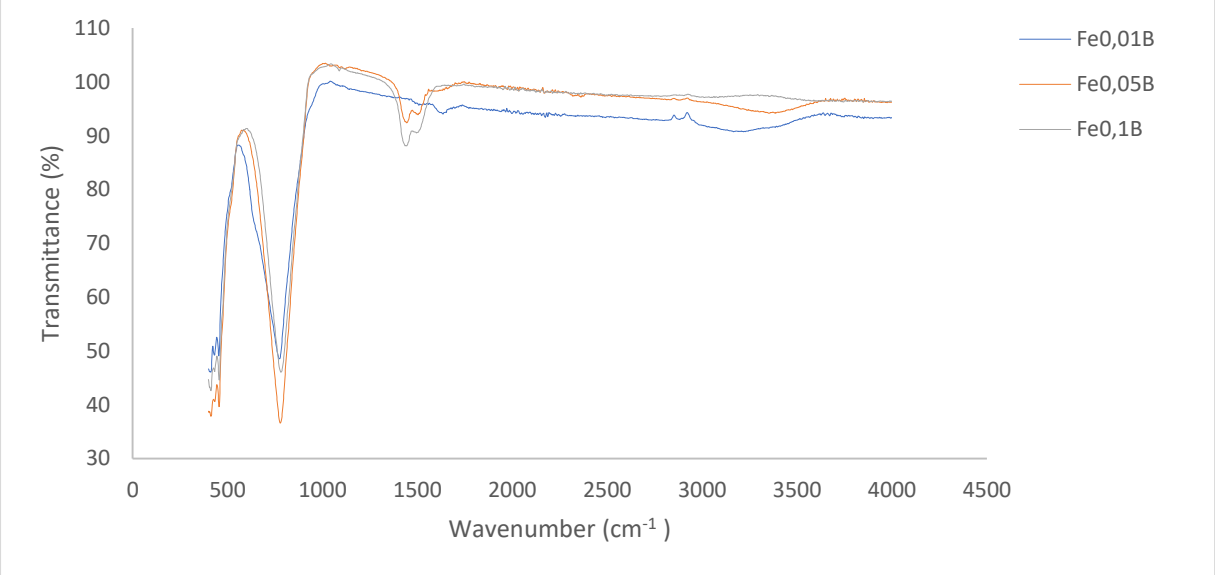

Figure 5.17: IR spectra of Samples FeB.

Table 5.6: IR spectral data (cm^{-1}) of $Li_3Fe_xV_{1-x}O_4$ using cellulose.

	Li-O	**V=O**	**Fe-O-Li**	**V-O-V**
$Li_3Fe_{0.01}V_{0.99}O_4$	417.79	919.14	1526.89	919.14
$Li_3Fe_{0.05}V_{0.95}O_4$	416.37	115124	1445.99	1105.24
$Li_3Fe_{0.1}V_{0.9}O_4$	712.13	1091.93	1445.99	1091.93

All the IR spectra of LVO and Fe- or Cu-doped LVO have similar features. As the amount of added dopant metal increases, it is observed that the absorption bands generally shift to lower frequency or wave number (Ding *et al*., 2016). The intensity of the Li-O band decreases with

© University of Venda

increasing intensity of the Li-O-M (M is Cu or Fe) and V-O-V bands (Liu *et al*., 2020; Kosova *et al*., 2015).

5.2.3 Structure characterization

The XRD of cellulose-assisted 1% Cu-doped LVO (Figure 5.18a) also has intense and sharp diffraction peaks, indicating a high crystallinity. The sample crystallized in the orthorhombic Li_3VO_4 structure without any impurity. The material consists of up to 10 μm-sized flakes accompanied by nanosized particles that are also stacked together, as shown by the SEM image (Figure 5.18b). The surfaces of these particles are relatively smooth, as illustrated by the TEM (Figure 5.18c). The EDS spectrum (Figure 5.18d) reveals that the product is mainly composed of C, V, O and Cu.

The XRD of cellulose-assisted 1% Fe-doped LVO (Figure 5.19a) has intense and sharp diffraction peaks, indicating a high crystallinity. The sample crystalized in the orthorhombic Li_3VO_4 structure without any impurity. The SEM image (Figure 5.19b) shows that the sample consists of aggregates of 10 μm and larger with some nanosized particles. The surfaces of these particles are uneven with cavities, and apparently a 0.4 nm carbon layer covering the particles, as illustrated by the TEM (Figure 5.19c). The EDS spectrum (Figure 5.19d) reveals that the product is mainly composed of C, V, O and Fe.

The XRD of cellulose-assisted 5% Cu-doped LVO (Figure 5.20a) has intense and sharp diffraction peaks, indicating a high crystallinity. The sample crystalized in the orthorhombic Li_3VO_4 structure without any impurity. The SEM image (Figure 5.20b) shows mostly 10 μm-sized flakes accompanied by some nanosized particles. The surfaces of these particles are relatively smooth, as illustrated by the TEM (Figure 5.20c). The EDS spectrum (Figure 5.20d) reveals that the product is mainly composed of C, V, O and Cu with no other elements.

© University of Venda

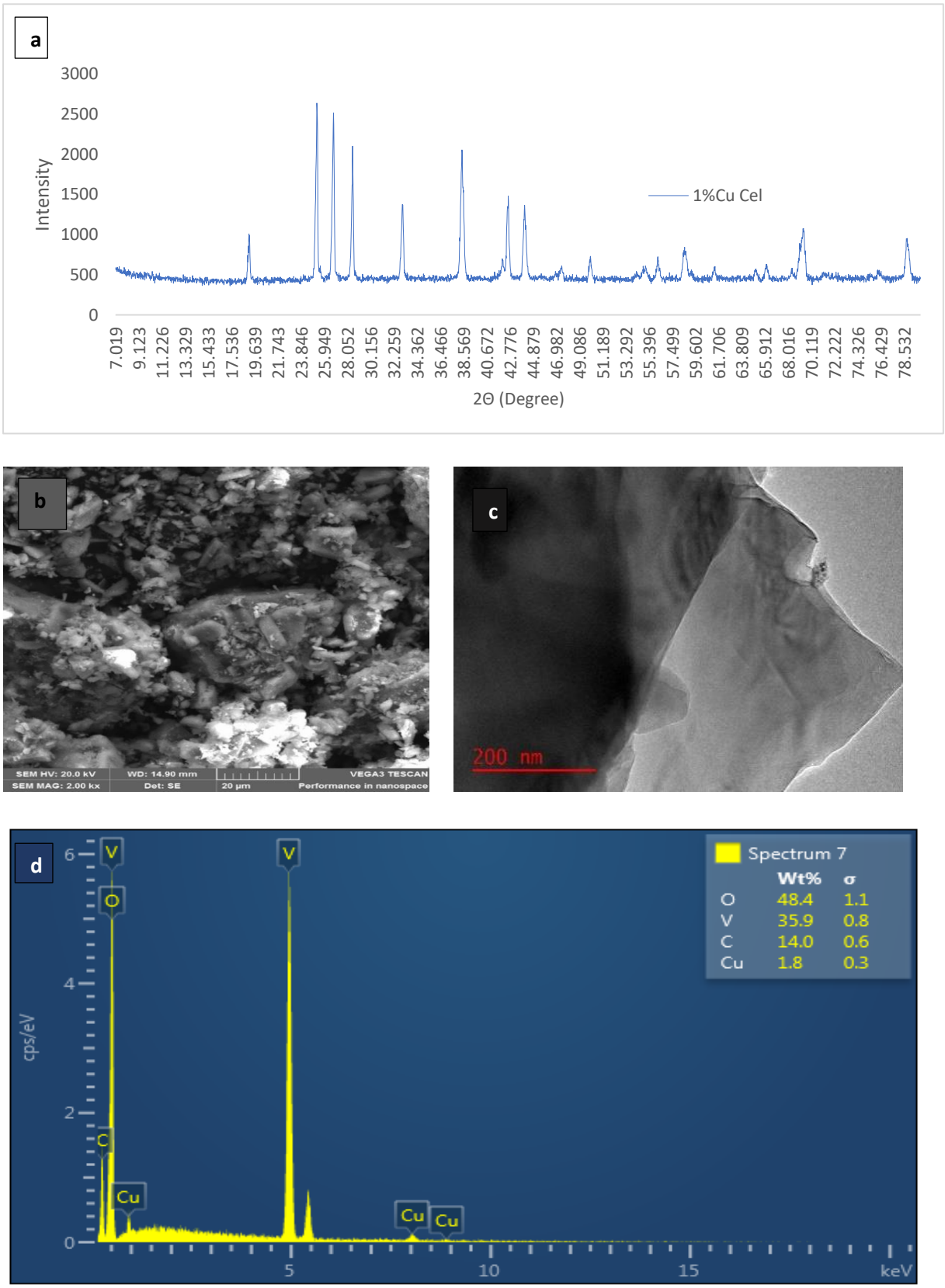

Figure 5.18: Physical characterization of 1% Cu-LVO. (a) XRD pattern, (b)SEM image, (c) TEM image, and (d) EDS spectrum.

© University of Venda

The XRD of cellulose-assisted 5% Fe-doped LVO (Figure 5.21a) also has intense and sharp diffraction peaks, indicating a high crystallinity. The sample crystalized in the orthorhombic Li_3VO_4 structure without any impurity. The SEM image (Figure 5.21b) shows irregular-shaped particles of up to 10 μm size, with relatively smooth surfaces, as illustrated by the TEM (Figure 5.21c). The EDS spectrum (Figure 5.21d) reveals that the product is mainly composed of C, V, O and Fe.

© University of Venda

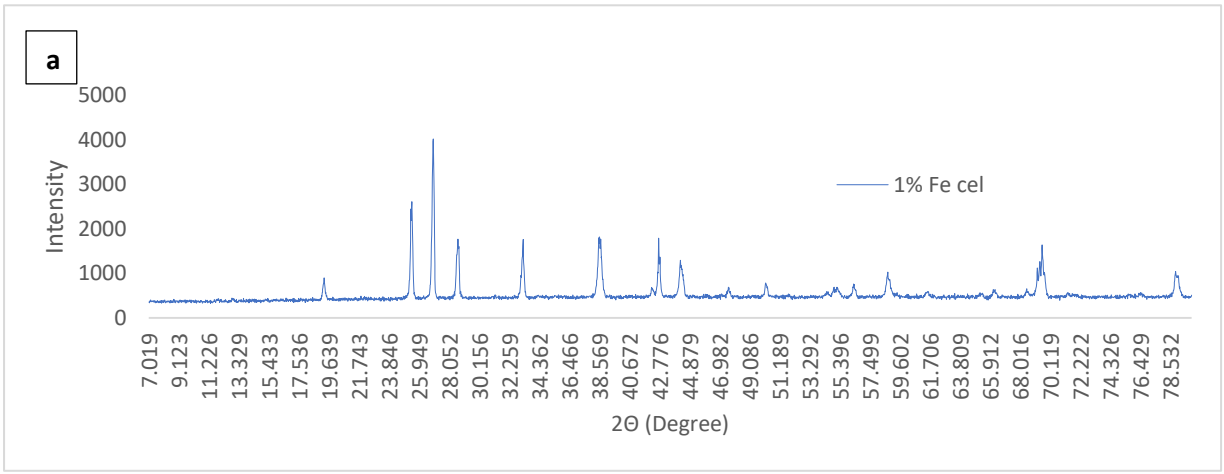

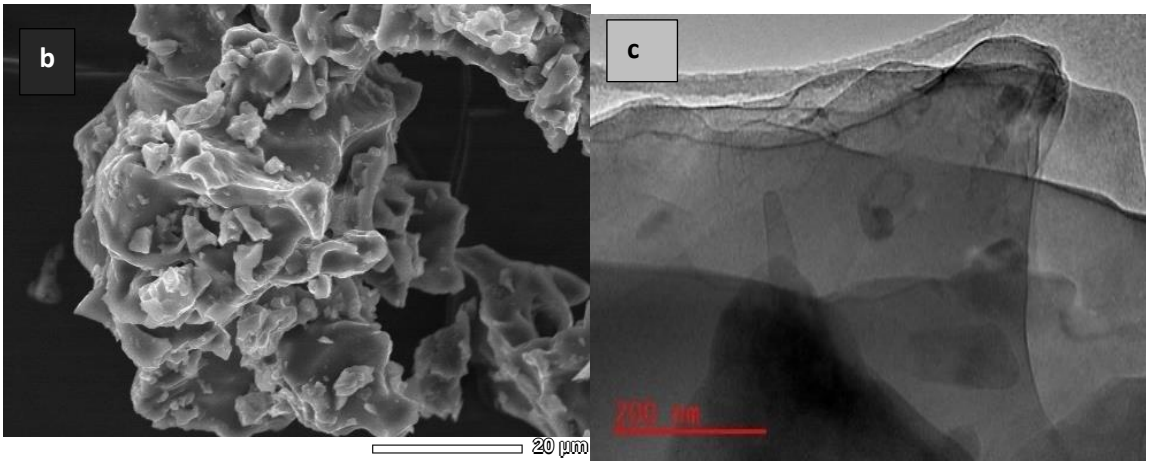

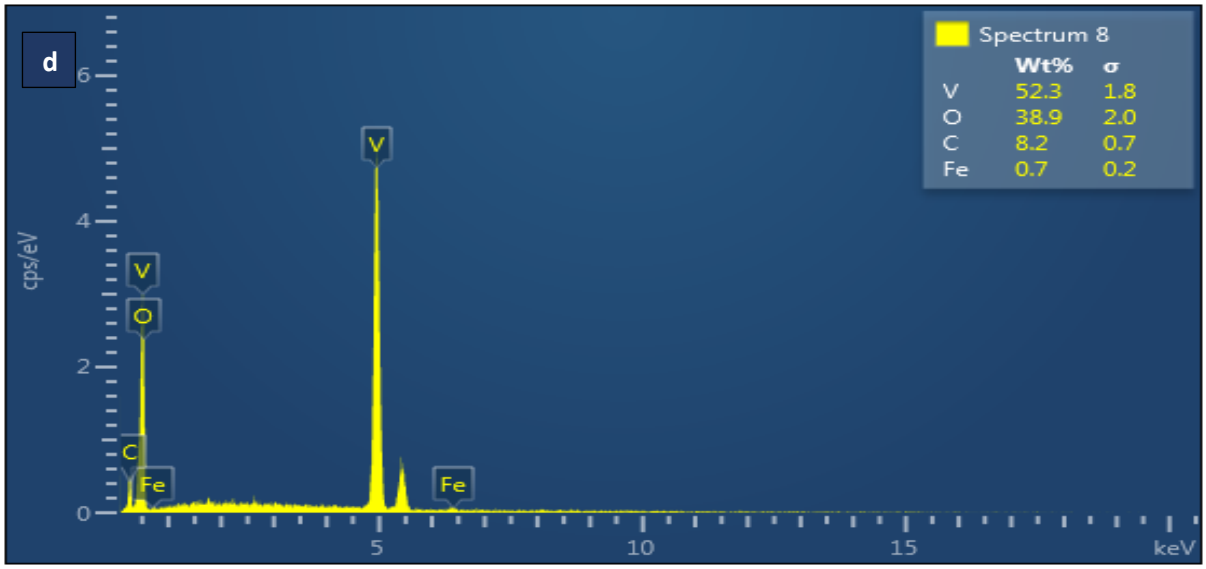

Figure 5.19: Physical characterization of 1%Fe-LVO. (a) XRD pattern, (b) SEM image, (c) TEM image, and (d) EDS spectrum.

© University of Venda

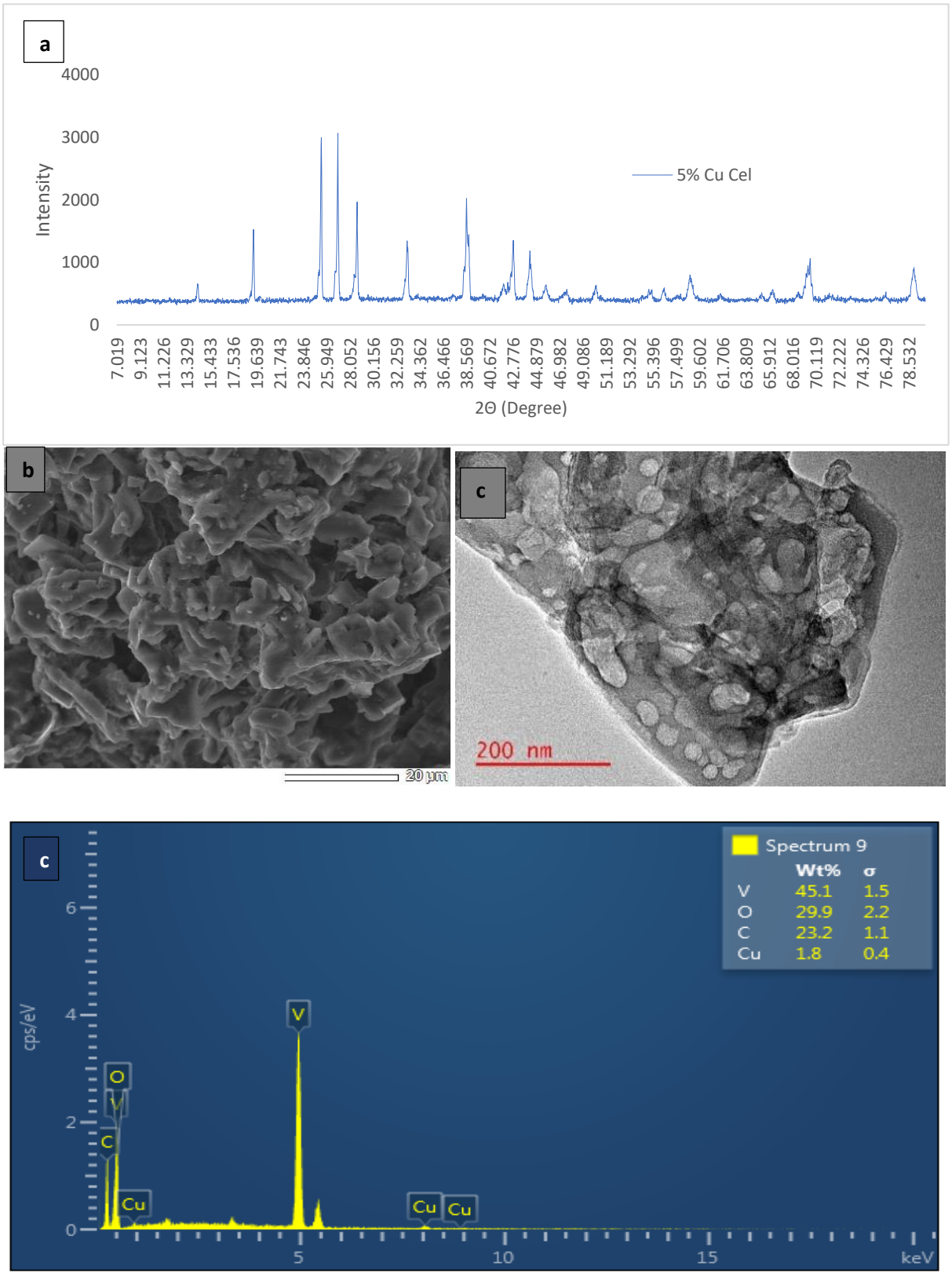

Figure 5.20: Physical characterization of 5% Cu-LVO. (a) XRD pattern, (b)SEM image, (d) TEM image and (e) EDS spectrum.

© University of Venda

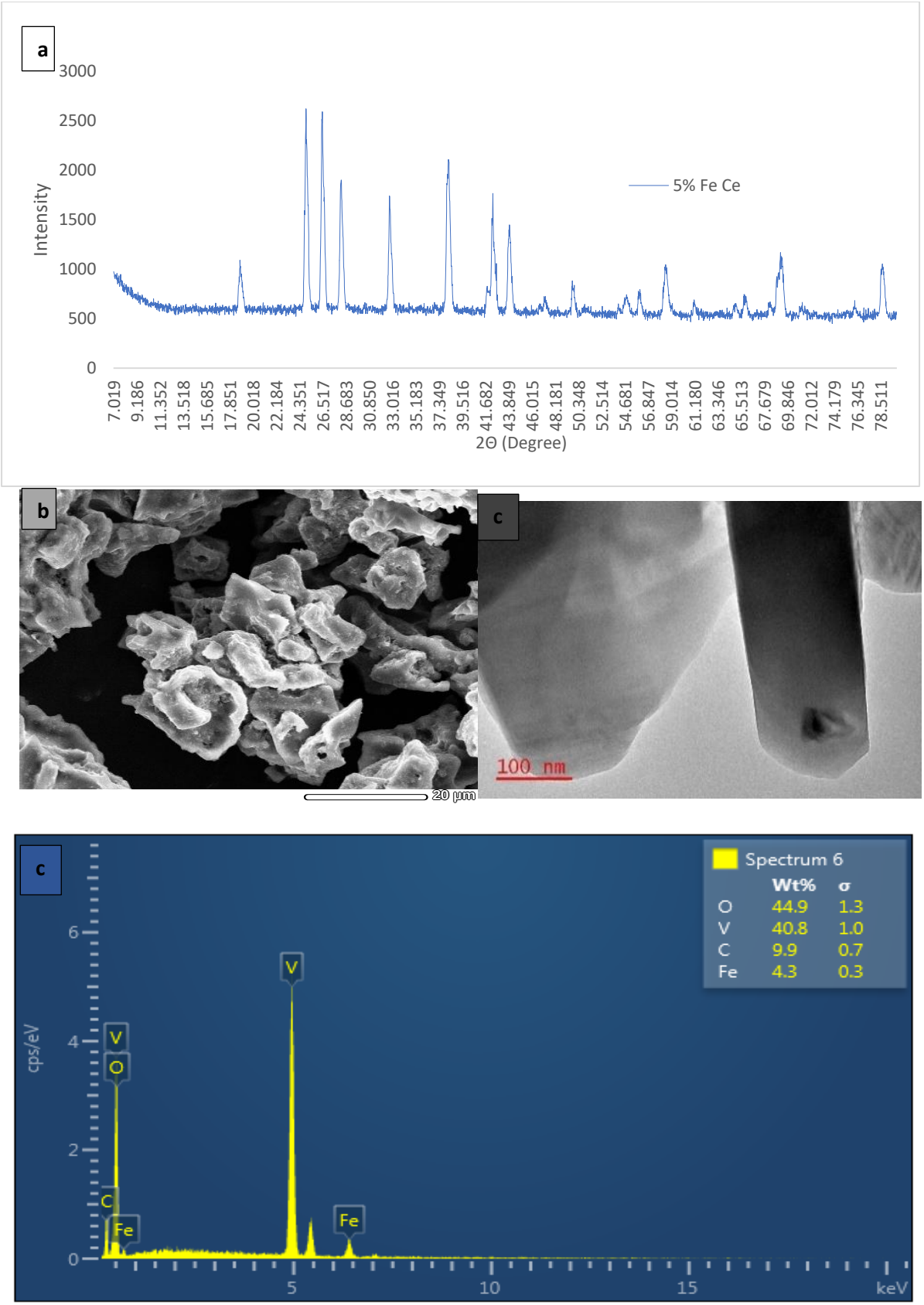

Figure 5.21: Physical characterization of 5% Fe-LVO. (a) XRD pattern, (b) SEM image, (c) TEM image and (d) EDS spectrum.

© University of Venda

5.3 Electrochemical Characterization

For the electrochemical characterization, samples prepared using starch as template, were used. Cyclic voltammetric (CV) measurement from 0.01 to 3.0 V at 0.5 C and a scanning rate of 0.001 Vs^{-1} was used to analyse the detailed electrochemical reaction of the electrode materials upon lithiation and delithiation. Galvanostatic charge/discharge (GCD) tests of the doped Li_3VO_4 were performed between 0.00 and 3.0 V vs. Li^+/Li, and electrochemical impedance spectroscopy (EIS) was performed after cycling the doped LVO electrodes at a rate of 0.5 C for at least 30 cycles.

5.3.1 Cyclic voltammetry (CV)

For the as-prepared Li_3VO_4 (A), the CV (Figure 5.22a) stabilized after the first charge-discharge cycle, showing good reversibility. Similar behaviour was observed for the 1%Cu doped material (Cu0.01A, Figure 5.22b) and 1%Fe doped material (Fe0.01A, Figure 5.22c). This suggests that Cu-doping and Fe-doping do not change the crystal structure of Li_3VO_4. For the three samples, the profiles for the second and subsequent CV curves are similar, differing much from that of the 1st curve.

In the 1st cathodic scan of LVO (Figure 5.22), the reduction peak at 0.466 V corresponds to the formation of SEI. The profiles of CV curves for the 2nd and 3rd cycle are similar, the two main reduction peaks around 0.537 and 0.876 V reflect the lithiation process:

$$xLi^+ + Li_3VO_4 + xe^- \rightleftarrows Li_{3+x}VO_4 \quad (x \leq 3) \tag{8}$$

The reduction peaks for the 1st cycle at 0.373 V and 1.269 V respectively and an oxidation peak at 0.024 and 0.461 V respectively. 2nd Cycle shows that reduction peak at 0.346 V and 1.258 V and an oxidation peak at 0.012 V and 0.749 V, third cycle shows reduction peak at 0.266 and 1.316 V and also an oxidation peak at 0.355 also at 0.738 V. Figure 5.22, for the first cycle it has been observed that reduction peak has occur at 0.261V and 1.253 V respectively and oxidation peak has occur at 0.236 V, second cycle shows that the reduction peak occur at 0.247 V and 1.293 V, also an oxidation peak appear at 0.333V and 0.729V, third cycle shows a reduction peak at 0.226 V and 1.316 V together with the oxidation peak at 0.352V and 0.738V.

The oxidation-reduction cycling pairs were all found to be reversible with regard to the Li^+ insertion/extraction processes (Song *et al.*, 2015). The voltage plateaus for the conversion

© University of Venda

reactions of LVO and Cu-LVO with Li^+ decrease slowly to 0.0000394V. The irreversible reduction peak below 0.468 V for pure LVO and 0.251 V for Cu-LVO in the first cycle, corresponds to the irreversible reduction of electrolyte and the formation of a passivating surface film (Ren, *et all.*, 2020), i.e. the formation of a solid-electrolyte interphase (SEI) layer, during the first charge and discharge processes (Zheng *et al.*, 2015; Zhang *et al.*, 2015), which disappeared in the following cycles.

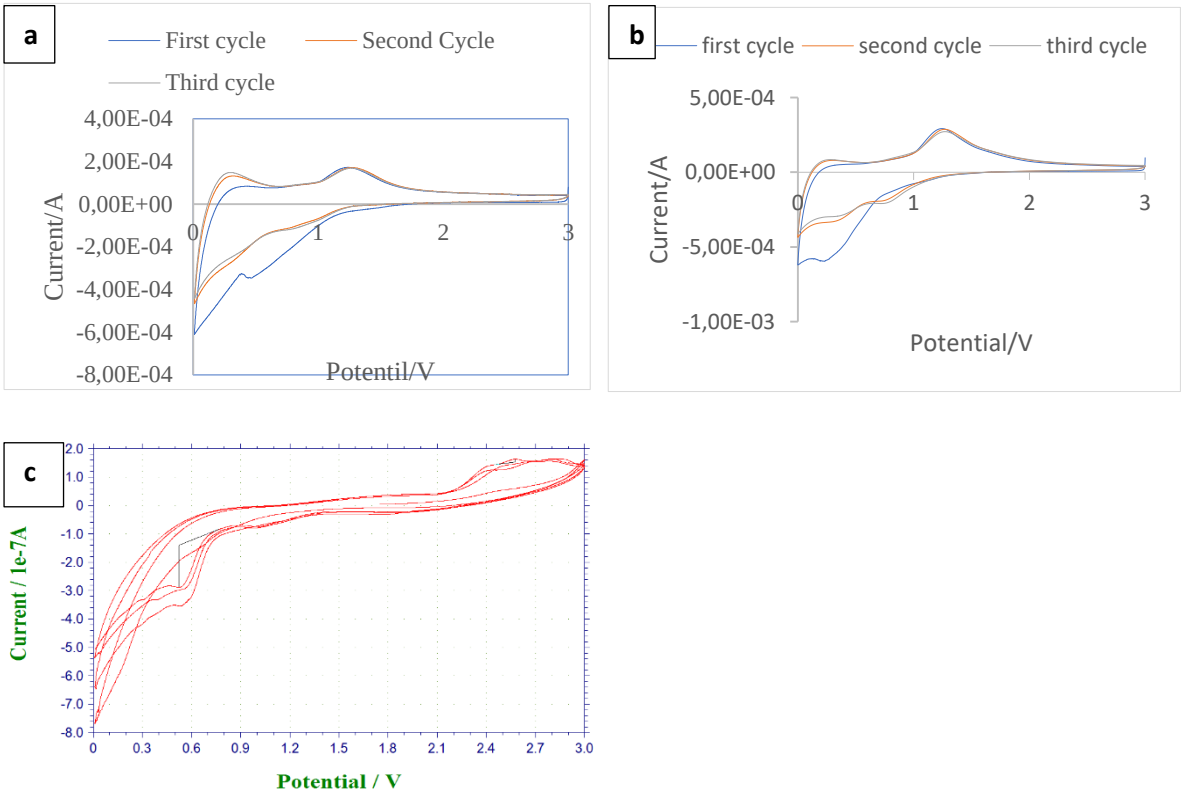

Figure 5.22: Cyclic voltammograms of as-prepared (a) Li_3VO_4 , (b) 1% Cu-LVO, and (c) 1% Fe-LVO material at a scan rate of 1.0 mV s^{-1}.

5.3.2 Charge-discharge curves

Figure 5.23 displays typical discharge and charge curves of the doped LVO electrodes at a rate of 0.5 C. Unstable GCD profiles were observed, especially for 1% Cu-doped material (Figure 5.23a) and 1% Fe-doped material (Figure 5.23c). The specific capacity rapidly decreased from 2.5 to 0.63 mAh g^{-1} for 1% Cu-doped material (Figure 5.23a); from 25 to 11.3 mAh g^{-1} for 5% Cu-doped material (Figure 5.23b); from 28.8 to 16.3 mAh g^{-1} for 1% Fe-doped material (Figure 5.23c); and from 18.8 to 9.4 mAh g^{-1} for 5% Fe-doped material (Figure 5.23d).

© University of Venda

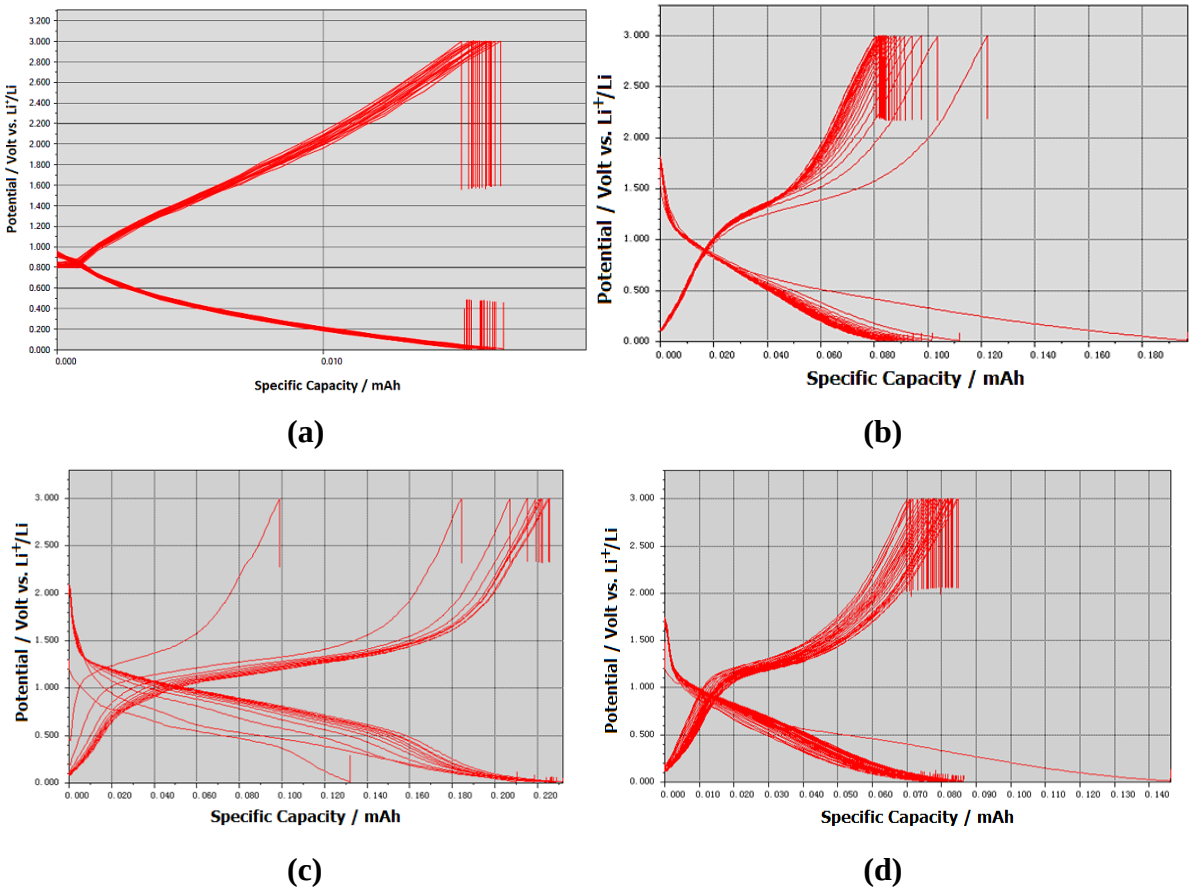

Figure 5.23: Electrochemical performance of Cu- and Fe-doped Li_3VO_4: The charge and discharge curves, at 0.5C, of (a) 1% Cu-doped material; (b) 5% Cu-doped material; (c) 1% Fe-doped material; (d) 5% Fe-doped material.

The rapidly decreasing capacity is most probably due to electrolyte decomposition at low voltage and formation of a solid electrolyte interface (SEI) layer (Liang *et al.*, 2014; Li *et al.*, 2011; Ohzuku *et al.*, 1995; Shi *et al.*, 2013; Wang *et al.*, 2017; Yang *et al.*, 2018). This dramatic capacity decrease implies that the electrochemical performance is not acceptable in the carbonate-based electrolyte.

The doped Li_3VO_4 shows good cycling stability (Figure 5.24), although the capacities are quite low. After an initial decrease, the charge and discharge specific capacity of 1% Cu-doped material reached 11.5 mAh g^{-1} after 170 cycles, with Coulombic efficiency near 100% (Figure 5.24a). With 5% Cu-doped material the specific capacity reached 63 mAh g^{-1} after 28 cycles (Figure 5.24b), while 5% Fe-doped material reached 70 mAh g^{-1} after 30 cycles (Figure 5.24c).

© University of Venda

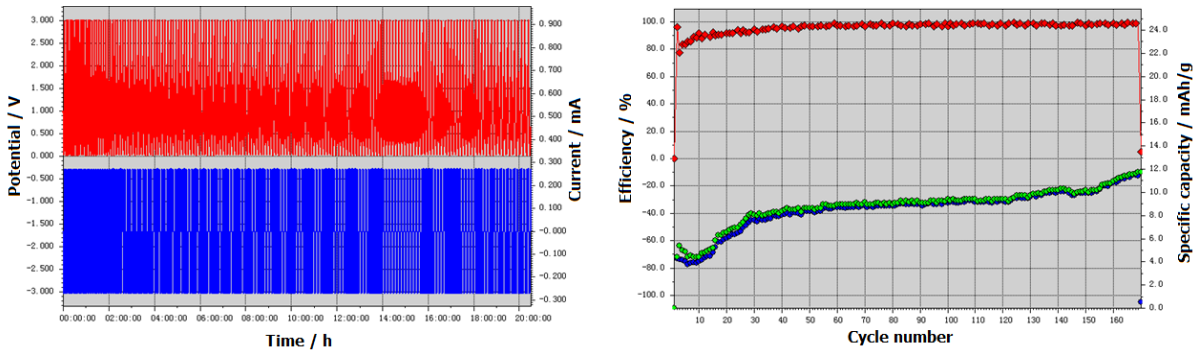

(a)

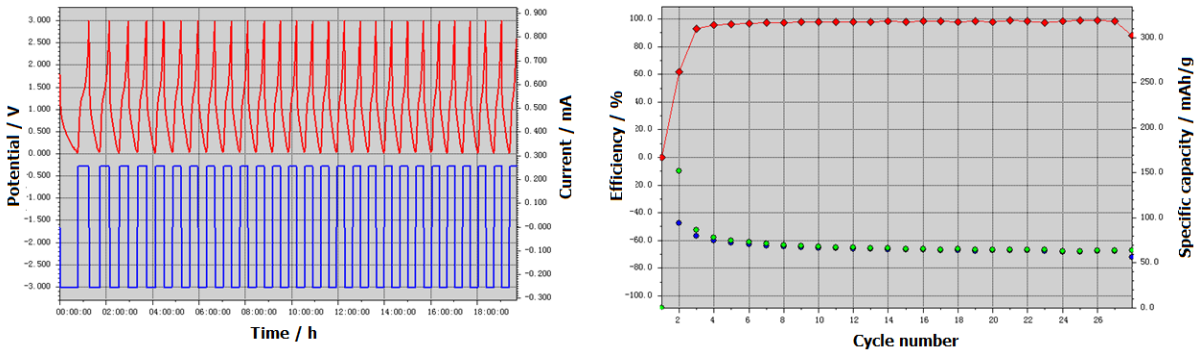

(b)

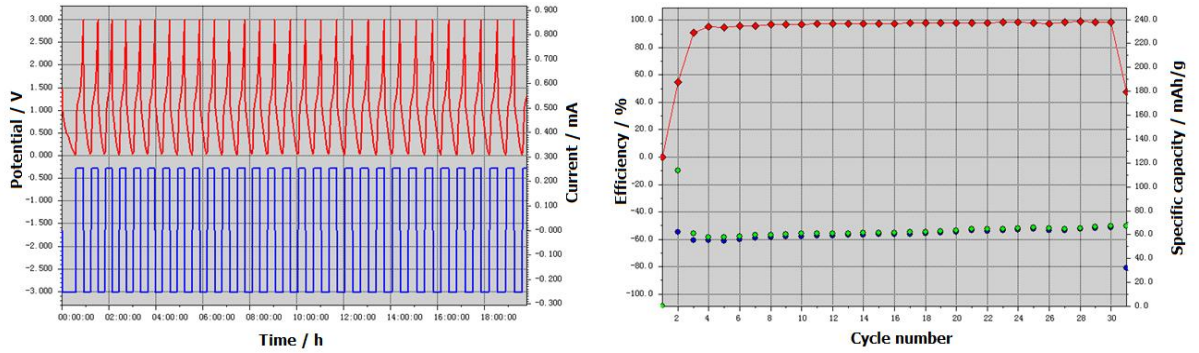

(c)

Figure 5.24: Representative charge/discharge behaviour at 0.5C of: (a) 1% Cu-doped material; (b) 5% Cu-doped material; (c) 5% Fe-doped material.

5.3.3 Electrochemical Impedance Spectroscopy (EIS)

Electrochemical impedance spectroscopy (EIS) was conducted to further investigate the conductivity enhancement and the rate performance of LVO and doped-LVO as negative electrode materials. Figures 5.25 and 5.26 show the EIS plots of Li_3VO_4, $Li_3Cu_{0.05}V_{0.95}O_4$, and $Li_3Fe_{0.05}V_{0.95}O_4$ samples. All the EIS plots exhibit the same shape with a semicircle in the high frequency region and an oblique line in the low frequency region. The semicircle in the high-frequency region is associated with the charge-transfer process and the properties of

© University of Venda

electrochemical reaction resistance, which reflects the resistance to Li^+ ion migration through the electrolyte/electrode interface, and the low frequency straight line relates to the properties of the diffusion process (Xiao *et al*., 2017; Zhang *et al*., 2015).

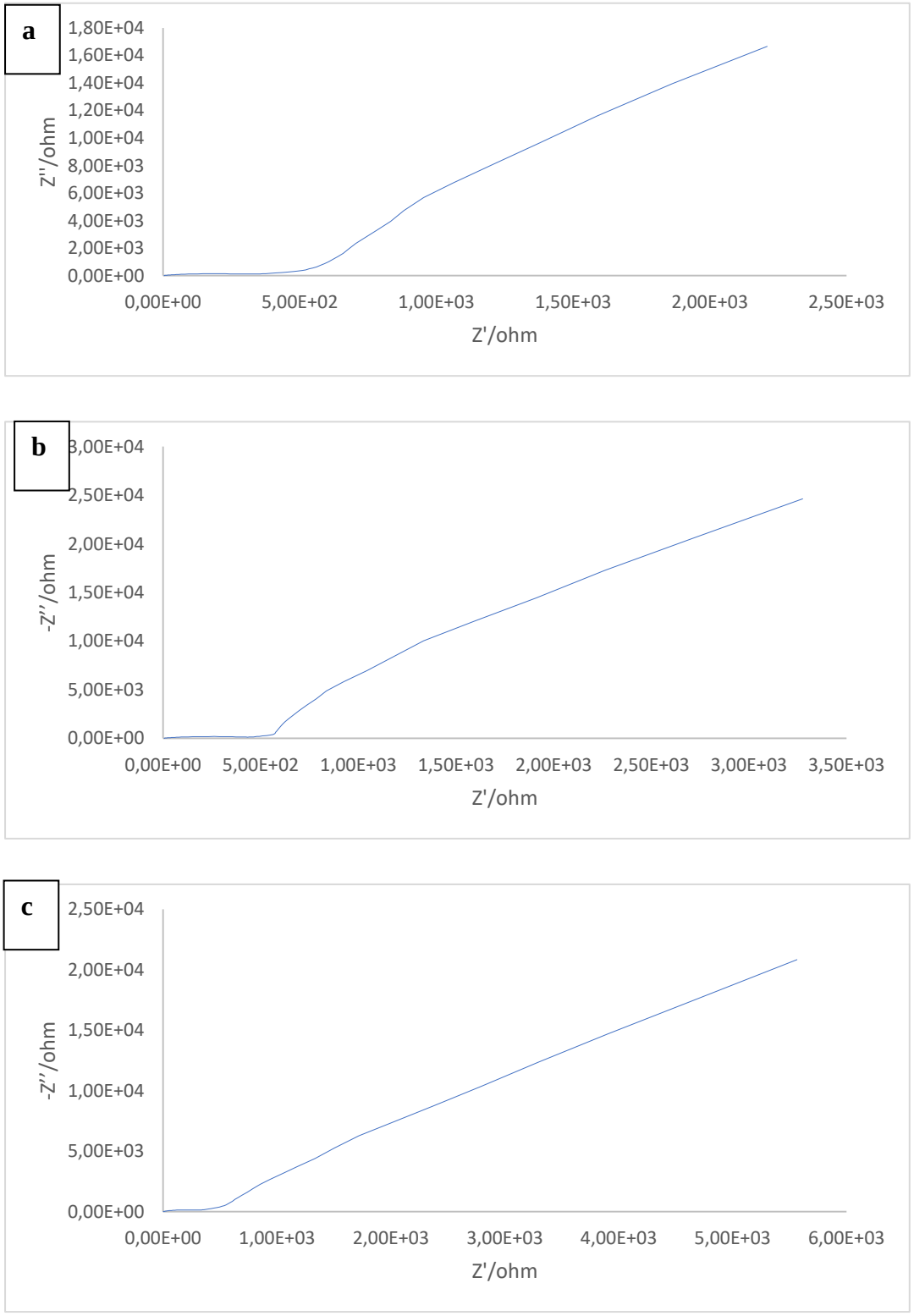

Figure 5.25: EIS plots of (a) as-prepared Li_3VO_4, (b) 5% Fe-doped LVO, (c) 5% Cu-doped LVO.

© University of Venda

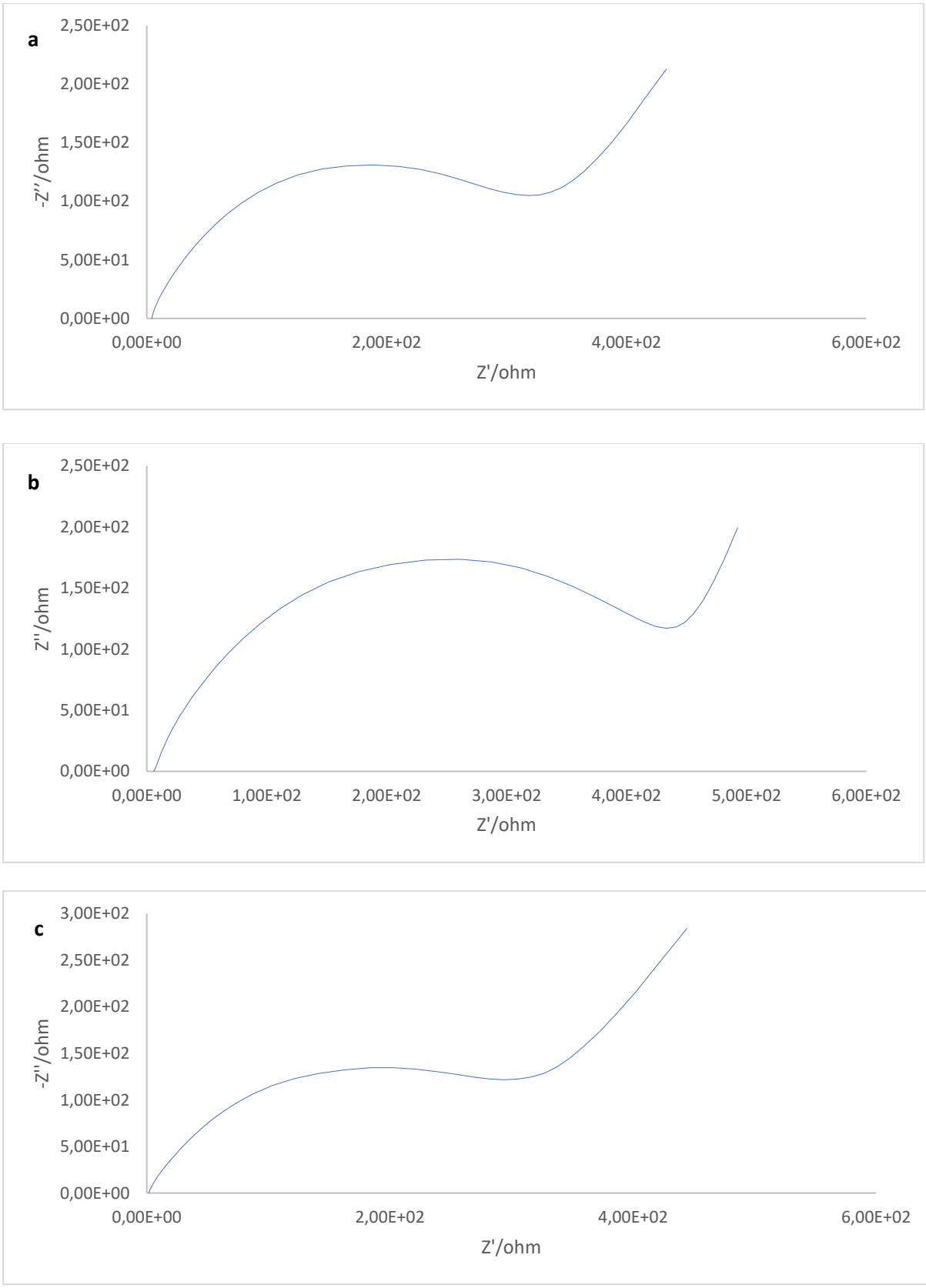

Figure 5.26: EIS plot of high-frequency end of the EIS spectrum of (a) as-prepared Li_3VO_4, (b) 5% Fe-doped Li_3VO_4, (c) 5% Cu-doped Li_3VO_4.

© University of Venda

Table 5.7 lists the solution charge-transfer resistances (R_{CT}) of the three samples. Notably, compared with pure Li_3VO_4 (50 Ω), the charge transfer resistance (R_{CT}) of $Li_3Cu_{0.05}V_{0.95}O_4$ (30 Ω), $Li_3Fe_{0.01}V_{0.99}O_4$ (35 Ω) and $Li_3Fe_{0.05}V_{0.95}O_4$ (30 Ω) are much lower. The lower R_{CT} values of $Li_3Cu_{0.05}V_{0.95}O_4$, $Li_3Fe_{0.01}V_{0.99}O_4$ and $Li_3Fe_{0.05}V_{0.95}O_4$ indicate a remarkable improvement of ion and electron movement, resulting in better lithium storage performance.

Table 5.7: EIS parameters of pure LVO and doped LVO calcined at 730°C.

Samples	**R_{CT}(Ω)**
Li_3VO_4	50
$Li_3Cu_{0.05}V_{0.95}O_4$	30
$Li_3Fe_{0.01}V_{0.99}O_4$	35
$Li_3Fe_{0.05}V_{0.95}O_4$	30

© University of Venda

Chapter 6: Conclusions

Li_3VO_4 nano particle has been considered a promising negative electrode material because of its high theoretical capacity (394 mAh g^{-1}) and zero strain during the charge and discharge processes. However, its electronic conductivity is low, which has led to an electrochemical performance unfavorable for practical application. In this study, Cu and Fe doped Li_3VO_4 sample were successfully synthesized by a simple sol-gel method. TGA was used to study the optimal calcination temperature, which was found to be 750°C, which is also supported by DTG, which shows that there is no further phase change at that temperature. All synthesized nano particles were calcined at 750°C. The materials were examined by XRD, which showed good crystallinity and the orthorhombic structure of the materials.

FTIR revealed that indeed the Li_3VO_4 was formed as shown by the Li-O, V-O-V, and Li-M (Fe or Cu) vibrations. EDS showed the presence of the elements of interest such as O, V, C, Cu and Fe with higher intensity.

SEM showed that the particles of all samples are agglomerates of irregular shape and size, ranging from 1 to 10 μm-sized. The materials are porous, which is good for Li^+ transport. TEM hints at carbon coating of about 3.17 nm. This layer may be from the chelating agent that was used.

Cyclic voltammetry showed SEI formation during the first charge/discharge cycles of doped and undoped LVO samples. The specific capacity of 1% Cu-doped LVO was found to be 11.5 mAh g^{-1} after 170 cycles, 5%Cu-doped LVO reached 63 mAh g^{-1} after 28 cycles, and lastly 5%Fe-doped LVO reached 70 mAh g^{-1} after 30 cycles at the rate of 0.5 C.

Electrochemical impedance spectroscopy showed that the charge-transfer resistance of 1% Fe-doped LVO was 35 Ω, and for 5% Fe-doped LVO and for 5% Cu-doped LVO the charge-transfer resistance was 30 Ω, compared to undoped LVO with 50 Ω charge-transfer resistance. This shows that metal doping potentially plays an important role in improving ionic conductivity. Introducing metals enable better Li^+ diffusion, structural stability, and cycling and rate performance of the negative electrode material.

Future developments that could be considered, are ball-milling the materials to obtain smaller and more even particle sizes (e.g., Liu, Yang *et al.*, 2020), and compositing with different forms of graphite, graphene or reduced graphene oxide (Li, Lei *et al.*, 2021).

© University of Venda

References

Agubra, V.A,. Fergus, J.W. 2014. The formation and stability of the solid electrolyte interface on the graphite anode. *Journal of Power Sources* **268**, 153-162.

Aifantis, K.E., Hackney, S.A., Kumar, R.V. Eds., 2010. *High energy density lithium batteries: materials, engineering, applications*. John Wiley & Sons.

Akinyele, D., Belikov, J., Levron, Y. (2017). Battery storage technologies for electrical applications: Impact in stand-alone photovoltaic systems. *Energies*, *10*(11), 1760.

An, S.J., Li, J., Daniel, C., Mohanty, D., Nagpure, S., Wood, D.L. 2016. The state of understanding of the lithium-ion-battery graphite solid electrolyte interphase (SEI) and its relationship to formation cycling. *Carbon* **105**, 52-76.

Aral, H., Vecchio-Sadus, A., 2008. Toxicity of lithium to humans and the environment—a literature review. *Ecotoxicology and Environmental Safety* **70**(3), 349-356.

Babu, B.V., Babu, K.V., Aregai, G.T., Devi, L.S., Latha, B.M., Reddi, M.S., Samatha, K., Veeraiah, V., 2018. Structural and electrical properties of $Li_4Ti_5O_{12}$ anode material for lithium-ion batteries. *Results in Physics* **9**, 284-289.

Barak, M. (Ed.). 1980. *Electrochemical Power Sources: Primary and Secondary Batteries*, Peregrinus: Stevenage, UK.

Barboux, P., Tarascon, J.M., Shokoohi, F.K., 1991. The use of acetates as precursors for the low-temperature synthesis of $LiMn_2O_4$ and $LiCoO_2$ intercalation compounds. *Journal of Solid State Chemistry* **94**(1), 185-196.

Berg, H., 2015. *Batteries for electric vehicles: materials and electrochemistry*. Cambridge University Press.

Besenhard, J.O., Winter, M., Yang, J., Biberacher, W. 1995. *Journal of Power Source***54**, 228.

Braga, M.H., Grundish, N.S., Murchison, A.J., Goodenough, J.B. 2017. Alternative strategy for a safe rechargeable battery, *Energy & Environmental Science* **10**, 331 - 336.

Bruce, PG., Scrosati, B., Tarascon, J-M. 2008. Nanomaterials for rechargeable lithium batteries. *Angewandte Chemie International Edition* **47**, 2930-2946).

Chan, C., Peng, H., Twesten, R., Jarausch, K., Zhang, X., Fei, Y. 2007. *Nano letters.* **7**, 490-495.

Chan, H.L., Sutanto, D. 2000. A new battery model for use with battery energy storage systems and electric vehicle power systems, *Power Engineering Society Winter Meeting. Conference Proceedings*, Singapore.

© University of Venda

Cheah, Y., Aravindan, V., Madhavi, S. 2012. *Journal of the Electrochemical Society.* **159**, A273-A280.

Chen, H., Cong, T.N., Yang, W., Tan, C., Li, Y., Ding, Y. 2009. Progress in electrical energy storage system: A critical review, *Progress in Natural Science.* **19**, 291 - 312.

Chung, S.Y., Bloking, J.T., Chiang, Y.M. 2011. Electronically conductive phospho-olivines as lithium storage electrodes. In *Materials For Sustainable Energy: A Collection of Peer-Reviewed Research and Review Articles from Nature Publishing Group,* 205-210.

Cluzel, C., Douglas, C. 2012. Cost and performance of EV batteries, *Element Energy*, Final Report for the Committee on Climate Change. http://www. element-energy.co.uk/wordpress/wpcontent/uploads/2012/06/CCC-battery-cost_-Element-Energyreport_March2012_Finalbis.pdf (accessed 14/11/2013).

Collins, J., Gourdin, G., Foster, M., Qu, D., 2015. Carbon surface functionalities and SEI formation during Li intercalation. *Carbon* **92**, 193-244.

Coustier, F., Hill, J., Owens, B.B., Passerini, S., Smyrl, W.H. 1999. Doped vanadium oxides as host materials for lithium intercalation. *Journal of the Electrochemical Society* **146**(4), 1355-1360.

Dahn, J., McKinnon, W. 1987. *Solid State Ionics* **23**, 1-7.

Deng, C., Zhang, S., Fu, B.L., Yang, S.Y., Ma, L. 2010. Characterization of Li_2MnSiO_4 and Li_2FeSiO_4 cathode materials synthesized via a citric acid assisted sol–gel method. *Materials Chemistry and Physics* **120**, 14-17.

Deng, D., 2015. Li-ion batteries: basics, progress, and challenges. *Energy Science & Engineering* **3**(5), 385-418.

Deng, Y., Kang, T., Ma, Z., Tan, X., Song, X., Wang, Z., Pang, P., Shu, D., Zuo, X., Nan, J., 2019. Safety influences of the Al and Ti elements modified $LiCoO_2$ materials on $LiCoO_2$/graphite batteries under the abusive conditions. *Electrochimica Acta* **295**, 703-709.

Di Noto, V., Negro, E., Polizzi, S., Riello, P., Atanassov, P., 2012. Preparation, characterization and single-cell performance of a new class of Pd-carbon nitride electrocatalysts for oxygen reduction reaction in PEMFCs. *Applied Catalysis B: Environmental* **111**, 185-199.

Di Noto, V., Negro, E., Polizzi, S., Vezzù, K., Toniolo, L., Cavinato, G., 2014. Synthesis, studies and fuel cell performance of "core–shell" electrocatalysts for oxygen

© University of Venda

reduction reaction based on a $PtNi_x$ carbon nitride "shell" and a pyrolyzed polyketone nanoball "core". *International Journal of Hydrogen Energy* **39**(6), 2812-2827

Dimitrov, V., Dimitriev, Y., Montenero, A., 1994. IR spectra and structure of $V_2O_5/GeO_2/Bi_2O_3$ glasses. *Journal of Non-Crystalline Solids* **180**(1), 51-57.

Ding, Y., Cano, Z.P., Yu, A., Lu, J., Chen, Z. 2019. Automotive Li-ion batteries: Ferrent status and future perspectives. *Electrochemical Energy Reviews* **2**(1), 1-28.

Du, C., Wu, J., Liu, J., Yang, M., Xu, Q., Tang, Z., Zhang, X., 2015. Synthesis of Lithium vanadium tetroxide anode material via a fast sol-gel method based on spontaneous chemical reactions. *Electrochimica Acta* **152**, 473-479..

Dunn, B., Kamath, H., Tarascon, J-M. 2011. Electrical Energy Storage for the Grid: A Battery of Choices. *Science* **334**(6058), 928 – 935.

El Seoud, O., Nawaz, H., Arêas, E. 2013. Chemistry and Applications of Polysaccharide Solutions in Strong Electrolytes/Dipolar Aprotic Solvents: An Overview. *Molecules* **18**, 1270-1313.

Etacheri, V., Marom, R., Elazari, R., Salitra, G., Aurbach, D. 2011. Challenges in the development of advanced Li-ion batteries: a review. *Energy & Environmental Science.* **4**, 3243 – 3262.

Fogelman, R. 2019. September 2019 Fire Report: The Lithium-ion Battery Problem Worsens. *Waste360* [https://www.waste360.com/safety/september-2019-fire-report-lithium-ion-battery-problem-worsens, accessed on 12.04.2021].

Fu, L., Wu, Y., van Ree, T. 2015. Noncarbon Negative Electrode Materials. *In* Y. Wu, *Lithium-Ion Batteries: Fundamentals and Applications*. Boca Raton: CRC Press Taylor & Francis, 261-262.

Garche, J., Jossen, A. 2000, May. Battery management systems (BMS) for increasing battery life time. In *TELESCON 2000. Third International Telecommunications Energy Special Conference (IEEE Cat. No. 00EX424)* (81-88). IEEE.

Gómez, L.S., de Meatza, I., Martín, M.I., Bengoechea, M., Cantero, I., Rabanal, M.E. 2010. Morphological, structural and electrochemical properties of lithium iron phosphates synthesized by Spray Pyrolysis. *Electrochimica Acta* **55**, 2805-2809.

Gong, C., Xue, Z., Wen, S., Ye, Y., Xie, X. 2016. Advanced carbon materials/olivine $LiFePO_4$ composites cathode for lithium ion batteries. *Journal of Power Sources* **318**, 93-112.

Goodenough, J.B., Kim, Y., 2010. Challenges for rechargeable Li batteries. *Chemistry of Materials* **22**(3), 587-603

© University of Venda

Goodenough, J.B., Park, K.S. 2013. The Li-ion rechargeable battery: a perspective. *Journal of the American Chemical Society* **135**(4), 1167-1176.

Goriparti, S., Miele, E., De Angelis, F., Di Fabrizio, E., Zaccaria, R.P., Capiglia, C., 2014. Review on recent progress of nanostructured anode materials for Li-ion batteries. *Journal of Power Sources* **257**, 421-443.

Hamidah, N.L., Wang, F.M., Nugroho, G. 2019. The understanding of solid electrolyte interface (SEI) formation and mechanism as the effect of flouro-o-phenylenedimaleimaide (F-MI) additive on lithium-ion battery. *Surface and Interface Analysis*, *51*(3), 345-352

Hanna, R., Gross, R., Speirs, J., Heptonstall, P., Gambhir, A. 2015. Assessment innovation timelines from invention to maturity. *UKERC Technol. Policy Assess.*

Hao, J., Lei, G., Li, Z., Wu, L., Xiao, Q., Wang, L. 2013. A novel polyethylene terephthalate nonwoven separator based on electrospinning technique for lithium ion battery. Journal of membrane science. **428**, 11-16.

Haregewoin, A.M., Wotango, A.S., Hwang, B.J. 2016. Electrolyte additives for lithium ion battery electrodes: progress and perspectives, *Energy & Environmental Science.* **9**, 1955–1988.

He, X., Wang, J., Jia, H., Kloepsch, R., Liu, H., Beltrop, K., Li, J. 2015. Ionic liquid-assisted solvothermal synthesis of hollow Mn_2O_3 anode and $LiMn_2O_4$ cathode materials for Li-ion batteries. *Journal of Power Sources* **293**, 306-311.

Heine, J., Hilbig, P., Qi, X., Niehoff, P., Winter, M., Bieker, P., 2015. Fluoroethylene carbonate as electrolyte additive in tetraethylene glycol dimethyl ether based electrolytes for application in lithium ion and lithium metal batteries. *Journal of The Electrochemical Society* **162**(6), A1094-A1101.

Hu, X., Zhang, W., Liu, X., Mei, Y., Huang, Y. 2015. *Chem. Soc. Rev.* **44**, 2376-2404.

Huang, L.H., Min, Z.H., Zhang, Q.Y. 2014. Solid electrolyte inter-phase on graphite anodes in Li-ion batteries. *Advanced Materials Science* **36**, 13-20.

Jeong, G., Kim, Y.U., Kim, H., Kim, Y.J., Sohn, H.G. 2011. Prospective materials and applications for Li secondary batteries. *Energy & Environmental Science.* **4**, 1986–2002.

Johnson, I.D., Lübke, M., Wu, O.Y., Makwana, N.M., Smales, G.J., Islam, H.U., Dedigama, R.Y., Gruar, R.I., Tighe, C.J., Scanlon, D.O., Corà, F. 2016. Pilot-scale continuous synthesis of a vanadium-doped $LiFePO_4$/C nanocomposite high-rate cathodes for lithium-ion batteries. *Journal of Power Sources* **302**, 410-418.

© University of Venda

Julien CM., Mauger A., Zaghib K., Groult H. 2014. Comparative issues of cathode materials for Li-ion batteries. *Inorganics*. **2**(1), 132-54.

Kamali-Heidari, E., Kamyabi-Gol, A., Ataie, A. 2018. Electrode Materials for Lithium Ion Batteries: A Review. *Journal of Ultrafine Grained and Nanostructured Materials* **51**(1), 1-12.

Kang, D.H.P., Chen, M., Ogunseitan, O.A. 2013. Potential environmental and human health impacts of rechargeable lithium batteries in electronic waste. *Environmental Science & Technology* **47**, 5495-5503.

Kim, T., Shin, J., You, T.S., Lee, H., Kim, J., 2015. Thermally controlled V_2O_5 nanoparticles as cathode materials for lithium-ion batteries with enhanced rate capability. *Electrochimica Acta, 164*, 227-234.

Kirillov, S.A. 2019. Electrode materials and electrolytes for high-rate electrochemical energy systems: a review. *Theoretical and Experimental Chemistry* **55**(2), 73-95.)

Koch, S.L., Morgan, B.J., Passerini, S. and Teobaldi, G. 2015. Density functional theory screening of gas-treatment strategies for stabilization of high energy-density lithium metal anodes. *Journal of Power Sources* **296**, 150-161.

Ku, J., Ryu, J., Kim, S., Han, O., Oh, S. 2012. *Advanced Functional Materials.* **22**, 3658-3664.

Kulka, A., Redel, K., & Molenda, J., 2019. Platelet-shape $LiFePO_4/Fe_2P/C$ composite material as a high-rate positive electrode for Li-ion batteries. *Solid State Ionics* **335**, 113-120.

Lebedeva, N., Di Persio, F., Boon-Brett, L. 2016. *Lithium ion battery value chain and related opportunities for Europe*. European Commission: Petten.

Lee, W.J., Maiti, U.N., Lee, J.M., Lim, J., Han, T.H., Kim, S.O., 2014. Nitrogen-doped carbon nanotubes and graphene composite structures for energy and catalytic applications. *Chemical Communications*, **50**(52), 6818-6830.

Leng, F., Tan, C.M., Pecht, M. 2015. Effect of temperature on the aging rate of Li ion battery operating above room temperature. *Scientific Reports* **5**, 12967.

Li, J., Daniel, C., Wood, D. 2011. Materials processing for lithium-ion batteries. *Journal of Power Source***196**, 2452-2460.

Li, Z., Lei, H., Kan, A., Xie, H., Yu, W. 2021. Photothermal applications based on graphene and its derivatives: A state-of-the-art review. *Energy*, **216**, 119262.

Li, H., Liu, X., Zhai, T., Li, D., Zhou, H., 2013. Li_3VO_4: a promising insertion anode material for lithium-ion batteries. *Advanced Energy Materials*, **3**(4), 428-432.

© University of Venda

Li, Z., Huang, J., Liaw, B. Y., Metzler, V., Zhang, J. 2014. A review of lithium deposition in lithium-ion and lithium metal secondary batteries. *Journal of Power Source***254**, 168-182.

Li, Q., Wei, Q., Sheng, J., Yan, M., Zhou, L., Luo, W., Sun, R., Mai, L., 2015. Mesoporous Li_3VO_4/C Submicron-Ellipsoids Supported on Reduced Graphene Oxide as Practical Anode for High-Power Lithium-Ion Batteries. *Advanced Science*, **2**(12), 1500284.

Liao, C., Zhang, Q., Zhai, T., Li, H.,Zhou, H., 2017. Development and perspective of the insertion anode Li_3VO_4 for lithium-ion batteries. *Energy Storage Materials*, **7**, 17-31.

Liao, F., Światowska, J., Maurice, V., Seyeux, A., Klein, L.H., Zanna, S., Marcus, P., 2015. The influence of the electrolyte on chemical and morphological modifications of an iron sulfide thin film negative electrode. *Physical Chemistry Chemical Physics*, *17*(1), 619-629.

Liu, X., Li, G., Zhang, D., Chen, D., Wang, X., Li, B., Li, L. 2019. Fe-doped Li_3VO_4 as an excellent anode material for lithium ion batteries: Optimizing rate capability and cycling stability. *Electrochimica Acta* **308**, 185-194.

Liu, J., Lu, P.J., Liang, S., Wang, W., Lei, M., Tang, S., Yang, Q., 2015. Ultrathin Li_3VO_4 nanoribbon/graphene sandwich-like nanostructures with ultrahigh lithium ion storage properties. *Nano Energy*, *12*, 709-724.

Liu, F., Song, S., Xue, D., Zhang, H., 2012. Selective crystallization with preferred lithium-ion storage capability of inorganic materials. *Nanoscale Research Letters* **7**(1), 149.

Liu, Y., Yang, Y., Chen, P., Shan, Y., Li, Y., Shi, J., Hou, J., Zhang, N., Zhao, G., Xu, J., Fang, Y., Dai, N. 2020. Nano Ball-Milling Using Titania Nanoparticles to Anchor Cesium Lead Bromine Nanocrystals and Energy Transfer Characteristics in TiO_2@$CsPbBr_3$ Architecture. *Small* **16**, 2004126.

Liu, W., Zhang, X., Li, C., Wang, K., Sun, X., Ma, Y., 2020. Carbon-coated Li_3VO_4 with optimized structure as high capacity anode material for lithium-ion capacitors. *Chinese Chemical Letters*, *31*(9), 2225-2229.

Lu, P., Harris, S.J. 2011. Lithium transport within the solid electrolyte interphase. *Electrochem. Commun.* **13**, 1035-1037.

Lu, C.H., Lee, W.C., Liou, S.J. and Fey, G.T.K., 1999. Hydrothermal synthesis of $LiNiVO_4$ cathode material for lithium ion batteries. *Journal of Power Sources* **81**, 696-699.

Lyster, R., Verchick, R.R. 2018. *Protecting the Power Grid from Climate Disasters*. In *Climate Disaster Law: Barriers and Opportunities,* Rosemary Lyster & Robert R.M. Verchick (Eds.), Edward Elgar Publishing Ltd.

© University of Venda

Ma, X.J., Zhang, W.B., Kong, L.B., Luo, Y.C., Kang, L. 2016. Pseudocapacitance of ammonium metavanadate pyrolysis products. *Electrochimica Acta* **192**, 30-37.

Malavika, C.R. 2004. Environmental effects associated with battery disposal. *Frost and Sullivan Insight,* [http://www.frost.com/prod/servlet/market-insight-print.pag?docid=20759887 [last accessed on 16.02.2019].

Malini, R., Uma, U., Sheela, T., Ganesan, M., Renganathan, N.G. 2009. Conversion reactions: a new pathway to realise energy in lithium-ion battery. *Ionics* **15**(3), 301-307.

Meng, Y.S., Arroyo-de Dompablo, M.E. 2009. First principles computational materials design for energy storage materials in lithium ion batteries. *Energy & Environmental Science* **2**(6), 589-609.

Meng, J., Guo, H., Niu, C., Zhao, Y., Xu, L., Li, Q., Mai, L. 2017. Advances in structure and property optimizations of battery electrode materials. *Joule* **1**(3), 522-547.

Meng, Q., Zhang, Y., Dong, P. 2018. A combined process for cobalt recovering and cathode material regeneration from spent $LiCoO_2$ batteries: Process optimization and kinetics aspects. *Waste Management* **71**, 372-380.

Migov, S. 2017. *Battery Recycling Technology: Russian market research*. Thesis, Centria University of Applied Sciences, St Petersburg, Russia.

Ming, J., Cao, Z., Wu, Y., Wahyudi, W., Wang, W., Guo, X., Cavallo, L., Hwang, J.Y., Shamim, A., Li, L.J., Sun, Y.K., 2019. New insight on the role of electrolyte additives in rechargeable lithium ion batteries. *ACS Energy Letters*, *4*(11), 2613-2622..

Mjejri, I., Etteyeb, N., Sediri, F. 2013. Hydrothermal synthesis of mesoporous rod-like nanocrystalline vanadium oxide hydrate $V_3O_7{\bullet}H_2O$ from hydroquinone and V_2O_5. *Materials Research Bulletin* **48**(9), 3335-3341.

Ni, S., Lv, X., Ma, J., Yang, X., Zhang, L. 2014. The fabrication of Li_3VO_4/Ni composite material and its electrochemical performance as anode for Li-ion battery. *Electrochimica Acta* **130**, 800-804.

Nishi, Y. 2001. Lithium ion secondary batteries; past 10 years and the future. *Journal of Power Sources* **100**, 101-106.

Nitta, N., Wu, F., Lee, J. T., & Yushin, G. 2015. Li-ion battery materials: Present and future. *Materials Today* **18**(5), 252-26.

Palacin, M.R., 2009. Recent advances in rechargeable battery materials: a chemist's perspective. *Chemical Society Reviews* **38**(9), 2565-2575.

© University of Venda

Parasuraman, A., Tuti Mariana, L., Skyllas-Kazacos, M. 2013. Vanadium based nanoelectrode materials in energy storage systems. *Nanoscience & Nanotechnology-Asia* **3**(1), 3-10.

Park, C.M., Kim, J.H., Kim, H., Sohn, H.J., 2010. Li-alloy based anode materials for Li secondary batteries. *Chemical Society Reviews* **39**(8), 115-3141.

Peled, E. 1979. The Electrochemical Behavior of Alkali and Alkaline Earth Metals in Nonaqueous Battery Systems -- The Solid Electrolyte Interphase Model. *Journal of The Electrochemical Society*. 2047-2051.

Peled, E., Golodnitsky, D., Penciner, J. 1998 . The anode/electrolyte interface. *Handbook of Battery Materials*, 419-456

Pimentel, D., Berger, B., Filiberto, D., Newton, M., Wolfe, B., Karabinakis, E., Clark, S., Poon, E., Abbett, E., Nandagopal, S. 2004. Water resources: agricultural and environmental issues. *BioScience* **54**, 909-918.

Pinson, M.B., Bazant, M.Z., 2013. Theory of SEI formation in rechargeable batteries: capacity fade, accelerated aging and lifetime prediction. *Journal of the Electrochemical Society* **160**(2), A243-A250.

Poizot, P., Laruelle, S., Grugeon, S., Dupont, L., Tarascon, J. 2000. *Nature* **407**, 496-499.

Priyono, S., Ginting, N.R., Humaidi, S., Subhan, A. and Prihandoko, B., 2018. Synthesis of lithium mangan dioxide ($LiMn_2O_4$) for lithium-ion battery cathode from various lithium sources. In *Journal of Physics: Conference Series* (Vol. 985, No. 1, p. 012054). IOP Publishing

Qiao, Y.Q., Wang, X.L., Mai, Y.J., Xia, X.H., Zhang, J., Gu, C.D., Tu, J.P. 2012. *Journal of Alloys and Compounds* . **536**, 132.

Qin, M.L., Liu, W.M., Liang, S.Q. and Pan, A.Q., 2016. Facile synthesis of porous $LiNiVO_4$ powder as high-voltage cathode material for lithium-ion batteries. *Transactions of Nonferrous Metals Society of China* **26**(12), 3232-3237.

Rajagopalan, R. 2017. *Nasicon based materials for high voltage lithium-ion and sodium-ion batteries*, PhD thesis, Wollongong University, Australia.

Ram, P., Singhal, R., Sharma, R.K., 2017. Preliminary study of dysprosium doped $LiMn_2O_4$ spinel cathode materials. *Materials Today: Proceedings* **4**(9), 9365-9370.

Rui, X.H., Jin, Y., Feng, X.Y., Zhang, L.C., Chen, C.H., 2011. *Journal of. Power Sources* **196**, 2109.

Scanlon, D., Watson, G., Payne, D., Atkinson, G., Egdell, R., Law, D. 2010. *The Journal of Physical Chemistry C* **114**, 4636-4645.

© University of Venda

Shchelkanova, M.S., Shekhtman, G.S., Druzhinin, K.V., Pankratov, A.A. and Pryakhina, V.I., 2019. The study of lithium vanadium oxide LiV_3O_8 as an electrode material for all-solid-state lithium-ion batteries with solid electrolyte $Li_{3.4}Si_{0.4}P_{0.6}O_4$. *Electrochimica Acta* **320**, 134570.

Schlesinger, H.R. 2010. *The Battery: How Portable Power Sparked a Technological Revolution*. Smithsonian Books: Washington, D.C., USA.

Shi, Y., Wang, J.Z., Chou, S.L., Wexler, D., Li, H.J., Ozawa, K., Liu, H.K., Wu, Y.P. 2013, Hollow Structured Li_3VO_4 Wrapped with Graphene Nanosheets in Situ Prepared by a One-Pot Template-Free Method as an Anode for Lithium-Ion Batteries. *Nano Letters* **13**, 4715 - 4720.

Shkrob, I.A., Zhu, Y., Marin, T.W., Abraham, D. 2013. Reduction of carbonate electrolytes and the formation of solid-electrolyte interface (SEI) in lithium-ion batteries. 1. Spectroscopic observations of radical intermediates generated in one-electron reduction of carbonates. *The Journal of Physical Chemistry C* **117**, 19255-19269.

Song, H.J., Choi, M., Kim, J.C., Park, S., Lee, C.W., Hong, S.H., Kim, B.K. and Kim, D.W., 2016. Enhanced lithium storage in reduced graphene oxide-supported M-phase vanadium (IV) dioxide nanoparticles. *Scientific Reports* **6**(1), 1-8.

Tabuchi, M., Nabeshima, Y., Ado, K., Shikano, M., Kageyama, H., Tatsumi, K., 2007. Material design concept for Fe-substituted Li_2MnO_3-based positive electrodes. *Journal of Power Sources*, **174**(2), 554-559.

Tang, W., Wang, X.J., Hou, Y.Y., Li, L.L., Sun, H., Zhu, Y.S., Bai, Y., Wu, Y.P., Zhu, K., Van Ree, T., 2012. Nano $LiMn_2O_4$ as cathode material of high rate capability for lithium ion batteries. *Journal of Power Sources*, **198**, 308-311.

Tang, Y., Zhang, Y., Li, W., Ma, B., Chen, X.2015. Rational material design for ultrafast rechargeable lithium-ion batteries. *Chemical Society Reviews*, **44**(17), 5926-5940.

Tarascon, J.M., Armand, M. 2011. Issues and challenges facing rechargeable lithium batteries. In *Materials For Sustainable Energy: A Collection of Peer-Reviewed Research and Review Articles from Nature Publishing Group*, 171-179.

Tie, S.F., Tan, C.W. 2013. A review of energy sources and energy management system in electric vehicles. *Renewable and sustainable energy reviews.* **20**, 82-102.

Tomaszewska, A., Chu, Z., Feng, X., O'Kane, S., Liu, X., Chen, J., Ji, C., Endler, E., Li, R., Liu, L., Li, Y., 2019. Lithium-ion battery fast charging: A review. *ETransportation* **1**, 100011.

© University of Venda

Tron, A., Park, Y.D., Mun, J. 2016. AlF_3-coated $LiMn_2O_4$ as cathode material for aqueous rechargeable lithium battery with improved cycling stability. *Journal of Power Sources* **325**, 360-364.

Vedala, S., Sushama, M., 2018. Urea Assisted Combustion Synthesis of $LiFePO_4$/C Nano composite Cathode Material for Lithium Ion Battery Storage System. *Materials Today: Proceedings* **5**(1), 1649-1656.

Verma, P., Maire, P., Novák, P. 2010. A review of the features and analyses of the solid electrolyte interphase in Li-ion batteries. *Electrochimica Acta* **55**(22), 6332-6341.

Vignarooban, K., Kushagra, R., Elango, A., Badami, P., Mellander, B.E., Xu, X., Tucker, T.G., Nam, C., Kannan, A.M. 2016. Ferrent trends and future challenges of electrolytes for sodium-ion batteries, *Int. J. Hydrogen Energy* **41**, 2829–2846.

Walker, A. 2013. *Solar energy: technologies and project delivery for buildings*. John Wiley & Sons.

Wang, A., Kadam, S., Li, H., Shi, S., Qi, Y. 2018. Review on modeling of the anode solid electrolyte interphase (SEI) for lithium-ion batteries. *npj Computational Materials*, *4*(1),1-26.

Wang, B., Qu, Q.T., Yang, L.C., Xia, Q., Wu, Y.P., Zhou, D.L., Gu, X.J., van Ree, T. 2009. 2-Phenylimidazole as an additive to prevent the co-intercalation of propylene carbonate in organic electrolyte for lithium-ion batteries, *Journal of. Power Sources* **189**, 757-760.

West, K., B. Zachau-Christiansen, S.V. Skaarup., F.W. Poulsen. 1992. Lithium Insertion in Sputtered Vanadium Oxide Film. *Solid State Ionics* **57**, 41–47. doi:10.1016/0167-2738(92)90062-T

Whitacre, J. 2012. What's Inside an Aqueous Hybrid Ion Battery? http://www.aquionenergy.com/blog/bid/108285/What-s-Inside-an-Aqueous-Hybrid-Ion-Battery [last accessed 21.12.2017]

Whittingham, M.S. 1978. Chemistry of intercalation compounds: Metal guests in chalcogenide hosts. *Progress in Solid State Chemistry*, *12*(1), 41-99.

Winter, M., Brodd, R.J., 2004. What are batteries, fuel cells, and supercapacitors? C*hemInform* **35**(50), 4245. https://doi.org/10.1002/chin.200450265

Wu, H., Chen, J., Hng, H., Wen Lou, X. 2012. *Nanoscale* **4**, 2526-2542.

Wu, Y.P. (Ed.). 2015. *Lithium-ion batteries: Fundamentals and Applications*. Boca Raton: CRC Press Taylor&Francis. ISBN 978-1-46-655733-8.

© University of Venda

Wu, F., Maier, J., Yu, Y. 2020. Guidelines and trends for next-generation rechargeable lithium and lithium-ion batteries. *Chemical Society Reviews*, **49(5)**, 1569-1614..

Wu, X., Song, K., Zhang, X., Hu, N., Li, L., Li, W., Zhang, L., Zhang, H. 2019. Safety Issues in Lithium Ion Batteries: Materials and Cell Design. *Frontiers in Energy Research*, **7**, 65.

Wu, Y., Yuan, X., Dong, C., Duan, Y. 2011. *Lithium Ion Batteries: Practice and Applications.* Beijing: Chemical Industry Press.

Xu, K. 2004. Nonaqueous Liquid Electrolytes for Lithium-Based Rechargeable Batteries. *Chem. Rev*., 4303–4418.

Yamaguchi, K., Domi, Y., Usui, H., Shimizu, M., Morishita, S., Yodoya, S., Sakata, T., Sakaguchi, H. 2019. Effect of Film-Forming Additive in Ionic Liquid Electrolyte on Electrochemical Performance of Si Negative-Electrode for LIBs. *Journal of the Electrochemical Society*. **166**(2), A268-A276.

Yan, X., Chen, L., Shah, S. A., Liang, J.,Liu, Z. 2017. The effect of Co_3O_4 & $LiCoO_2$ cladding layer on the high rate and storage property of high nickel material $LiNi_{0.8}Co_{0.15}Al_{0.05}O_2$ by simple one-step wet coating method. *Electrochimica Acta*, **249**, 179-188.

Yang, L.C., Qu, Q.T., Shi, Y., Wu, Y.P., Van Ree, T. 2010. Materials for lithium-ion batteries by mechanochemical methods. In *High-Energy Ball Milling* (pp. 361-408). Woodhead Publishing.

Yan, Z., Sun, Z., Xia, A., Yin, R., Huang, X., Yue, K., Xu, H., Zhao, G., Qian, L. 2019. Li_3VO_4/carbon sheets composites from cellulose as an anode material for high performance lithium-ion batteries. *Ceramics International*.

Yuan, M., Liu, K., 2020. Rational design on separators and liquid electrolytes for safer lithium-ion batteries. *Journal of Energy Chemistry*, 43, 58-70.

Zakharova, G.S., Thauer, E., Wegener, S.A., Nölke, J.H., Zhu, Q., Klingeler, R., 2019. Hydrothermal microwave-assisted synthesis of Li_3VO_4 as an anode for lithium-ion battery. *Journal of Solid State Electrochemistry*, **23**(7), 2205-2212.

Zhang, S.S. 2006. A review on electrolyte additives for lithium-ion batteries. *Journal of Power Source***162**(2), 1379-1394.

Zhang, T., Imanishi, N., Shimonishi, Y., Hirano, A., Takeda, Y., Yamamoto, O., Sammes, N. 2010. A novel high energy density rechargeable lithium/air battery. *Chemical Communications.*, **46**, 1661-1663.

© University of Venda

Zhang, X., Kostecki, R., Richardson, T.J., Pugh, J.K. and Ross, P.N. 2001. Electrochemical and infrared studies of the reduction of organic carbonates. *Journal of the Electrochemical Society*, **148**(12), A1341-A1345.

Zhang, J., Ni, S., Ma, J., Yang, X., Zhang, L. 2016. High capacity and superlong cycle life of Li_3VO_4/NeC hybrids as anode for high performance Li-ion batteries. *Journal of Power Source* **301**, 41-46.

Zhang, H., Wang, X., Liang, Y. 2015. Preparation and characterization of a Lithium-ion battery separator from cellulose nanofibers. *Heliyon*, **1**(2), 00032.

Zhang, H.P., Xia, Q., Wang, B., Yang, L.C., Wu, Y.P., Sun, D.L., Gan, C.L., Luo, H.J., Bebeda, A.W., van Ree, T. 2009. Vinyl-tris-(methoxydiethoxy)silane as an effective and ecofriendly flame retardant for electrolytes in lithium ion batteries, *Electrochemistry communications* . **11**, 526-529.

Zhang, M., Zhang, X., Liu, Z., Peng, H. and Wang, G., 2020. Ball milling-derived nanostructured Li_3VO_4 anode with enhanced surface-confined capacitive contribution for lithium ion capacitors. *Ionics*, 1-12

Zhang, Y., Zhang, Y., Xia, S., Dong, P., Jin, L., Song, J., 2013. Challenges in the Development of Film-Forming Additives for Lithium Ion Battery: A Review. *American Journal of Analytical Chemistry*, **4**, 7-12.

Zhao, H., Nie, Y., Li, Y., Wu, T., Zhao, E., Song, J., Komarneni, S. 2019. Low-cost and eco-friendly synthesis of octahedral $LiMn_2O_4$ cathode material with excellent electrochemical performance. *Ceramics International* **45**(14), 17183 - 17191.

Zhao, W., Ji, Y., Zhang, Z., Lin, M., Wu, Z., Zheng, X., Li, Q., Yang, Y. 2017. Recent advances in the research of functional electrolyte additives for lithium-ion batteries. *Current Opinion in Electrochemistry* **6**(1), 84-91.

Zhu, X., Zhou, S., Jiang, X., Yao, X., Xu, X., Peng, A., Wang, L., Xue, Q., 2020. High-performances of Li4Ti5O12 anodes for lithium-ion batteries via modifying the Cu current collector through magnetron sputtering amorphous carbon. *Journal of Alloys and Compounds, 830*, 154682.

© University of Venda

© University of Venda